Atmospheric boundary layer structure at the head of a small Alpine tributary valley detected with uncrewed aerial systems (UAS)

Master's Thesis

in Atmospheric Sciences

Submitted to the

Faculty of Geo- and Atmospheric Sciences

of the

University of Innsbruck

in Partial Fulfillment of the Requirements for the Degree of

Master of Science

by

Almut Alexa

Advisors

Assoc. Prof. Dr. Alexander Gohm, University of Innsbruck
Dr. Norman Wildmann, German Aerospace Center (DLR)

Innsbruck, November 2023

Abstract

Wind systems in the atmospheric boundary layer within valleys contribute to the transport and exchange of mass, energy, and momentum in mountainous areas. The research program "Multiscale transport and exchange processes in the atmosphere over mountains" (TEAMx) aims to investigate these processes on different scales through observations and numerical simulations in the TEAMx Observational Campaign (TOC) in 2024/2025. Measurements will be conducted at multiple sub-target areas across the Alps one of which being Nafingalm, a head of a tributary valley in Tyrol, Austria. In the framework of a pre-campaign in 2022 (TEAMx-PC22), ground-based and airborne measurements were done at Nafingalm to explore the local mountain boundary layer and to test instrumentation for the TOC. Ground-based instruments were deployed between 15 June and 12 September 2022. Flights with a fleet of uncrewed aerial systems (UAS) were performed between 20 and 28 June 2022. The UAS measured temperature and humidity by an external sensor. Wind speed and direction were determined from the attitude data of the drones. Flight patterns performed were simultaneous point measurements, vertical and horizontal profiles, and combinations of these patterns. A case study was done on 23 June 2022 when most UAS flights were available, analyzing the atmospheric processes that occurred during different periods of the day. The UAS measurements complemented and extended the ground-based measurements, illustrating the occurrence of thermally-driven winds, foehn winds, and the formation of a stable boundary layer at the valley ground. Nafingalm proved to be a suitable location to observe local and mesoscale phenomena and their interaction. For the TOC, the UAS measurements should be complemented with remote sensing and further ground-based in-situ instrumentation in order to measure wind as well as temperature and humidity distribution along the valley axis and at heights up to crest level. A larger drone fleet would allow to sample areas on the scale of a cross-valley circulation. Doppler wind lidars could provide insight into along-valley and cross-valley winds at levels higher than the maximum UAS flight level. Ground-based instrumentation at the slopes could compensate for the inability of the lidar and UAS to measure in the range of a meter from the valley side wall.

Contents

Chapter 1

Introduction

1.1 Motivation

The atmospheric boundary layer (ABL) in mountainous terrain is more complex than the one in flat terrain. Generally, in the ABL, energy, momentum, and mass are exchanged between the Earth's surface and the atmosphere (Stull 1988). In flat terrain, exchange happens mainly in the vertical. In complex terrain, however, horizontal exchange and additional processes such as thermally- and dynamically-driven winds become important (Serafin et al. 2020; Whiteman 2000).

Parameterizations to describe ABL processes in numerical models are usually developed for horizontally homogeneous, flat (HHF) terrain. This approximation was suitable decades ago when numerical models had grid sizes on the order of 100 km × 100 km so that orography of a few kilometers height was negligible (Rotach et al. 2022). Nowadays, most model grids have a much finer horizontal resolution, even climate simulations go down to the order of kilometers (Ban et al. 2021). Hence, the actual non-HHF character of mountainous terrain cannot be ignored (Rotach et al. 2022).

Current ABL parameterizations are still based on the assumption of relevant time scales of up to one hour (Stull 1988; Rotach et al. 2022). Phenomena in the mountains span many more time scales, including much shorter (e. g. reaction time of slope winds to changes in surface energy balance) and much longer (e. g. diurnal cycle of valley winds) time scales than one hour (Serafin et al. 2020). ABL parameterizations are not adapted to those different time scales. Lehner and Rotach (2018) extended Stull's (1988) definition of the ABL with respect to those time scales to describe the mountain boundary layer (MoBL). More information on this definition is to be found in section 1.2.1.

To improve models, a better understanding of processes in the ABL over mountains is needed (Adler et al. 2021). Furthermore, one of the most problematic issues in atmospheric modeling are surface fluxes and surface temperature diurnal cycles, following a survey of WGNE (Working Group on Numerical Experimentation, an interdisciplinary body of WMO; Zadra et al. 2018). This applies not only to mountainous regions, never-

theless, mountains play a significant role since more than 50% of the global land surface is classified as complex terrain, according to Rotach et al. (2014).

Surface fluxes are one of the main components of ABL parameterizations. Surface exchange in the MoBL is generated not only by vertical but also by horizontal turbulent mixing (Strauss et al. 2016; Umek et al. 2021), as well as thermally-driven flows such as slope and valley winds (Zardi and Whiteman 2013), and dynamically-driven flows such as foehn (Jackson et al. 2013).

Thermally-driven winds are crucial for mass transport towards the main crest which can initiate convection (Kirshbaum et al. 2018; Göbel et al. 2023). Convection and the resulting precipitation is another large error source in models (Zadra et al. 2018).

The different mountain wind systems are not mutually exclusive but can superimpose each other (Zardi and Whiteman 2013), potentially modifying the turbulence characteristics of the MoBL (Jackson et al. 2013). Many of the flows occurring in complex terrain have already been investigated in main valleys, e. g. CROSSINN in the Inn Valley (Adler et al. 2021), MATERHORN at the foot of a desert mountain (Lehner et al. 2015) or Perdigão near two parallel mountain ridges (Mann et al. 2017), or homogeneous sections of a slope (e. g. Wagner et al. 2014; Freitas et al. 2022). Yet, similar studies performed at the head of a tributary valley are rare, even though a few of them do exist (Freytag and Hennemuth 1981, 1982). One reason might be that, at a valley head, the slope is inherently inhomogeneous in terms of solar exposure. Additionally, valley winds transition into slope winds and vice versa at a valley head, or they superimpose within the whole valley, hence, distinguishing the two wind systems can be difficult (Hennemuth and Schmidt 1985; Mikkola et al. 2023; Wagner et al. 2015b). The presence of water masses such as lakes can induce wind systems such as lake breezes and can further complicate the exchange processes of energy, mass, and momentum (Chazette et al. 2021; Laiti et al. 2014).

Investigating multiscale transport and exchange processes in the MoBL experimentally and numerically in order to improve ABL parameterizations for complex terrain is the objective of the TEAMx program ("Multi-scale transport and exchange processes in the atmosphere over mountains"; Serafin et al. 2020; Rotach et al. 2022). Besides numerical simulations, atmospheric observations will be performed on a large range of scales both spatially and temporally to achieve this goal: from the whole Alps over main valleys, tributary valleys, and mountain slopes, to only meter-sized areas. The major part of the measurements is planned to be conducted in 2024/2025 within the TEAMx Observational Campaign (TOC). In order to assess the suitability of measurement locations and techniques for the TOC, instrumentation was tested at multiple target areas in the Alps in summer 2022 within the TEAMx pre-campaign (TEAMx-PC22; Pfister et al. 2023). One of the target areas is the Inn Valley in Tyrol, Austria. It has multiple sub-target areas, one of which is Nafingalm, a valley head south of the Inn Valley.

In the framework of the project ESTABLIS-UAS (Exposing spatio-temporal Structures of Turbulence in the Atmospheric Boundary Layer with In-Situ measurements by a fleet of Unmanned Aerial Systems), a fleet of uncrewed aerial systems (UAS) is used to measure wind, temperature and moisture simultaneously at multiple locations in order to gain knowledge about the sub-mesoscale structure of the ABL (Wildmann et al. 2022). After the fleet was deployed in flat, heterogeneous terrain (Wetz et al. 2023; Wildmann and Wetz 2022), a next step was to use the UAS fleet in mountainous terrain. This was done during the TEAMx-PC22 at the sub-target area Nafingalm. Between 20 and 28 June 2022, a fleet of up to three drones performed various flight patterns in different weather conditions in order to assess which MoBL processes can be captured by the UAS, combined with ground-based instrumentation, and what is to be improved for the TOC.

The results of the measurements at Nafingalm at the end of June 2022 are analyzed in this Master's thesis. A focus is on 23 June 2022 as this was the day with most UAS flights, covering the evolution of the lowest 120 m of the ABL from early morning to late evening.

1.2 State of research

In this section, the basic meteorological knowledge about atmospheric boundary layers, boundary layers in mountainous areas, and thermally- and dynamically-driven winds is described. Furthermore, information about UAS measurements in the meteorological context is given.

1.2.1 Atmospheric boundary layer

The atmospheric boundary layer (ABL) is the lowest part of the troposphere where the exchange of energy, mass, and momentum between the Earth's surface and the atmosphere takes place (Stull 1988). On ideal days, it undergoes a typical diurnal cycle.

Diurnal cycle On radiation days when solar radiation reaches the ground unimpededly, the diurnal cycle typically develops two main states with transitions between those states, as illustrated in Fig. 1.1. At noon, with net energy flux from the ground to the atmosphere, the ABL is well-mixed and neutrally or unstably stratified (corresponding to the arrow indicating 3 PM in Fig. 1.1). The largest part of the ABL at that time is called the mixed layer (ML). Above is the entrainment zone providing exchange with the free atmosphere. Close to the ground, superadiabatic stratification can be found if the (mainly solar) forcing and the resulting surface heat flux from the ground to adjacent air is large enough (not shown in Fig. 1.1). Positive buoyancy of air close to the ground can lead to convection throughout the whole ABL.

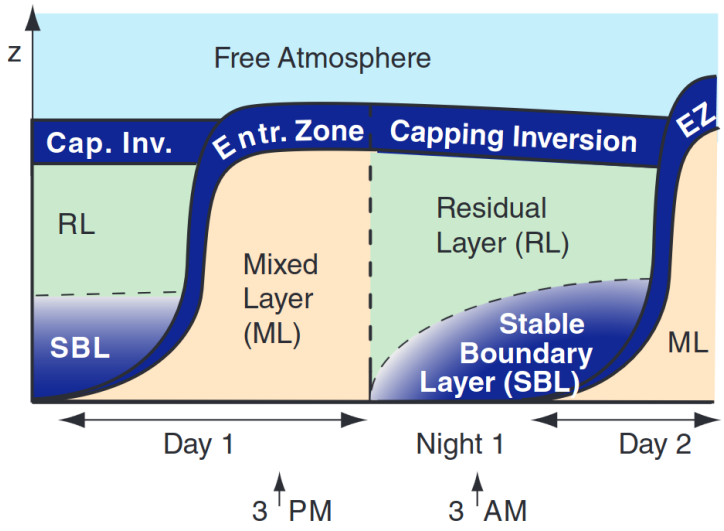

Figure 1.1: Diurnal cycle of the ABL during fair weather. Cap. Inv. stands for Capping Inversion. Entr. Zone and EZ stand for Entrainment Zone. The different tans indicate stable (dark blue), neutral (green), and unstable (orange) stratification. Taken from Stull (2017).

The ABL structure starts to change during the evening transition: the sun sets and the surface net energy flux becomes negative (from air to ground). A ground inversion forms the stable boundary layer (SBL, cf. 3-AM mark in Fig. 1.1). The remaining mixed layer above becomes the so-called residual layer (RL). Stratification in the RL is neutral but the RL is not convective anymore, as compared to the ML.

During the morning transition, the surface net energy flux switches back to positive values after sunrise. A new mixed layer starts to build from the ground, growing in height and replacing the SBL. Eventually, the new ML connects to the RL and the two layers form one new ML together.

In the case of non-ideal fair weather conditions with weaker solar forcing, an elevated stable core above the ML can remain throughout the day. This phenomenon can especially be observed in deep valleys. There, the reason for the one or more stable cores is not necessarily weaker solar forcing but the stable stratification induced by circulation cells in the valley as explained in the paragraph about slope winds in section 1.2.2.

Mountain boundary layer In mountainous terrain, an additional distinction of elements in the ABL structure as shown in Fig. 1.2 is convenient. The slope atmosphere with up- and downslope winds develops closest to the terrain surface. In valleys, an additional valley atmosphere with up- and downvalley winds is on top. The mountain atmosphere covers the whole mountainous area, with plain-to-mountain or mountain-to-plain winds. All these winds can interact as is implied in Fig. 1.3.

Besides the distinction of multiple layers in the MoBL with different spatial scales, a larger range of temporal scales beyond the classical one-hour threshold defined by Stull

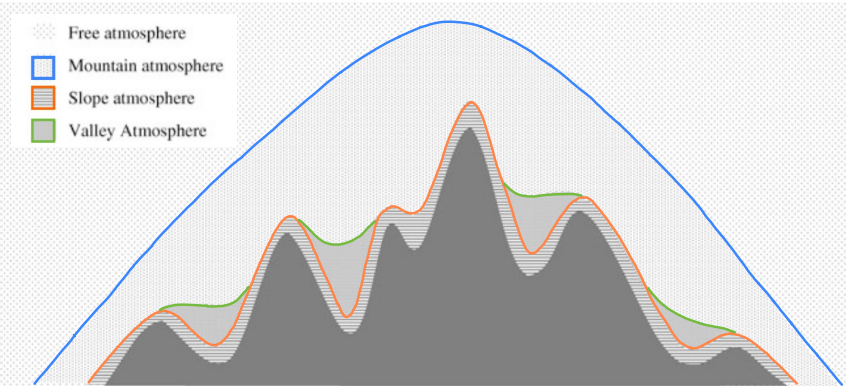

Figure 1.2: Mountain boundary layer with slope atmosphere, valley atmosphere, and mountain atmosphere below the free atmosphere. Adapted from Zardi and Whiteman (2013) which is based on Ekhart (1948).

(1988) should be included in the definition of the MoBL. Lehner and Rotach (2018) extended Stull's 1988 definition and proposed to define the MoBL as "the lowest part of the troposphere that is directly influenced by the mountainous terrain, responds to surface and terrain forcings with timescales of one to a few hours, and is responsible for the exchange of energy, mass, and momentum between the mountainous terrain and the free troposphere". In the MoBL, certain wind systems such as explained in section 1.2.2 can occur.

1.2.2 Regional and local winds in alpine valleys

There are many wind systems specific to mountainous terrain. Two of them are presented in this section as they occurred during the measurement period described in section 2.1.

Thermally-driven winds

In idealized HHF terrain, temperature is horizontally equal for stationary conditions, only in the vertical, temperature differences can exist. In sloped terrain, these horizontal temperature contrasts are associated with horizontal pressure gradients that produce local flows which are called thermally-driven winds.

Slope wind During daytime, incoming radiation heats the ground and sensible heat flux convergence warms the air adjacent to the ground. In sloped terrain, an air parcel close to the ground will thus become warmer than another parcel at the same altitude further away from the slope. During nighttime, the opposite is true: the ground cools, and the adjacent air cools by sensible heat flux divergence. Consequently, an air parcel close to the slope becomes cooler than its equally elevated counterpart at a distance from

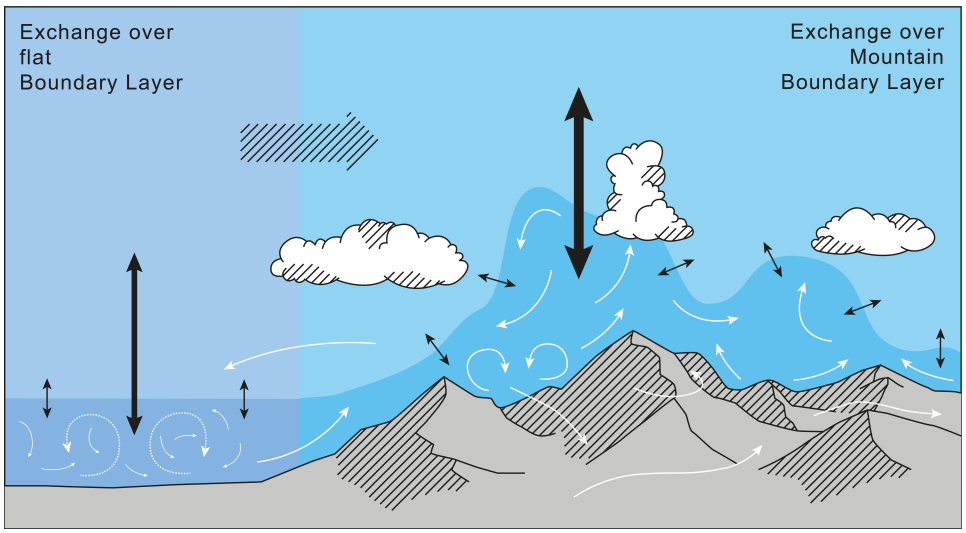

Figure 1.3: Wind systems and exchange processes in flat and in mountainous terrain. White arrows indicate processes (mainly) within the boundary layer. Black arrows indicate exchange between the boundary layer and the free atmosphere above. Taken from Serafin et al. (2020).

the slope. Buoyancy force leads to an upslope (anabatic) flow during daytime and a downslope (katabatic[1]) flow during nighttime (Whiteman 2000).

While moving along the slope, air parcels cool (warm) adiabatically during ascent (descent) and would soon reach their level of neutral buoyancy relative to air outside the slope layer without any further effects. Hence, they would stop their along-slope movement. However, air parcels in the slope layer are usually subject to continuous heating (cooling) from the surface below. Such steady state movement along the slope can only persist if energy sources and sinks of an air parcel in the slope layer are balanced. Prandtl (1944) described this balance relating sensible heat flux convergence (divergence) and temperature advection – advection of potentially cooler air by upslope winds and advection of potentially warmer air by downslope winds.

Slope flows are partially compensated by return flows. One part is a return flow right above the slope-wind layer, running in the opposite direction of the actual slope flow (Prandtl 1944). Another part is the subsidence above the valley center. Together with the upslope flow, it forms a "cogwheel"-like circulation during daytime. The subsiding air warms the valley atmosphere, forming an elevated stable layer above the mixed layer in the valley (Vergeiner and Dreiseitl 1987). Multiple circulation cells with their respective stable layers can be stacked on top of each other (Wagner et al. 2014, 2015a). During nighttime, downslope flows can be partially compensated by rising motions in the valley core, cooling the valley atmosphere (Zardi and Whiteman 2013). A third portion is not compensated but detrained from the slope and valley atmosphere into the mountain atmosphere during

[1]not to be confused with the large-scale katabatic flows over ice domes such as in Greenland or Antarctica which are influenced by Coriolis force (Zardi and Whiteman 2013)

daytime or entrained into the slope and valley atmosphere from higher levels during nighttime. The detrainment during daytime is part of the "mountain venting" where air is transported towards mountain crests and above them by thermally-driven winds (Serafin et al. 2018).

Models for slope winds Prandtl (1944) developed a simplified slope wind model containing a characteristic depth

$$D = \left(\frac{4 K_M K_H}{N^2 \, sin^2(\alpha)} \right)^{1/4} \tag{1.1}$$

from which the slope wind depth can be estimated as $\pi \, D$. N is the Brunt-Väisälä frequency, describing stability, and α is the slope angle. From the equation, it can be seen that characteristic depth decreases with increasing slope angle. Equation (1.1) contains eddy diffusion coefficients for sensible heat (K_H) and momentum flux (K_M). These quantities can span multiple orders of magnitude – for instance, Stull (1988) reports values from 0.1 to 2000 $\mathrm{m^2 s^{-2}}$ – and they are usually not known in real-world applications. This makes it hard or even impossible to estimate a characteristic slope wind depth for a given slope using Prandtl's model without further information about the coefficients. Instead, the coefficients are often used as tuning parameters to make Prandtl's slope wind model fit observations (Defant 1949). Vergeiner and Dreiseitl (1987) extended Prandtl's model and described the "cogwheel"-like circulation, as mentioned above. Schumann (1990) performed the first numerical simulations of upslope flows using LES. Downslope flows were not treated in his simulations because the associated smaller-sized eddies could not yet be computationally resolved at the time. Zardi and Whiteman (2013) evaluated observations and report typical maximum upslope (downslope) wind speeds of $1-5\,\mathrm{m\,s^{-1}}$ ($1-4\,\mathrm{m\,s^{-1}}$). Horst and Doran (1986) provide an observation-based rule of thumb for the depth of the temperature deficit layer in downslope wind regimes being approximately 5% of the vertical drop of the slope. However, this rule was applied at night to one specific slope being relatively uniform, having slope angles not steeper than 21°and is not applicable to the slopes analyzed in this study.

Along-valley wind On a larger scale, a similar rule holds for valley winds[2] as for slope winds if the synoptical forcing is weak: winds blow upvalley – or into the valley, for non-sloped valley floors – during daytime, and downvalley – or out of the valley – during nighttime. Valley winds are driven by horizontal pressure differences which result from horizontal temperature differences (Zardi and Whiteman 2013). Multiple mechanisms play a role in forming those temperature differences.

[2] "Valley winds" will be used synonymously to "along-valley winds", otherwise they will be explicitly called "cross-valley winds".

One major effect is the valley-volume effect (Whiteman 2000; Schmidli and Rotunno 2010; Schmidli 2013a), based on the topographic amplification factor concept by Wagner (1932). The volume of air in a valley is smaller than the volume of air over the adjacent plain, considering volumes of equal depth. The solar energy input per horizontal unit surface area is assumed to be the same, but the volume of air to be heated by that energy input is smaller in the valley. Hence, the air in a valley will reach a certain volume-averaged temperature earlier than the air above the plain. Comparing the integrated columns of air in the valley and over the plain by pressure yields a pressure gradient force from the plain to the valley.

The transport of heat to a valley is more effective than over a plain since not only convection leads to warming of air at a certain level but also advection (Zardi and Whiteman 2013). The advection induced by upslope winds is an advection of potentially cooler air from lower levels, hence, it is a cooling mechanism (as is the case for daytime upvalley winds advecting cooler air from the plane). Instead, the compensatory subsidence of air at the valley center is a warming mechanism. As long as the cross-valley circulation remains below crest height, the warming and cooling mechanisms balance each other. Energy is introduced only by solar forcing and the heat is redistributed by the circulation. However, if the cross-valley circulation reaches above crest height, energy can be transported to higher levels, being removed from the valley volume. Schmidli (2013b) conducted simulations using the bulk perspective, confirming the export of heat from the valley atmosphere as a net effect of the cross-valley circulation.

Another advection process is related to upslope flow encountering an elevated stable layer. The upslope flow detaches from the slope and moves horizontally towards the valley center, leading to net warming of the valley atmosphere. However, this warming by detrainment from the slope wind layer is usually small (Schmidli 2013a).

Another circumstance leading to more effective heating of the valley air is the protection from mass and heat exchange with upper-level air by surrounding topography (Zardi and Whiteman 2013). However, the presence of topography can lead to thermally-driven winds which do not hinder but promote exchange.

The valley wind reversal is delayed with respect to surface energy budget reversal and slope wind reversal because first, the valley atmosphere needs to be heated – partially supported by the slope wind circulation. Then, if part of the valley atmosphere is heated enough, the along-valley pressure gradient becomes large enough to set the valley wind system into motion. Moreover, in the morning, an elevated core of downvalley winds can be sustained while upslope winds have already set in. Similarly, an elevated core of upvalley wind can be sustained during the evening transition when downslope winds have already set in (Schmidli and Rotunno 2010).

Mountain-plain wind The mountain-plain wind circulation, also called "Alpine pumping" for the European Alps (Graf et al. 2016), is driven by a similar mechanism as the slope winds: horizontal pressure differences are created between mountain massif and adjacent plain due to horizontal temperature differences. Stronger heating during daytime (cooling during nighttime) leads to a thermal low (high) over the mountain massif, provoking plain-to-mountain winds (mountain-to-plain winds; Zardi and Whiteman 2013). Lugauer and Winkler (2005) introduced the term "Alpine Pumping" to describe the combination of the slope, valley, and mountain-plain wind system in the European Alps and the Alpine foreland.

Return flows The slope, valley, and mountain-plain winds are compensated by flows at greater heights. Wind speeds of compensating flows are usually low as the return flows extend over a larger volume than their spatially more constrained counterparts (Whiteman 2000). The compensatory flows for valley and mountain-plain winds are often so weak that they are overruled by synoptic-scale winds (Zardi and Whiteman 2013).

Transition between regimes Between day and night, a transition from flow up the terrain to flow down the terrain takes place. The smaller the scale, the shorter the response time, because the smaller the mass is which reacts to a certain heating or cooling rate. Additionally, less mass needs to be set into motion. Hence, first slope winds reverse their direction, then valley winds, then mountain-plain winds (Zardi and Whiteman 2013).

Cross-valley wind A fourth type of thermally-driven wind is a cross-valley circulation. It can occur in valleys whose flanks are not equally exposed to the sun. Typically, one flank is illuminated by the sun while the other flank is in the shade. The sunny flank will experience upslope flow whereas air above the shady flank will rather flow downslope. At higher levels, air flows from the sunny towards the shady flank, closing the circulation (Hennemuth and Schmidt 1985; Hennemuth 1986).

Dynamically-driven cross-valley motion can be induced by valley curvature. Centrifugal force acting on along-valley flow makes air move up the slope at the outer edge of the curve ("outer" from the perspective of the along-valley flow). The across-valley pressure gradient in the lower part and the upper part of the valley is from the outer to the inner edge of the curve. Two types of cross-valley circulations can establish. One type is the circulation driven by the upper-level pressure gradient with cross-valley motion from the outer edge of the valley curve to the inner edge of the valley curve at the upper level, and from the inner to the outer edge close to the ground, as observed in the Inn Valley (Babić et al. 2021). The other type is the circulation driven by the lower-level pressure gradient, resulting in the sense of rotation opposite to the first type. This second type was observed in the Riviera Valley (Weigel and Rotach 2004).

Idealization versus reality The previously given description of thermally-driven winds is idealized. Local inhomogeneities such as varying land coverage (meadows, shrubs, rocks, snow, etc.), varying slope angle, varying solar exposure or areas falling into shade can strongly modify them, especially the small-scale slope winds (Lehner and Gohm 2010). Additionally, thermally-driven wind systems can interact with each other so that slope and valley winds may be hard to distinguish (Hennemuth and Schmidt 1985). The increasing complexity inhomogeneities introduce is the reason why rather homogeneously shaped and covered mountain areas are usually favored for research experiments (Zardi and Whiteman 2013). This was also one of the major reasons for the measurement location that was chosen in this study.

Downslope windstorms

One sub-type of dynamically-driven winds are downslope windstorms. They are associated with high wind speeds and gustiness on the leeward side of an obstacle. Wind speeds two to three times higher than at crest level have been observed on lee slopes (Jackson et al. 2013).

For downslope windstorms to occur, multiple prerequisites are needed. A mountain barrier and stable stratification are required (Jackson et al. 2013). However, stratification may not be too strong either in order for the air masses to actually cross the barrier instead of being blocked or flowing around (Whiteman 2000; Jackson et al. 2013). Additionally, sufficiently strong cross-barrier winds, a hydrostatic pressure gradient, or both trigger the movement of air from one side of the barrier to the other.

There are multiple mechanisms to explain downslope windstorms. The main three ones include hydraulic theory (e. g. Long 1954; Durran 1986), wave amplification by constructive interference after reflection at a pre-existing critical layer (Klemp and Lilly 1975), and a similar reflection at a self-induced critical layer (Peltier and Clark 1979).

Downslope windstorms can be warm or cold winds. If the replacing air is warmer than the replaced air, a cold-air pool is usually eroded (e. g. Haid et al. 2020, 2022; Umek et al. 2021, 2022). There are two main warming mechanisms (Sprenger 2022), one of which is isentropic drawdown: the replacing air often originates from upper levels (with higher potential temperature if stratification is stable) and warms adiabatically during lee slope descent being warmer than the replaced air. The other important process is latent heating when clouds are formed on the upstream side of the barrier and part of the moisture content is removed from the air mass by precipitation. Additional mechanisms such as mechanical mixing and radiative heating can also play a role (Elvidge and Renfrew 2016).

In the central European Alps where measurements for the study at hand were conducted, the regional name for downslope windstorms is foehn. The most typical foehn types are south foehn (Jansing et al. 2022) and north foehn (e. g. Zangl 2006; Cetti et al.

2015) as the main Alpine crest is west-east oriented, even though foehn from other directions on non-west-east-oriented slopes can occur, as well (Saigger and Gohm 2022). North foehn occurs on the southern side of the main crest or other sufficiently large west-east-oriented mountain ridges, south foehn on the northern side. Deep south foehn is usually caused dynamically by geostrophic winds with a component perpendicular to the Alps such as is often the case for the leading edge of low-pressure systems approaching central Europe from the West. Typically, the flow ahead of the cold front generates so-called pre-frontal foehn (Heimann 1992). Shallow foehn is mainly caused by a pressure gradient force across the mountain barrier, that may have a geostrophic component and a hydrostatic component, the latter due to different air masses on either side of the Alps (Gohm and Mayr 2004).

Foehn winds can interact with valley winds as can for example be the case in the Inn Valley (Adler et al. 2021). They can cause a valley wind direction reversal, for example, daytime upvalley flow can be overruled by foehn, leading to a downvalley flow (Gohm et al. 2009).

Lakes in mountainous areas

The presence of lakes or other water bodies in mountainous areas can impact the characteristics of the adjacent atmosphere (Chazette et al. 2021) such as composition and stratification. Furthermore, a lake breeze can develop (Gerken et al. 2014), similar to a sea breeze: temperature differences between land and water lead to temperature differences of the adjacent air and thus to a pressure gradient, driving a daytime breeze from water to land and a nighttime breeze from land to water. If a lake is too small to warm or cool enough air for a long enough time (given non-zero mean wind) in order to generate a pressure difference, no breeze develops. Yet, these small water bodies can still affect the moisture distribution, the surface energy budget, and thermally-driven winds (Sturman et al. 2003) such as larger water bodies do (Laiti et al. 2014).

1.2.3 Meteorological measurements with UAS

The meteorological phenomena presented in sections 1.2.1 and 1.2.2 can be investigated experimentally with a multitude of instruments. One rather new kind of measurement instruments are uncrewed aerial systems (UAS), sometimes also called uncrewed aerial vehicles (UAV), remotely piloted aircraft systems (RPAS), or simply drones.

History UAS have been used in the context of atmospheric sciences already for decades. For example, the first drones at DLR to fulfill meteorological purposes were built in 1967 (Schumann 2012).

Advantages Drones come with a lot of advantages as opposed to other measurement techniques, one of which is that they are spatially more flexible than surface stations or towers (Wetz et al. 2021). Furthermore, drones are cheaper and more maneuverable than large aircraft. For instance, they can fly closer to the ground and in spatially more constrained areas (Serafin et al. 2020). As compared to lidars, UAS measure in-situ instead of collecting data remotely which requires averaging over an area and assuming homogeneity and stationarity (Wetz et al. 2021; Wildmann and Wetz 2022).

Disadvantages Despite their technical ability to reach heights greater than 120 m AGL (depending on the height above mean sea level), UAS flights in the "open" category are only permitted up to a height of 120 m AGL, following European law. Flying above, or within controlled air space, or with a fleet of multiple drones controlled by a single pilot, requires special permission. Small and lightweight UAS are well suited to resolve small meteorological scales but they cannot carry heavy loads (Serafin et al. 2020), which means there is an upper limit to battery capacity and consequently to flight time. The duration of flights performed within this study did not exceed 20 minutes. To overcome this challenge, one UAS can be replaced by another to continue the measurement at a given location (Wildmann and Wetz 2022). Moreover, evolution in the battery industry and in UAS design might allow longer flight times in the future.

UAS types A frequently used UAS type is the fixed-wing aircraft with attached sensors measuring boundary layer parameters (Reuder et al. 2009), sometimes with specific applications such as wind energy research (Wildmann et al. 2014) or the investigation of diurnal mountain winds (Egger et al. 2002). More recently, another type of UAS has undergone great development: multicopters. They, too, are suitable for meteorological purposes (Palomaki et al. 2017), and particularly for the investigation of diurnal mountain winds (Bailey et al. 2023). An advantage of multicopters over fixed-wing UAS is the copters' ability to hover at a certain location and to move at a very low speed. A disadvantage is that most of the lift needs to be generated by motor thrust as compared to fixed-wing UAS which generate part of the lift aerodynamically while gliding. Hence, operation times for multicopters are usually shorter than for fixed-wing UAS operated at the same weight and with the same battery capacity. Depending on the sampling area, it can also be an advantage that multicopters only need a small space for take-off and landing as compared to fixed-wing UAS (Wetz et al. 2021).

UAS fleet In order to obtain simultaneous, spatially distributed measurements of the airflow, *multiple* drones can be operated as a fleet. One of these fleets is the SWUF-3D (Simultaneous Wind measurement with Unmanned Flight Systems in 3D) quadrocopter fleet that was also used in this study. The fleet was first deployed in heterogeneous, flat

terrain in the vicinity of a meteorological measurement tower for calibration and validation purposes (Wetz et al. 2021).

The ESTABLIS-UAS project aims to capture wind and turbulence structures in the ABL using the SWUF-3D fleet. Wind tunnel tests, field experiments, and virtual measurements in numerical simulations are envisaged to develop accurate wind and turbulence retrieval algorithms (Wildmann et al. 2022). Field experiments have been performed over flat, inhomogeneous terrain to investigate the spatial correlation and coherence in the ABL (Wetz et al. 2023), Wetz and Wildmann (2023) analyzed the turbulent flow in a wind turbine wake. Wind tunnel experiments have been conducted and were being evaluated at the time this Master's thesis was handed in.

Another location to measure atmospheric flow and turbulence quantities by the SWUF-3D fleet is mountainous terrain. The airflow was sampled during the TEAMx-PC22. SWUF-3D measurements in complex terrain are to be extended in the future in the framework of the TOC (Serafin et al. 2020).

1.3 Goals and outline

In the framework of TEAMx-PC22, a side valley of the Inn Valley was tested as a potential measurement location for the TOC. In this thesis, two questions shall be answered in this context:

1. Which meteorological phenomena can be detected at Nafingalm by the instrumentation used during TEAMx-PC22?

2. Which UAS flight patterns are suitable to investigate the valley atmosphere of Nafingalm?

After having introduced the state of knowledge about the mountain boundary layer as well as regional and local winds in an alpine valley in chapter 1, the methodology of the TEAMx-PC22 at Nafingalm will be explained in the next chapter. In chapter 3, the synoptic weather situation during the measurement campaign from 20 to 28 June 2022 is described. Then, a case study is done for 23 June 2022, analyzing different phases of the day in detail based on UAS data. In chapter 4, the results of the case study are discussed. In chapter 5, the main findings are summarized and an outlook is given on what might be improved and investigated in a future campaign with respect to methodology and remaining scientific questions.

Chapter 2

Methods

In this chapter, information on the measurement location and period is given. Then, the instrumentation and measurement strategy are explained. Finally, the processing of observational data and the reanalysis and forecast data used in section 3 are explained.

2.1 Measurement location and period

Measurements in the framework of the TOC will be conducted at several target areas across the Alps from North to South, one of which being the Inn Valley (Serafin et al. 2020). A sub-target area within the Inn Valley is Kolsass, a town located east of Innsbruck (cf. Fig. 2.1). Airflow in the Inn Valley is partially influenced by flow in and out of its tributary valleys (Deidda 2023). One of these tributary valleys is the Weer Valley, opening near Kolsass. One of the valley heads of the Weer Valley is Nafingalm. Nafingalm is another TEAMx sub-target area. It is an Alpine pasture with a size of approximately $2\,\mathrm{km} \times 2\,\mathrm{km}$ with several creeks and a lake (the Nafingsee, or Nafing Lake) in the center at approximately 1921 m above mean sea level (AMSL), displayed in Fig. 2.2, with a close-up of the central lake area in the lower left panel. The lake measures approximately 180 m in north-south direction and 70 m in west-east direction. Towards the northwest, Nafingalm opens in the direction of the Weer Valley. Towards the west, south, and east, the pasture is surrounded by mountain ridges with the highest peaks at approximately 2500 m AMSL. A pass, Geiseljoch, is embedded in the southern crest. Geiseljoch is almost 2300 m AMSL and leads to Tux Valley which is connected to Ziller Valley. The largest creek in the area flows from below Geiseljoch towards the lake, forming a marshy delta south of the lake where creeks from the western and eastern flanks converge with the main creek. One of those tributary creeks from the east is displayed in the map in Fig. 2.2 as it becomes important in the data analysis. The direct distance to the Alpine main crest in the south is approximately 25 km.

There are three main measurement areas which will henceforth be called measurement area (1) north of the lake (northernmost orange and purple dot in Fig. 2.2), (2) at the

southern lake shore (orange, yellow, and red dots close to the southern lake shore in Fig. 2.2), and (3) at the delta (orange and red dots in the southernmost area of the marshland in Fig. 2.2).

Nafingalm was chosen as a measurement site because it is large enough to presumably have its own valley wind system while it is also small enough to be sampled with UAS, surface stations, and possibly lidar in the future. Moreover, the topography is assumed to be homogeneous enough for future numerical simulations, although the steepness of the valley side walls may be a challenge. Slope angles of the surrounding mountain flanks are relatively similar, from 26° to 34°, except for the southern flank along the main creek, which has an average slope angle of 16°. The vegetation is nearly homogeneous with a canopy height of mostly less than 0.5 m. Inhomogeneity is introduced by a few gullies and ridges at the valley side walls potentially deflecting slope winds (i e. converging downslope winds in the gullies, converging upslope winds over the ridges), at least for low-wind conditions. The most prominent inhomogeneity at Nafingalm is the lake which potentially modifies latent and sensible heat fluxes (Zardi and Whiteman 2013).

The measurements evaluated in this study took place in the framework of the TEAMx-PC22 (Pfister et al. 2023). Measurements at Nafingalm were conducted between mid-June and mid-September 2022.

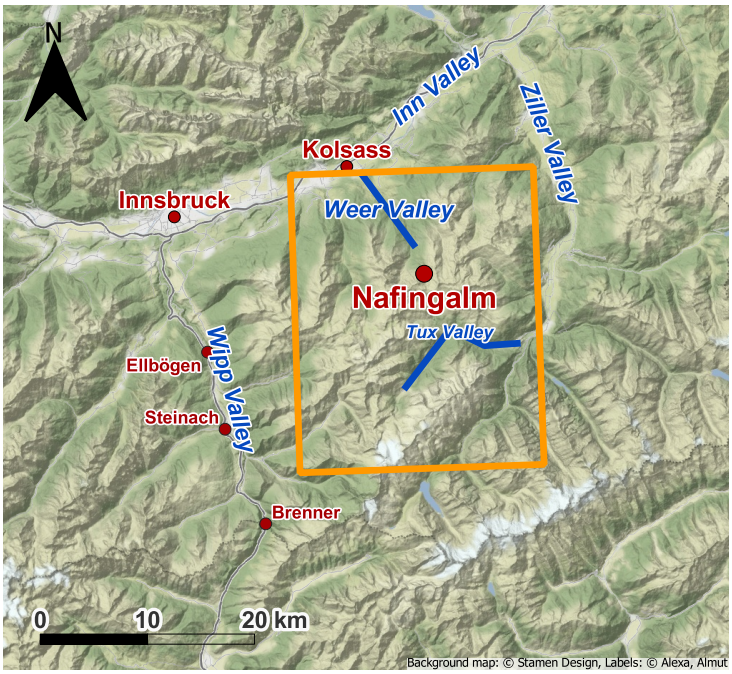

Figure 2.1: Map of the Alpine area around Nafingalm. The locations Nafingalm, Kolsass, and Innsbruck are three of the sub-target areas of the TEAMx program (Serafin et al. 2020). Ellbögen, Steinach, and Brenner are locations prone to south foehn through the Wipp Valley (cf. section 3.1). The orange rectangle is the domain in which forecast data of the COSMO-1E model are regarded (cf. sections 2.4 and 3). Map created with QGIS version 3.22. Map tiles by © Stamen Design, under CC BY 3.0. Data by OpenStreetMap, under ODbL.

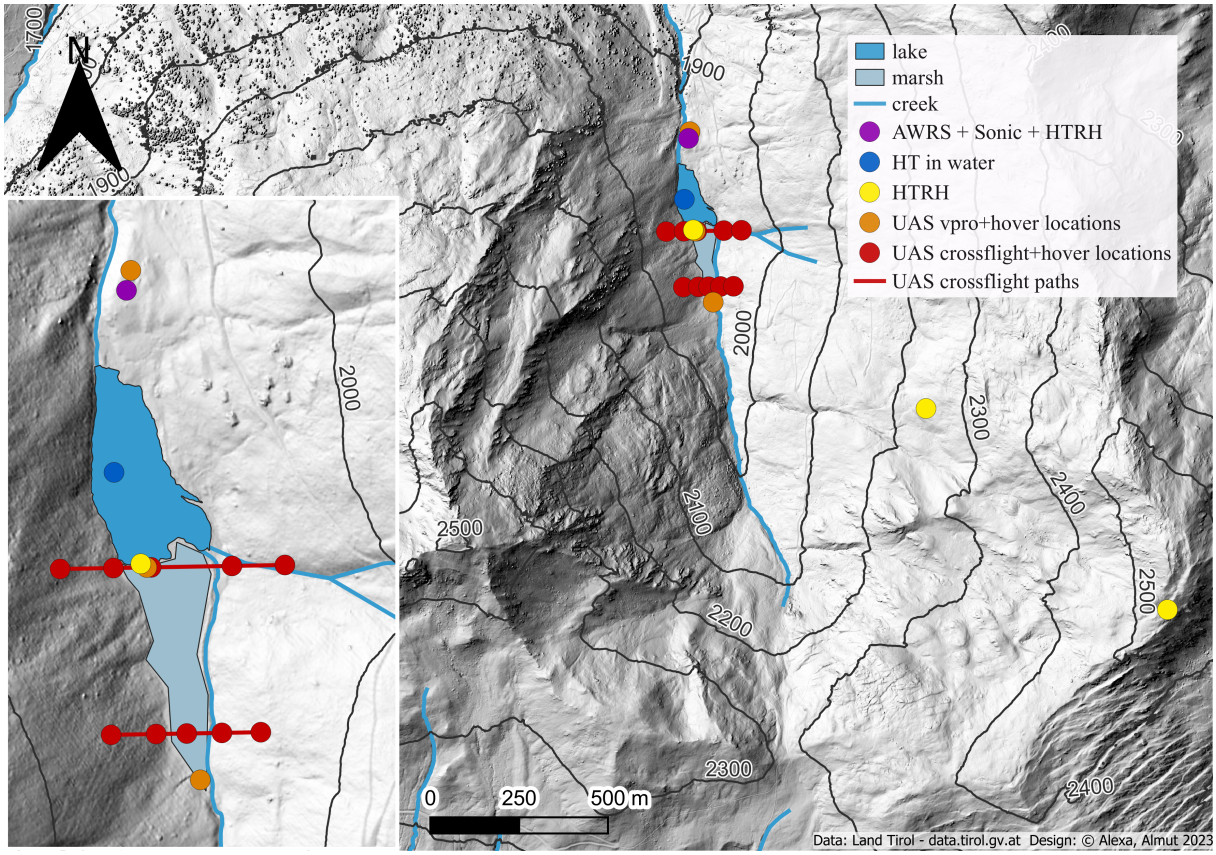

Figure 2.2: Map of Nafingalm with instrumentation. Lower left: close-up of the lake area. Only the creeks most relevant to this study are shown. Figure created with QGIS version 3.22. Map tiles are 1 m DSM-data from 2007-2008 provided by Land Tirol - `data.tirol.gv.at`.

2.2 Ground-based instrumentation

An overview of all instrumentation used at Nafingalm during TEAMx-PC22 can be found in table B.1 in the appendix. The ground-based instrumentation is explained in detail in this section.

AWRS An automatic weather and radiation station (AWRS) was positioned close to the northern shore of the lake on a gentle hill at 7 m above lake level (purple dot in Fig. 2.2). The goal was to have a surface station close to the lake on solid (not too marshy) ground, and exposed to undisturbed valley in-/outflow. The station was composed of three separate measurement systems: two automatic weather stations and a radiation station combined with soil measurement devices to determine ground heat flux. Figure 2.3a shows the respective measurement tower on the left-hand side of the panel). Pressure p, temperature T, relative humidity RH, wind speed U, and wind direction Ψ were measured at 0.8 and 4 m AGL, respectively and their average values were output every 5 min. Two rain gauges positioned on the ground measured the accumulated rain rate RR in mm per 5 min.

Wind speed and direction were detected by two 03002 R.M. Young Wind Sentry Set devices. The booms the wind measurement devices were attached to were directed towards 255° and the devices were aligned with the boom because orienting the sensors towards the north would have required considerably more time and effort when setting up the AWRS. Hence, wind direction had to be corrected (measurement of 0°corresponded to actual 255°). Between 352° and 360° of measured wind direction, the devices have an electrical dead band. Since the device outputs data averaged over 5 min, and the dead band is already taken into account internally, the averaged values in this range of angles do not need to be discarded in the output dataset. Wind speeds below $0.5\,\mathrm{m\,s^{-1}}$ were discarded due to the inertia of the anemometer.

Net short-wave radiation was detected by two Apogee SP-110 pyranometers, but a separate CNR4 Net Radiometer measured both shortwave and longwave radiation for top and bottom half-space ($R_{\mathrm{SW}\uparrow}$, $R_{\mathrm{SW}\downarrow}$, $R_{\mathrm{LW}\uparrow}$, $R_{\mathrm{LW}\downarrow}$) which is why only the CNR4 data were used during data analysis. The soil measurements included a Heat Flow Transducer (HFT3) Soil Heat Flux Plate at 11 cm below the Earth's surface, soil thermometers measuring T_{soil} at 2.5 at 6.5 cm depth, and an SM300 soil moisture and temperature sensor to determine volumetric soil moisture M_{soil} in % between 3.5 and 5.5 cm depth. The AWRS measured from 15 June to 12 September 2022. The collected data were made publicly available by Gohm and Obleitner (2023). Further datasets of measurements during the TEAMx-PC22 are collected in the TEAMx community (TEAMx Community 2022).

HOBO Furthermore, several battery-powered Onset HOBO MX2302 temperature and humidity sensors (henceforth called HTRH) equipped with a radiation shield RS3-B were distributed in the area. They measure temperature and humidity and were programmed to output instantaneous absolute temperature, relative humidity, and dewpoint as well as an averaged value for absolute temperature and relative humidity every 5 min. Some of them were complemented with an Onset HOBO MX2201 Pendant waterproof temperature sensor (henceforth called HT) equipped with a homemade double plate radiation shield to measure land surface temperature. The HT was programmed to output values of instantaneous and averaged absolute temperature every 5 min. An example of such a HOBO station can be seen in Fig. 2.3b).

Two of the HTRH sensors were added to the AWRS station, one at 2 m and one at 0.3 m AGL. A HOBO station with HTRH sensors only was set up directly at the southern shore of the lake with two HTRH at 2 m AGL, one HTRH at 0.3 m AGL, and one HT at the ground. This station will be referred to as "HOBO lake station". Two further HOBO stations were installed at higher elevations, one on the slope and one at crest height. One of these stations, similarly equipped as the one at the southern lake shore, was installed at about half of the crest height (2241 m AMSL). This station will be referred to as "HOBO slope station". The third HOBO station, consisting of a single HTRH, was

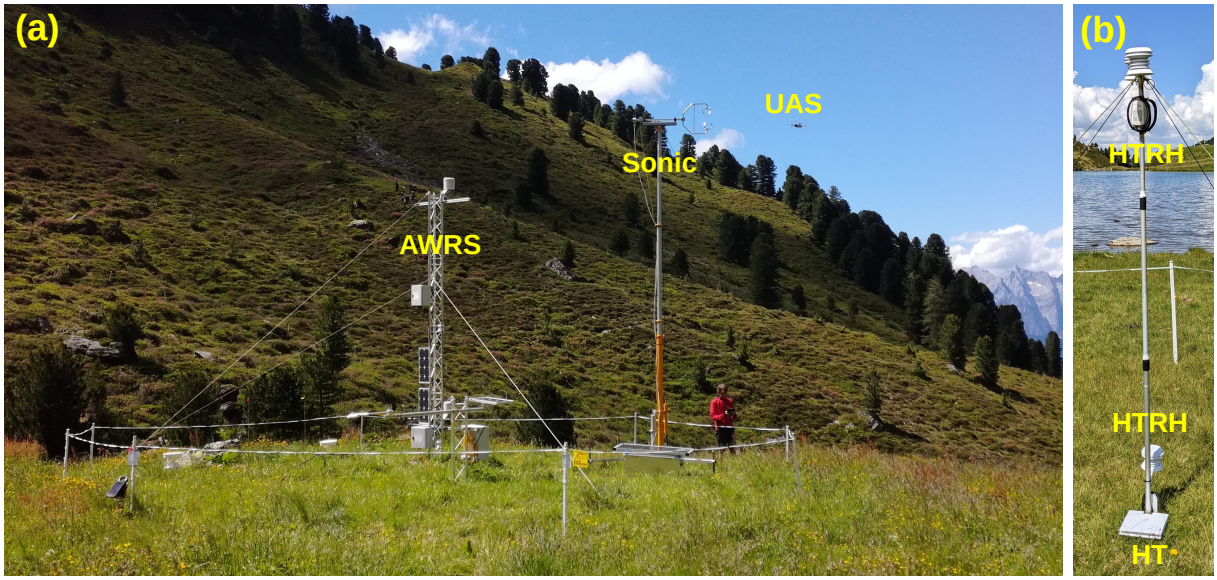

Figure 2.3: **(a)** The collection of instruments north of the lake. The view is towards the northwest. The left one of the two towers is the AWRS with additional HOBO sensors attached. The radiation station is set up in front of the left tower. The tower to the right has the sonic anemometer attached at its top. To the right of the sonic anemometer, a UAS is flying, controlled by one of the researchers standing nearby (it is to be noted, however, that this specific UAS does not belong to the SWUF-3D fleet). Photograph taken by the author. **(b)** HOBO station at the southern shore of the lake. The view is towards the north. Two HTRH sensors are attached at 2 m AGL and one is attached at 0.3 m AGL. An HT sensor is at the ground, shielded from solar radiation by a homemade plate. Credits: Norman Wildmann, adapted photograph.

mounted on top of a signpost on the crest at 2531 m AMSL, approximately 40 m below the peak of Mount Halslspitze. The three HOBO stations are marked by yellow dots in Fig. 2.2. The two higher-level HOBOs were aligned along an axis towards the southeast, seen from the HOBO station at the southern lake shore, to measure temperature and humidity within the slope wind layer, and to obtain a pseudo vertical temperature profile providing information about stratification in the valley as computed by Viebahn (2023). This axis was chosen since the locations to mount the HOBO stations were relatively easily accessible from the nearby hiking trail. The alignment of HOBOs along the valley axis up to Geiseljoch might have been even more informative but the poorer accessibility of the area halfway up the slope would have made the installation more challenging. Two of the waterproof HT sensors were installed within the lake at 0.3 and 1 m depth, hanging from a tethered buoy. They did not have any radiation shields. The position was closer to the western shore of the lake where the lake is deeper and where water temperature was expected to be most representative of the lake.

The HOBO sensors were deployed in a time period from 16 June to 12 September 2022. The collected data were made publicly available by Gohm (2023).

To make the moisture quantity independent of temperature, relative humidity was converted to water vapor mixing ratio. The computation was done using the method described by Viebahn (2023), approximating barometric pressure at sensor level by the barometric formula. For the purpose of this study, the mixing ratio was calculated for the HOBO stations 2 m above the ground at the southern lake shore, on the slope, and at the crest.

Sonic anemometer A 3D ultrasonic anemometer (type "Metek USA Class A sonic anemometer"; henceforth only called sonic anemometer) was installed next to the AWRS at a height of 5 m AGL for the period 20 – 28 June 2022. The sonic anemometer measures the u, v, and w-component of the wind and absolute virtual temperature T_v at a frequency of 10 Hz. The tower that the device was attached to can be seen in Fig. 2.3a) on the right-hand side. The boom was directed towards 42° , deviating from its default orientation of 180° . Hence, wind direction and the horizontal wind components had to be corrected.

To compute TKE from the sonic data, a rolling mean of 30 min was used. On the one hand, the averaging period should be long enough to account for convective conditions. On the other hand, the averaging period should be short enough to avoid covering multiple wind regimes (e. g. upvalley flow and foehn) in one period. To compare the sonic anemometer data to AWRS and HOBO data, 5-minute average values were computed.

2.3 Airborne instrumentation: UAS

Similar to the deployment period of the sonic anemometer, UAS measurements were conducted between 20 and 28 June 2022. Some days were rainy and therefore not usable for UAS measurements. Flights were performed on 20, 21, 22, 23, 26 and 27 June 2022.

The drones were deployed at three different locations as mentioned in section 2.1, indicated by the orange dots and red lines in Fig. 2.2. The photo in Fig. 2.4 shows an example of a pilot controlling a drone near the measurement location north of the lake.

The protocol of all UAS flights can be found in table C.1 in the appendix. Data of vertical profiling flights and fixed-point measurements are published by Wildmann et al. (2023).

Seven UAS were taken to Nafingalm, and up to three UAS were deployed simultaneously. When problems occurred with one UAS, it was replaced by another one. The maximum UAS fleet size was three drones due to the availability of a maximum of three pilots at a time. According to EU regulation 2019/947 in the open category of UAS operation, each drone had to be controlled by one pilot. Each UAS was programmed to perform its flight in auto-pilot mode. Only in exceptional cases, the UAS needed to be controlled manually. For the TOC, it is envisaged to operate multiple drones by one pilot which will require special permission.

Figure 2.4: The author controls a drone near the measurement location north of the lake. The view is towards the south.

Flight plans were created using Python scripts and the software © QGroundControl (QGC) developed by the Dronecode Foundation (Gagne et al. 2023). QGC was also used to control the UAS during operation.

2.3.1 UAS – meteorological parameters

The main meteorological quantities measured by UAS are absolute temperature, relative humidity, barometric pressure, and the attitude of the drone. From these data, horizontal wind speed and horizontal wind direction can be derived. Furthermore, other moisture quantities such as the water vapor mixing ratio can be computed. Different types of data are recorded at different frequencies as explained by Wildmann and Wetz (2022), the highest recording frequency being 250 Hz for accelerometer data, the lowest being 1 Hz for temperature and humidity data. In the post-processing of the TEAMx-PC22 flights, the output data sampling frequency was set to 20 Hz.

Temperature and humidity Measuring meteorological variables on drones has often been achieved by attaching external sensors (e. g. Shimura et al. 2018). For the SWUF-3D fleet, this was indeed done for temperature and relative humidity, using an IST HYT 271 sensor sampling with a frequency of 5 Hz. However, sensor inertia causes an effectively coarser resolution than 0.2 s. The hysteresis was corrected by time constants, sometimes also called lag coefficients, of 4 s for temperature and 3 s for humidity.

Figure 2.5: UAS on top of its box, in preparation for take-off. The pin pointing away from the nose of the UAS on the left-hand side is the temperature and humidity sensor, protected against direct sunlight by a white shield. Credits: Tamino Wetz, adapted photograph.

Wind As opposed to temperature and humidity, for horizontal wind, the drone itself is used as a measurement instrument. Payload in the form of additional sensors would increase the system's weight and would reduce flight time, or a larger drone would be needed which disturbs the flow more and can thus only resolve larger scales.

The UAS used in the ESTABLIS-UAS project are Holybro QAV250 racing drones which quickly react to changes in attitude or position (photo in Fig. 2.5). The drones hold their position while hovering by relying on the estimated system state with an accuracy of 0.19 m horizontally and 0.85 m vertically (Wetz et al. 2021). Fast reactions and position accuracy are important for a highly resolved and precise wind vector.

The UAS used in this study are operated in weather-vane mode, orienting themselves automatically towards the current wind direction. The direction is measured by a magnetometer. The declination (deviation of magnetic north from geographic north) is not corrected for in the data analyzed in this study. The error was on the order of 4° for central Europe at the time the measurements in the framework of this study were done (NCEI Geomagnetic Modeling Team and British Geological Survey 2019). The horizontal wind speed is determined from the attitude and position of the UAS (Wetz and Wildmann 2022). The algorithm is explained in more detail in the appendix in section A.

An additional algorithm based on motor thrust and acceleration was developed to determine changes in vertical wind speed relative to a mean vertical wind speed (Wildmann and Wetz 2022). This algorithm is suited to compute vertical velocity variance during hover periods. If the mean vertical wind speed is zero, the algorithm yields absolute vertical wind speed. However, if the vertical wind speed cannot be assumed to be zero such as in the ABL, the algorithm output may only be interpreted in relative terms

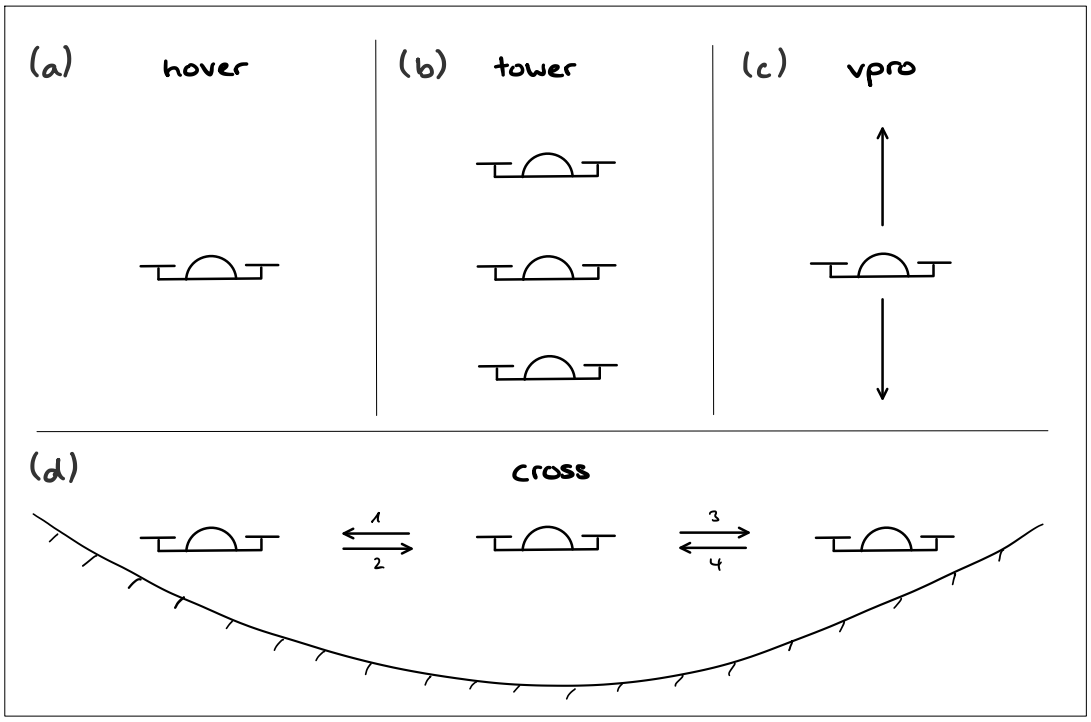

Figure 2.6: UAS flight patterns. The solid line with dashes below in panel (d) indicates a valley cross-section.

(e. g. "the upward movement increases over time"). When using the expression "wind speed" in this study, horizontal wind speed is meant. If vertical wind speed is meant, it is explicitly called "vertical".

The currently achieved accuracy is $\sigma_\psi < 5\,^\circ$ for wind direction, $\sigma_u < 0.25\,\mathrm{m\,s^{-1}}$ for horizontal wind speed, and $\sigma_w < 0.25\,\mathrm{m\,s^{-1}}$ for vertical wind speed relative to a mean vertical wind speed (Wetz and Wildmann 2022; Wildmann and Wetz 2022).

2.3.2 UAS – flight patterns and locations

Several flight patterns were applied during the campaign in 2022. The different patterns are illustrated in Fig. 2.6 and they are explained in the next paragraphs.

Patterns *hover*, *vpro*, *tower* In the *hover* pattern (cf. Fig. 2.6a), a UAS hovers for a pre-defined period of time, performing a fixed-point measurement. The default hovering time used in this study was 10 min, and the default hovering height 120 m AGL. Shorter hovering periods at different heights occurred only during manual flight or when hovering was incorporated into other flight patterns (such as in the pattern *cross* as explained in the next paragraph).

In the *vpro* pattern (cf. Fig. 2.6c), which stands for "vertical profile", a UAS flies upward and downward between two distinct heights once or multiple times. We used data from ascents only as, during descent, the drone flies through its own downwash

which disturbs the measurement. The ascent rate was set to $1\,\mathrm{m\,s^{-1}}$, the descent rate was $3\,\mathrm{m\,s^{-1}}$, and the default amount of ascents per flight was two. The default heights between which the drone alternated were 7 and 120 m AGL. Consequently, two consecutive ascents were approximately 3 min apart.

Multiple UAS with the same or different patterns can be combined. For example, multiple hovering UAS can be stacked vertically to imitate a measurement tower (cf. Fig. 2.6b). At Nafingalm, this *tower* pattern was tested with three UAS hovering at 20, 70, and 120 m AGL, respectively. The heights were chosen such that the whole height range which is allowed for UAS (up to 120 m AGL) is sampled. Other combined patterns are explained later.

Pattern *cross* A flight pattern tested with the SWUF-3D drones for the first time was the *cross* pattern. In this pattern, a UAS flies across the valley to perform a scan of a horizontal transect. At Nafingalm, the transects were west-east oriented, i. e. parallel to a latitude, to fly perpendicular to the almost north-south-oriented valley axis (cf. red lines in the close-up in Fig. 2.2).

Until mid-2022, measurements with the SWUF-3D fleet had only been done in *hover* mode, so correcting the wind measurement using the horizontal ground speed measured by GNSS had not yet been necessary. Hence, before TEAMx-PC22, it was not clear if that correction yielded proper results during forward flight. In order to include measurement periods for which the algorithm was already known to work, we included three *hover* periods per horizontal leg in the *cross* pattern: at the westernmost point close to the slope, at the approximate valley center, and at the easternmost point close to the slope (red dots in Fig. 2.2 and Fig. 2.7). The time span for the hover periods was 30 s.

The order of the legs during a flight is indicated by the numbers in Fig. 2.6. *Cross* flights started at the valley center. From there, the UAS moved to the hover point at the western slope, back to the hover point at the valley center, to the hover point at the eastern slope, and again back to the hover point at the valley center (four legs). Usually, the sequence of those four legs was repeated once (eight legs in total, taking approximately 12 min when performed at the southern lake shore at 10 m above valley floor level). For locations at which the *cross* flight distance was too long to repeat the whole four-leg pattern due to limitations of battery capacity (such as for the *cross* flights at the southern lake shore at 40 m above the valley floor), only legs 1 and 2 (cf. arrows indexed with 1 and 2 in Fig. 2.6d) were repeated after the four-leg pattern (six legs in total, taking approximately 13.5 min when performed at the southern lake shore at 40 m above valley floor level).

For the measurements during forward flight, a horizontal velocity of the UAS had to be defined. The measured wind speed was expected to be on the order of a few $\mathrm{m\,s^{-1}}$ only. A high forward speed of the drone as compared to the low measured wind speeds

was expected to decrease the accuracy of the wind measurement. On the other hand, the faster a UAS moves forward, the longer the distance that can be scanned in a given period of time. In the end, a horizontal velocity of $1\,\mathrm{m\,s^{-1}}$ was chosen as a compromise.

The resulting time needed to cross the valley once (leg from one valley side wall to the central hover point + hover period + leg from central hover point to other valley side wall + hover period) depends on the location where the *cross* pattern is performed since the transect from one valley side wall to the other depends on the latitude and the height above valley floor level (AVFL). The *cross* pattern was performed at two locations: at the creek delta on 22 June 2022 (flights no. 202 to 207 in table C.1; for location cf. southern red line in Fig. 2.2), and at the southern lake shore on 22 June 2022 (flights no. 208 and 209) and 23 June 2022 (flights no. 301 to 312 and 322 to 326; for location cf. northern red line in Fig. 2.2). Furthermore, the *cross* flights were performed at different height levels, 10 m and 40 m AVFL. The time needed to cross the valley at the southern lake shore (at the delta) at 10 m height was approximately 3 min (2 min), at 40 m height it was approximately 4.5 min (3.5 min) if the flight was not disturbed by manual input via the remote control.

As suggested in (Serafin et al. 2020), stacked horizontal flights can be used to get a better data coverage of an area. This was achieved by operating two vertically stacked UAS at 10 m and 40 m AVFL. Since the transect of the higher UAS is longer than that of the lower UAS, the western- and easternmost hover point of the higher and the lower UAS are not at the same horizontal position. This is indicated in Fig. 2.2 by the five red dots per red line. From west to east, these dots indicate: westernmost hover point of the higher UAS, westernmost hover point of the lower UAS, central hover point for both UAS, easternmost hover point of the lower UAS, easternmost hover point of the higher UAS. A side view of such stacked *cross* flights is illustrated in Fig. 2.7b.

Actual stacked *cross* flights require synchronization of the horizontal position of the upper and lower UAS. This was tested by simulating the upper and the lower UAS and increasing hover times at the western- and easternmost hover points of the lower UAS, deviating from the default hover time of 30 s. The simulations were done for the southern *cross* flight trajectory at the creek delta whose flight plans were created in advance of the measurement campaign (cf. southern red line in Fig. 2.2). Flight plans for the northern *cross* flight trajectory (cf. northern red line in Fig. 2.2) were created during the measurement campaign, hence, simulations to synchronize the two UAS were not performed.

The westernmost and easternmost hover points were chosen such that the drone was as close to the slope as possible to potentially capture slope winds, while still keeping a safe distance from the ground. The safety margin was chosen rather high since these were the first measurements of the SWUF-3D fleet in complex terrain. Drones starting their *cross* flight at 10 m AVFL had a 5 m vertical distance to the slope. Drones starting their

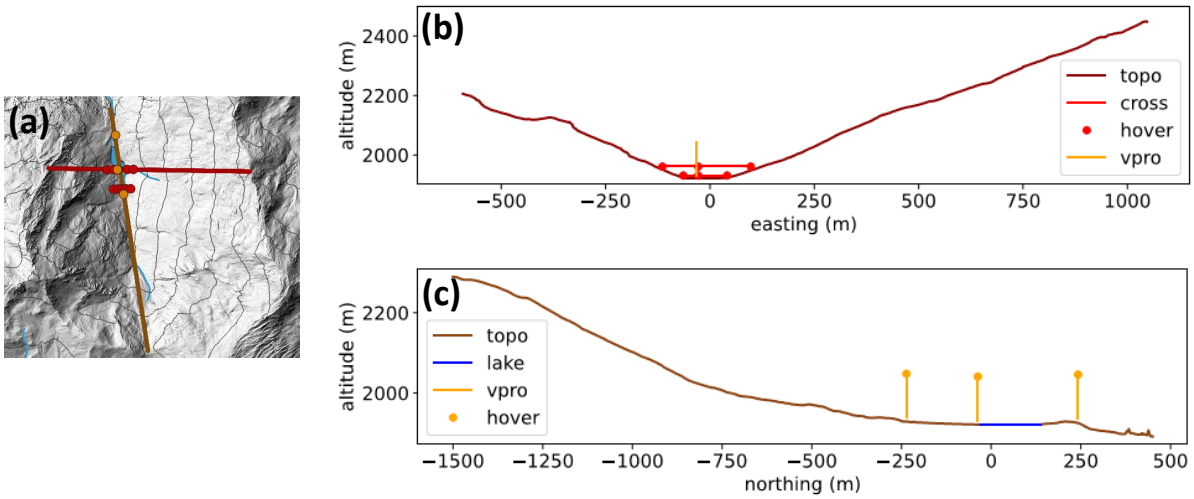

Figure 2.7: (a) Simplified map of Nafingalm, (b) schematic of *cross+vpro* pattern, (c) schematic of *vpro+hover* pattern. Dark-red cross-valley transect in (a) corresponds to dark-red topography in (b). Brown along-valley transect in (a) corresponds to brown topography in (c). Blue line in (c) indicates position of lake. Red dots in (a) and red dots and lines in (b) indicate hover positions and flight trajectories of UAS during *cross* flights. Orange dots in (a) indicate locations of vertical profiles of UAS, located close to the brown valley axis. Orange lines in (c) indicate flight trajectories during vertical profiling, orange dots are hover position after the ascent.

cross flight at 40 m AVFL had a 10 m vertical distance to the slope. The larger vertical distance for the higher UAS at 40 m AVFL was chosen due to the more difficult visual surveillance. The drones were operated in auto-pilot mode but nevertheless needed to be surveyed visually in order for pilots to control them manually in case of unforeseen events such as GNSS failure. The higher UAS could be visually tracked less easily when approaching the terrain than the lower UAS at 10 m AVFL being closer to the observer.

Pattern combinations All of the patterns described above can be combined, provided that the flight plans are designed such that collision of the UAS is precluded. Besides the *vpro* pattern, combinations used were *cross+vpro* and *vpro+hover*. These patterns are illustrated in Fig. 2.7 to get an idea of the ratio of the sampled valley volume to the total size of the valley.

The pattern *cross+vpro* combines two stacked UAS performing *cross* flights with one UAS performing a vertical profile. The vertical profile was done close to the central hover point of the *cross* pattern near the HOBO station at the southern lake shore. In Fig. 2.7b, the pattern *cross+vpro* is illustrated as seen from the side, facing the north. The two red lines indicate the *cross* flight trajectories at 10 and 40 m above the central valley floor. The red dots are the hover points. The orange vertical line indicates the vertical profile and corresponds also to the middle vertical orange line in Fig. 2.7.

In this combined pattern, the "*vpro* drone" performed four ascents during one flight. The number of ascents was chosen such that the "*vpro* drone" had the approximate same flight time as the "*cross* drones". The heights between which the "*vpro* drone" alternated were 7 and 120 m AGL to capture as much of the boundary layer as possible whilst keeping a safe distance to the HOBO station with a maximum height of 2 m AGL and complying to current law (max. 120 m AGL, as mentioned earlier).

The combination *vpro+hover* was performed with three drones simultaneously. They ascended to 120 m AGL, hovered at maximum height for 10 min each, then descended and landed. The UAS sampled simultaneously at three locations along the valley axis, indicated by the three vertical orange lines with dots on top in Fig. 2.7c, corresponding to the three orange dots in Fig. 2.7a: close to the AWRS station north of the lake, close to the HOBO station on the southern lake shore, and at the creek delta. Note that the valley axis is not exactly north-south oriented. Hence, northing on the x-axis in Fig. 2.7c does not exactly correspond to the same distance along the brown transect in Fig. 2.7a. Instead, there is a slight deviation of 1 m northing corresponding to 1.015 m horizontal distance along the brown transect.

2.3.3 Automatic pattern detection in UAS flight data

The raw data of a UAS flight are output as a continuous time series including launch, flight to the first waypoint, execution of the pre-defined pattern, flight back to the launch position, and landing. In order to analyze the measurements taken during pattern execution or only during part of a pattern, the time series has to be cut. The pattern detection within a flight was designed to be automated as much as possible.

The most relevant conditions to detect *vpro* periods were an upper threshold for horizontal velocity $u, v < 0.2\,\mathrm{m\,s^{-1}}$ and a lower threshold of vertical velocity $w > 0.15\,\mathrm{m\,s^{-1}}$. The most relevant condition to detect *hover* periods was an upper threshold for both horizontal and vertical velocity being $u, v, w < 0.5\,\mathrm{m\,s^{-1}}$. Periods of the *cross* pattern were indirectly detected: first, all hover periods within a *cross* flight were detected. Then, the periods in between these hover periods had to be the *cross* flight legs. A seemingly easier way to determine the *cross* flight legs is to select the part of the flight corresponding to a certain flight time. However, this procedure is not robust against manual steering of the drone during flight, either on purpose or accidentally by moving the control levers while the drone is in auto-pilot mode.

Mistakenly detected patterns were partially eliminated automatically. For example, detected patterns of only a few seconds in time and patterns contained entirely within the time period of another larger pattern were discarded. Overlapping patterns were separated in order for the one pattern (e. g. *vpro*) to end before the other pattern (e. g. *hover*) begins.

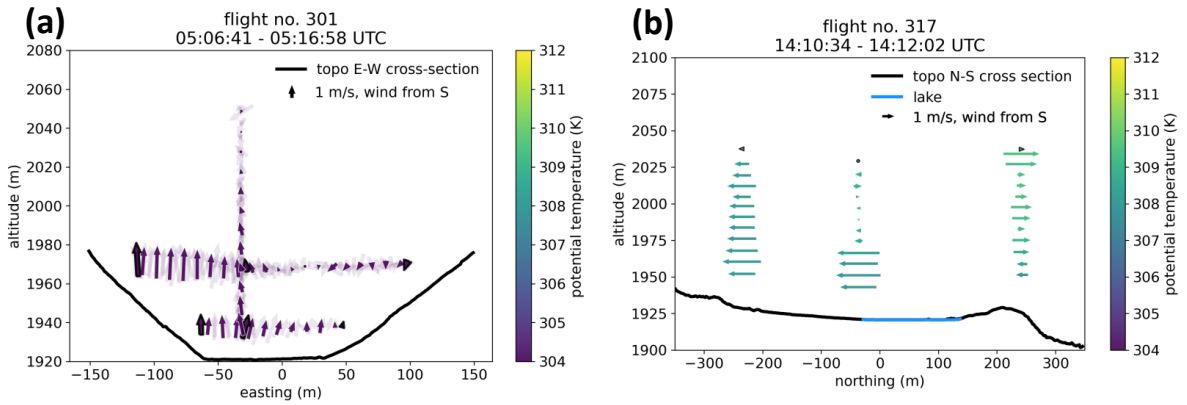

Figure 2.8: Example of the representation of (a) a *cross+vpro* flight and (b) a *vpro+hover* flight. The explanation is given in section 2.3.4.

At the beginning and end of a pattern, the drone usually accelerates or decelerates which is visible in erroneous peaks of horizontal wind speed. The start and end times of the pattern were adjusted such that the start/end value of horizontal wind speed is not higher than 1.25 times the average value of the next/previous ten time steps. Despite the automatic detection, some patterns still had to be manually corrected or discarded in a final step.

2.3.4 Graphical processing of UAS flights

To evaluate UAS flights of the combined patterns *cross+vpro* and *vpro+hover*, special representations were used. Exemplary illustrations are explained in this section.

***Cross+vpro* flights** For the *cross+vpro* flights, a representation was sought which combines information about wind speed, wind direction, and a scalar meteorological parameter, and which also combines simultaneous legs of *cross* flights and vertical profiles. However, horizontal and vertical legs were usually not exactly simultaneous due to the different required time periods for a horizontal and a vertical flight leg. Hence, all legs of all simultaneous flights were combined in one panel. Averages of wind speed, wind direction, and a scalar quantity (potential temperature or water vapor mixing ratio) were computed for each 10 m-bin of a flight trajectory. For each bin, one arrow (or "quiver") was generated, providing information about wind speed, direction, and the chosen scalar quantity. The advantage of illustrating the data this way is that three meteorological parameters can be displayed all at once. The disadvantage of this representation, however, is that signals with a scale smaller than bin size are lost.

An example of such a plot can be found in Fig. 2.8a. The plot resembles the schematic of a *cross+vpro* flight in Fig. 2.7b, with the view along the valley axis towards the north, but zooming into the central part of the valley where the UAS were located. The plot shows the *cross* flight at 10 m AVFL, the *cross* flight at 40 m AVFL, and the *vpro* flight

between 7 and 120 m AGL. The black line represents a lateral topographic cross-section through the valley. The arrow direction indicates wind direction, however, an important point must be made in order to avoid misunderstandings: the orientation of the arrows indicates the orientation of the wind direction in a *horizontal* plane, hence, an arrow pointing vertically up in the plot means a horizontal wind from the south, *not* vertical wind. The length of the arrow indicates the wind speed in $\mathrm{m\,s^{-1}}$. The color of the arrows indicates the value of potential temperature or of water vapor mixing ratio. Faint arrows are measurements of single flight legs. Color-saturated arrows represent the averages of all flight legs within a flight. Measurements at hover positions are marked with a black edge.

***Vpro+hover* flights** For the combined pattern *vpro+hover*, simultaneous flights were combined in one panel, similar to the graphical representation of *cross+vpro* flights. An example of such a plot is given in Fig. 2.8b. The plot resembles the schematic of a *vpro+hover* flight in Fig. 2.7c, viewing the valley from the side looking from the east towards the west, zooming into the central part of the valley where the UAS are located. To the left of the plot is the south, and to the right is the north. The black line is the topography along the valley axis, and the blue line indicates the location of Nafing Lake. The leftmost vertical profile is the one at the creek delta, the central vertical profile is at the southern lake shore, and the rightmost profile is north of the lake.

The difference between *vpro+hover* plots and *cross+vpro* plots is the orientation of the topography and the meaning of arrow direction: on the x-axis of Fig. 2.8b, northing is plotted instead of easting. A southerly wind is represented by an arrow pointing from left to right, as opposed to southerly winds in Fig. 2.8a. The arrows *only* show the *north-south-vector component* of horizontal wind, *not* the whole wind vector. Consequently, the displayed wind speed can deviate from the total horizontal wind speed. The data displayed in quiver plots for both *cross+vpro* and *vpro+hover* flights were smoothed with a moving average of 0.5 s.

2.4 Model data

ERA5 reanalysis data were used in this study to put the measurements at Nafingalm between 20 and 28 June 2022 into the context of the synoptic weather situation. COSMO-1E forecast data were used to obtain the near-ground wind field in the Nafingalm area for the case study on 23 June 2022.

ERA5 reanalysis data ERA5 is the acronym of the fifth generation of the ECMWF (European Center for Medium-Ranger Weather Forecast) reanalysis for the global climate and weather within the last eight decades (Hersbach et al. 2023). In an analysis, model

data of a recent forecast are combined with newly available observational data. The method to combine this information is called data assimilation. The goal is to get a best estimate of the atmospheric state that is spatially and temporally consistent. In a reanalysis, the same is done but for a past point in time. The horizontal grid size of ERA5 is 0.25° which corresponds to approximately 28 km in north-south direction and 19 km in west-east direction for central Europe (at 47° N). The temporal resolution is one hour.

For this study, data for Europe (longitude -15°W to 20°E, latitude 30°N to 70°N) on 23 June 2022 were regarded. The dataset used comprises geopotential height, absolute temperature, and relative humidity at 800 hPa.

COSMO-1E forecast data COSMO-1E is an ensemble prediction system with 11 ensemble members based on the COSMO model developed by the Consortium for Small-scale Modeling (2023). COSMO-1E is used operationally by the Swiss Federal Office of Meteorology and Climatology (MeteoSwiss 2023) to create weather forecast products on regional and local scales for the Alpine area. COSMO-1E contains 11 ensemble members and the horizontal grid size is 1.1 km (hence the name COSMO-*1E*). Boundary values are taken from the IFS HRES model by ECMWF. The model is run every three hours (00, 03, ..., 21 UTC). The forecast lead time of the 03 UTC control run which was used in this study for 23 June 2022 is 45 hours. The data were provided by MeteoSwiss.

Chapter 3

Results

In this chapter, the ground-based observations of the measurement campaign between 20 and 28 June 2022 are described and put into the context of the synoptic weather situation. Then, the 23 June 2022 is analyzed in detail with respect to the atmospheric regimes occurring in different phases of the day.

3.1 Measurements between 20 and 28 June 2022

The synoptic weather situation between 20 and 28 June 2022 is shown in Fig. 3.1. The period started with a stationary front associated with an air mass boundary in west-east direction over Europe (cf. Fig. 3.1a). After a small upper-level ridge passed central Europe on 21 June (signature only weakly visible in the geopotential of the 800 hPa chart in Fig. 3.1b), a low-level south-westerly flow towards the Alps established on 22 June (cf. Fig. 3.1c). In the morning of 23 June, a ridge prevailed over central Europe (not displayed in Fig. 3.1), moving westward and leading to intensification of the southwesterly flow towards the Alps. This flow, in combination with a hydrostatic pressure gradient caused by a northward temperature gradient across the Alps, led to south foehn in the central Alps in the course of the day. A corresponding "foehn nose" indicating lower geopotential (which is coupled with pressure) north of the Alps can be seen in Fig. 3.1d. On 24 June, a cold front passed the Alps from the southwest (cf. kink in isohypses north of Nafingalm in Fig. 3.1e). From here, the sequence of ridge, pre-frontal foehn and a cold front repeated:: a small ridge passed the Alps (weakly indicated by the geopotential in Fig. 3.1f), pre-frontal south foehn established (cf. Fig. 3.1g) and lasted until the evening of 27 June (cf. Fig. 3.1h), and a cold front reached the central Alps in the evening, this time from the northwest. The Alps remained under the influence of this front on 28 June (cf. Fig. 3.1i).

An overview of the ground-based observations at Nafingalm between 20 and 28 June 2022 is presented in Fig. 3.2. In Fig. 3.2a, both AWRS and sonic anemometer data are displayed because they complement each other in the case of data gaps.

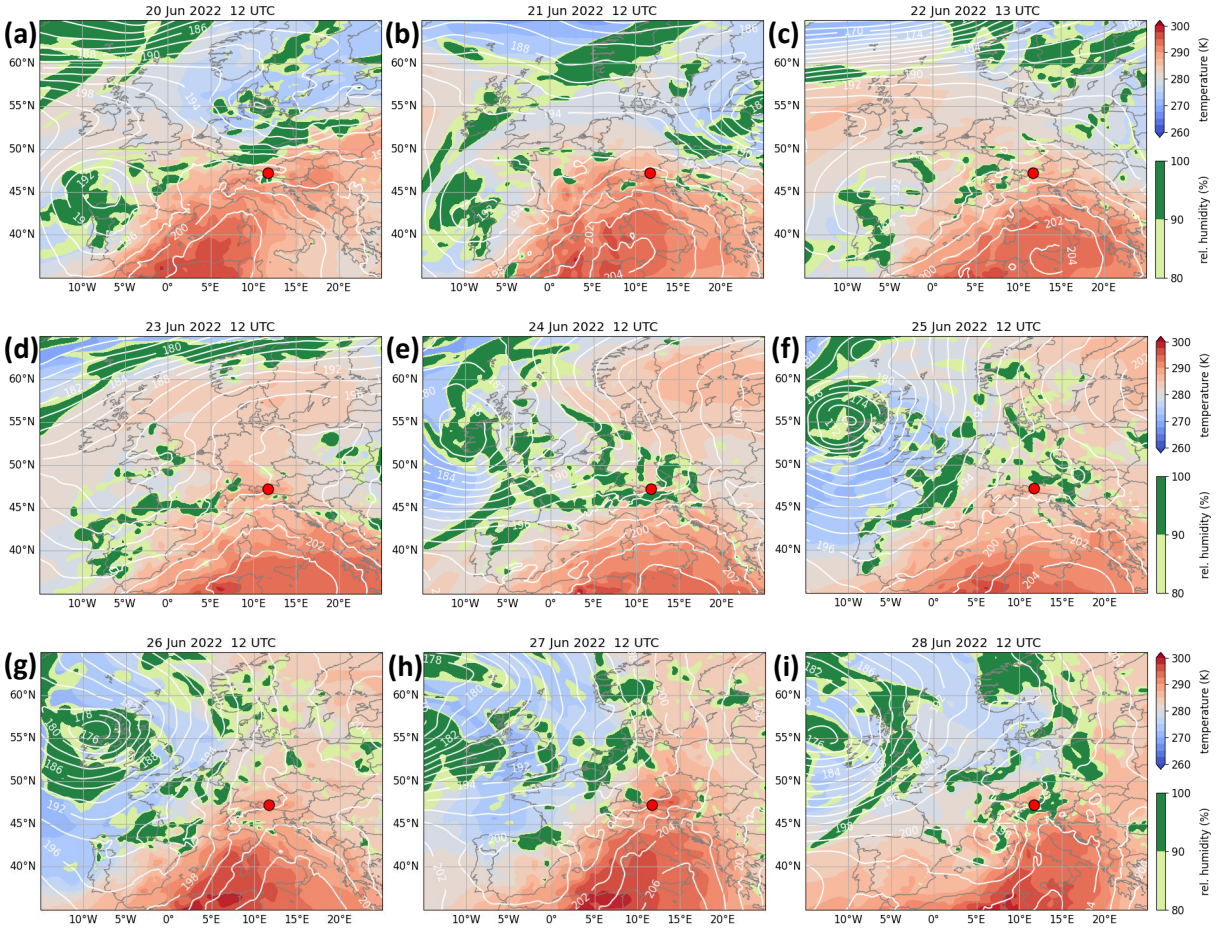

Figure 3.1: ERA5 data at 800 hPa for Europe for the time period of 20 to 28 June 2022. One plot per day showing data for 12 UTC: (a) 20 June, (b) 21 June, (c) 22 June, (d) 23 June, (e) 24 June, (f) 25 June, (g) 26 June, (h) 27 June, (i) 28 June. Blue to red color contours indicate temperature. Green color contours indicate relative humidity above 80%. White lines indicate geopotential height in geopotential decameters with contour line spacing of 2 gpdm. Grey lines are national borders. Red dot indicates position of Nafingalm.

Wind speed and direction data of the AWRS were discarded if the values were below the respective threshold related to sensor inertia, even though the sensor-internal averaging over five minutes might mitigate the effect of introducing errors. The sonic anemometer experienced multiple power outages between 25 and 27 June.

20 to 22 June 2022: The stationary front over Europe on 20 June caused cloudy and rainy weather at Nafingalm. The first UAS flights with *vpro* patterns were tested in the evening after a few rain showers. (cf. Fig. 3.2c for rain and Fig. 3.2e for UAS flights).

The synoptic-scale ridge caused fair weather on 21 June at Nafingalm with incoming short-wave radiation resembling the ideal curve more than on the previous day (cf. purple dashed line in Fig. 3.2d). The dips in the curve were caused by convective clouds. Convective, turbulent conditions were also detected by UAS measurements when horizontal

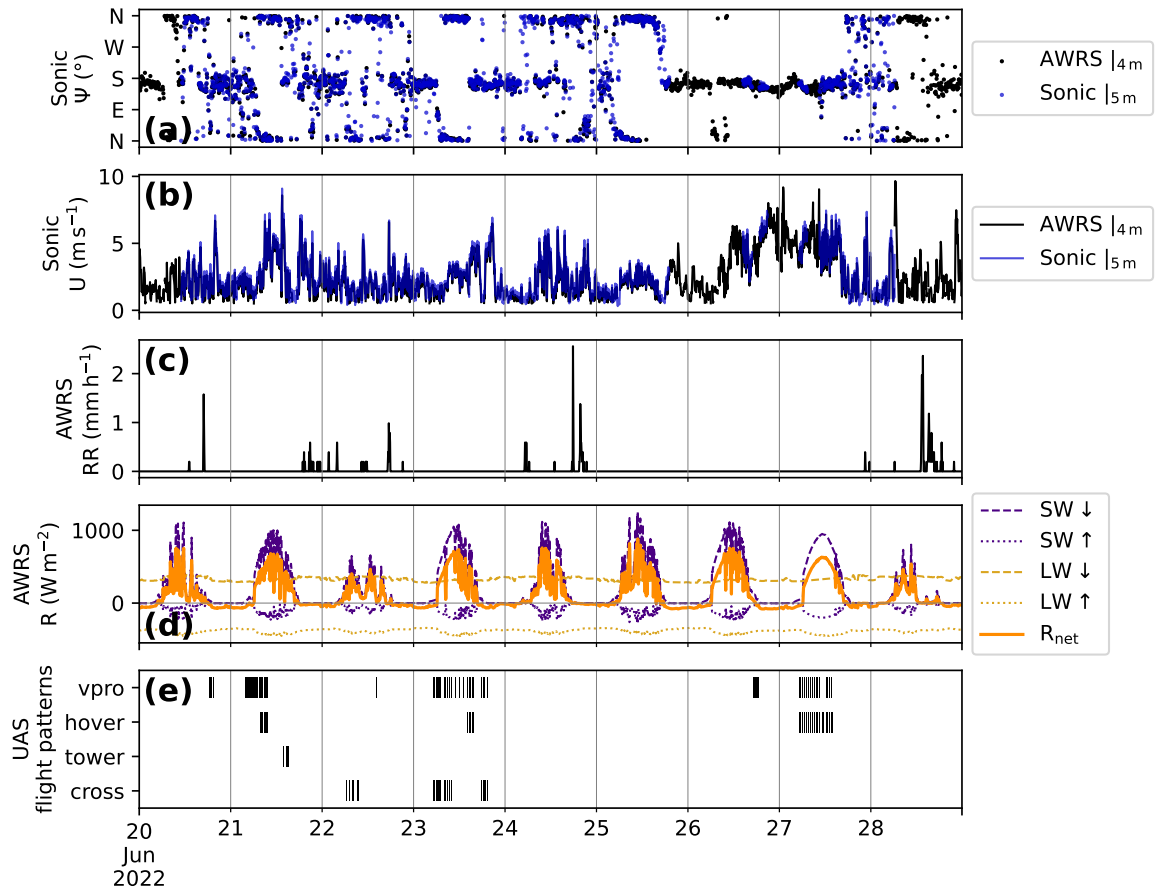

Figure 3.2: Overview of meteorological quantities measured during the campaign from 20 to 28 June 2022. All quantities in panels (a)–(d) are 5-minute averages. Time on x-axis in UTC. (a) Wind direction Ψ measured by the sonic anemometer (blue) and the AWRS (black). (b) Horizontal wind speed U, same measurement instruments as in (a). (c) Rain rate RR measured at the AWRS. (d) Radiation R with the single components incoming short-wave radation $R_{\mathrm{SW}\downarrow}$, outgoing short-wave radiation $R_{\mathrm{SW}\uparrow}$, incoming long-wave radiation $R_{\mathrm{LW}\downarrow}$, outgoing long-wave radiation $R_{\mathrm{LW}\uparrow}$, and net radiation R_{net}, measured by the AWRS. (e) UAS flight patterns *vpro*, *hover*, *tower*, *cross*. Combined patterns *vpro+hover* and *cross+vpro* are illustrated by bars at *vpro* and *hover*, and at *cross* and *vpro* for the same time period.

wind speeds varied by multiple $\mathrm{m\,s^{-1}}$ within seconds while hovering at 120 m AGL. The curves in Fig. 3.3a-b illustrate these variations. At 0730 UTC, variations are mostly within $5\,\mathrm{m\,s^{-1}}$ (cf. Fig. 3.3a). Approximately one hour later, between 0850 and 0852 UTC; there are more pronounced changes in horizontal wind speed of up to $5\,\mathrm{m\,s^{-1}}$ within seconds (cf. Fig. 3.3b). The first UAS flights of the day were already performed before the onset of convective mixing in the boundary layer in order to potentially capture the morning transition from nighttime katabatic flow to daytime anabatic flow. Later in the day, the convective conditions led to thunderstorms. After a local shower, the *vpro* pattern was tested. Then, UAS operations were stopped for that day due to impending precipitation.

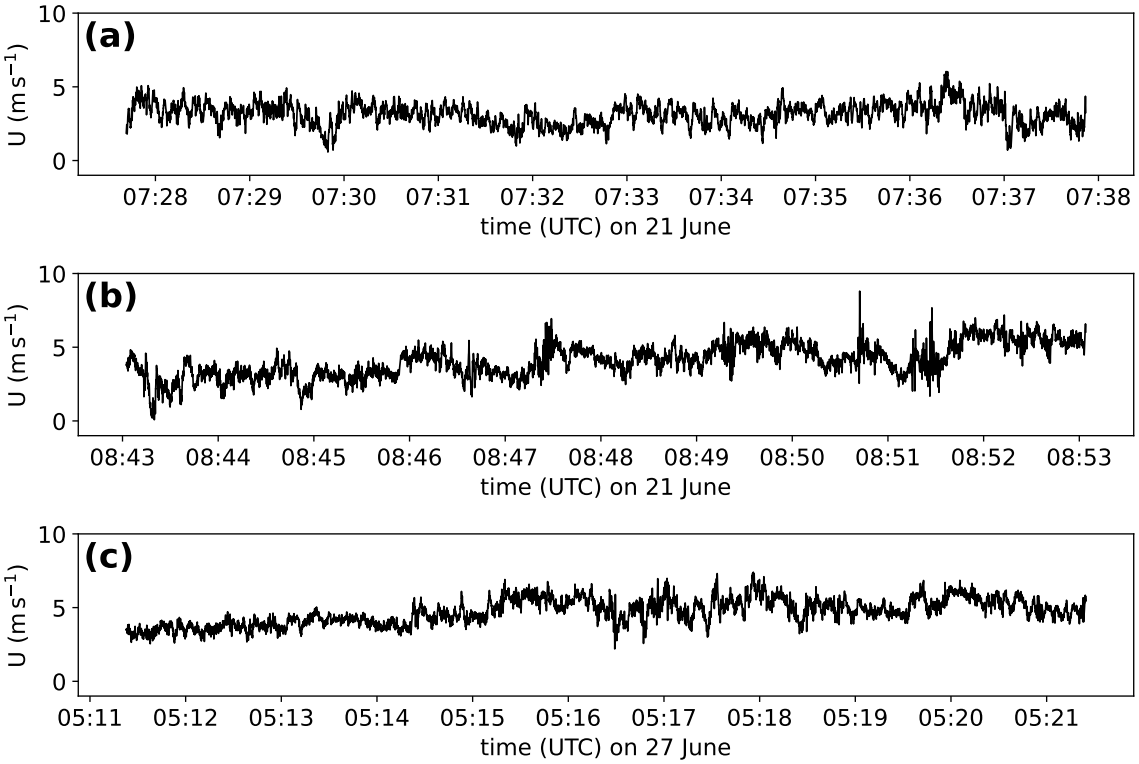

Figure 3.3: Horizontal wind speed U during hover periods of UAS at 120 m AGL for (a) flight no. 121 on 21 June 2022 at the southern lake shore, (b) flight no. 125 on 21 June 2022 at the creek delta, and (c) flight no. 701 on 27 June 2022 north of the lake. The x-axis shows UTC time for both panels. The sampling frequency of the data is 20 Hz.

On 22 June, periods of rain only permitted UAS flights during the forenoon and shortly in the afternoon. For the first time, *cross* flights were performed and tested at the creek delta. As the flight plans passed the test, the *cross* pattern was also tested at the southern lake shore, flying by the HOBO station.

23 June 2022: Under the influence of the synoptic-scale ridge over central Europe, wind speeds at Nafingalm were rather low in the morning of 23 June, compared to other morning-time wind speeds (cf. Fig. 3.2b). In the course of the day, cumulus clouds evolved.

South foehn became dominant in the central Alps around noon: In the Wipp Valley, a deep valley west of Nafingalm with a maximum height of approximately 1400 m AMSL at the Brenner pass, foehn set in around 1230 UTC in Steinach and around 1430 UTC at Ellbögen (both at approximately 1000 m AMSL, for precise location see Fig. 2.1) but did not reach down to Innsbruck (at approximately 600 m AMSL), following the foehn classification and method by Plavcan et al. (2014). Corresponding figures are to be found in appendix D.

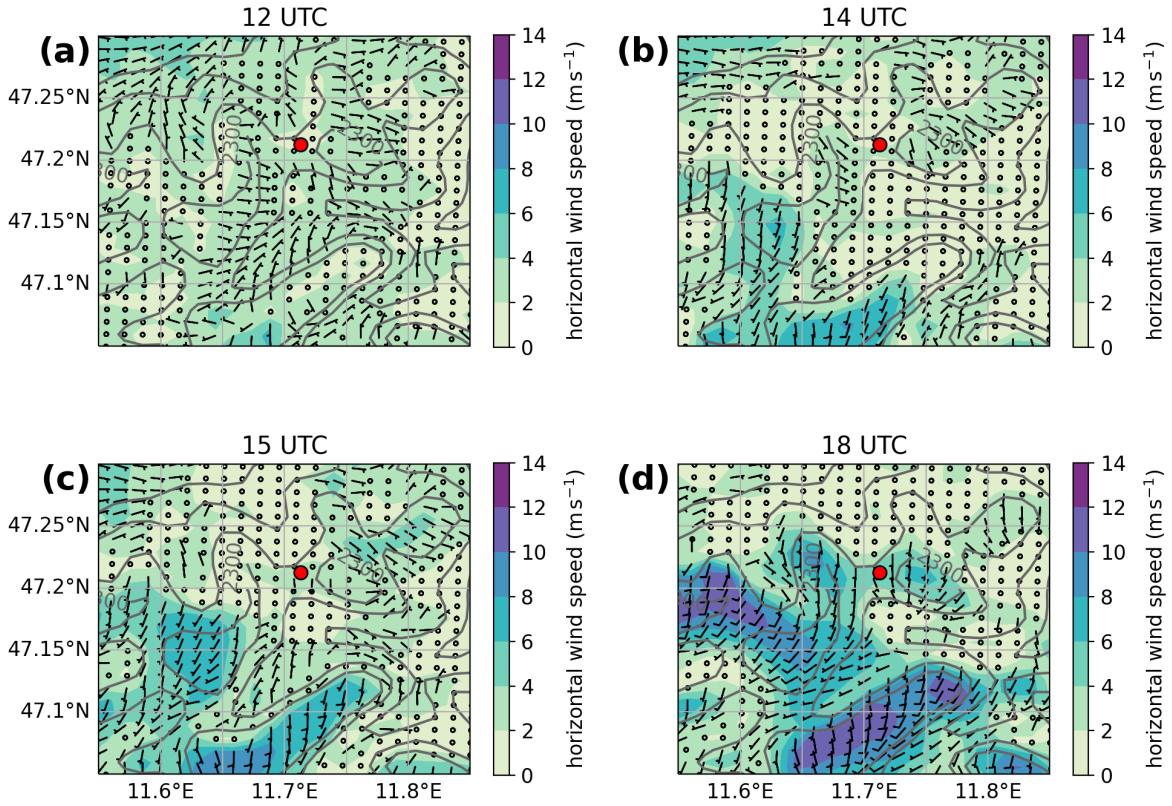

Figure 3.4: COSMO-1E forecast data at 10 m AGL for 23 June 2022 at different times of the day. All panels show the same domain located in the Tux Alps, with the Inn Valley north and the Ziller Valley east of the domain (see map in Fig. 2.1). The red dot indicates the location of Nafingalm. The forecast run was initialized at 03 UTC and the forecast lead times are +9, +11, +12, and +15 hours, corresponding to (a) 12 UTC, (b) 14 UTC, (c) 15 UTC, (d) 18 UTC. Color contours: horizontal wind speed in $\mathrm{m\,s^{-1}}$. Wind barbs: horizontal wind direction. Grey lines: surface elevation contours at 1000, 1500, 2000, 2300 m AMSL.

For the region around Nafingalm, the COSMO-1E model predicted 10 m-winds to be on the order of 1 to 5 $\mathrm{m\,s^{-1}}$ only at 12 UTC (cf. Fig. 3.4a). The areas with higher wind speeds which mostly correspond to areas of higher elevation mainly show easterly wind directions at that time. At 14 UTC, a field of southerly winds with wind speeds on the order of 7 to 8 $\mathrm{m\,s^{-1}}$ was predicted to move towards Nafingalm from the south. At that point in time, the COSMO model still predicted wind speeds below 2 $\mathrm{m\,s^{-1}}$ for Nafingalm (cf. Fig. 3.4b). However, at 15 UTC, wind barbs close to Nafingalm indicate southerly airflow for the first time after the morning transition period (cf. Fig. 3.4c). In the course of the afternoon, wind speeds were predicted to intensify at Nafingalm, reaching up to 5 $\mathrm{m\,s^{-1}}$ at 18 UTC (cf. Fig. 3.4d). The observations at the AWRS confirm that southerly winds set in at the Nafingalm valley floor in the afternoon.

Figure 3.5: UAS take-off position at the creek delta. View is towards north. The yellow textile wind vanes marked with red circles indicate southerly flow with a slightly westerly component for the vane on the left and an easterly component for the vane on the right. Photograph taken on 26 June 2022 by the author.

The goal for 23 June was to perform the pattern *cross+vpro* during a potentially observable morning and evening transition and to obtain at least one vertical profile every hour during daytime. Between 10 and 14 UTC, only one UAS was used for measurements due to only one pilot available. Between 16 and 1730 UTC, no UAS flights were performed.

24 to 28 June 2022: On 24 and 25 June, no UAS flights were performed because crew members were not available. On 26 June, foehn set in during the forenoon between 06 and 10 UTC at Steinach and Ellbögen (figures not shown). At Nafingalm, nighttime katabatic winds prevailed until a phase of northerly upvalley winds set in in the forenoon. Then, southerly winds with speeds of more than $5\,\mathrm{m\,s^{-1}}$ set in, marking the onset of foehn at the Nafingalm valley ground (cf. Fig. 3.2a-b).

In the evening, multiple simultaneous *vpro* flights with two UAS were performed. One UAS profiled the atmosphere north of the lake next to the AWRS. The other UAS was operated at the creek delta at the southernmost location of Nafingalm valley floor. The southerly winds close to the ground prevailed both north of the lake and at the delta further south, as indicated not only by UAS (not shown) but also by textile wind vanes put up during UAS measurements (cf. Fig. 3.5).

On 27 June, foehn kept influencing Nafingalm as the high-speed southerly winds continued and the sky was clear (cf. Fig. 3.2a-b, d). UAS flights were again performed north of the lake and at the delta in the south, but the pattern was changed to *vpro+hover*. In flight, the drones showed turbulent conditions with changes of horizontal wind speed by multiple $\mathrm{m\,s^{-1}}$ within seconds (cf. Fig 3.3c) and the main wind direction was south. The foehn period was ended by the approaching cold front in the evening with wind directions deviating from south, decreased wind speeds, and temporally with rain (cf. Fig. 3.2a-c).

After the rainfall during the evening and nighttime cooling, fog prevailed in the morning of the 28 June. No further UAS flights were performed on that day.

3.2 Measurements on 23 June 2022

The detailed analysis of atmospheric phenomena at Nafingalm focuses on 23 June as this day was covered by UAS flights from before sunrise (at the valley floor) to after sunset. The data of both ground-based and airborne instrumentation are evaluated.

Figure 3.6 is an excerpt of Fig. 3.2 for 23 June 2022 with additional parameters. This overview plot includes air temperature at the AWRS at two levels and the potential temperature gradient between these two levels (cf. Fig. 3.6d). It also contains temperature and humidity data of the HOBO sensors at 2 m AGL at the southern lake shore, on the slope and at the crest (cf. Fig. 3.6e and f). 23 June was subdivided into different phases based on the different regimes that occurred. Each phase is analyzed separately in this section.

3.2.1 Phase I – early morning

Phase I started at midnight and lasted until 06 UTC in the morning. The day began with thermally-driven katabatic winds from the south flowing downvalley, not only near the ground (cf. phase I in Fig. 3.6a), but also at altitudes up to 2020 m AMSL as indicated by UAS vertical profiles (cf. Fig. 3.7a). During the ascents between 0528 and 0535 UTC, a low-level jet was observed. The upper limit varied between 1970 and 1980 m AMSL which corresponds to approximately 50 m AGL (cf. Fig. 3.7b). The potential temperature indicates stable stratification throughout the layer of 120 m depth (cf. Fig. 3.7c). At 1970 m AMSL, there is a slight kink in the curve indicating a stabler layer below than above. This correlates with the occurrence of the low-level jet. Water vapor mixing ratio decreases with altitude as is typical for a nighttime ABL (cf. Fig. 3.7d).

Note that the data in plots of the type shown in Fig. 3.7 were smoothed with a moving average of 10 s (corresponding to 10 m for a UAS ascent rate of $1\,\mathrm{m\,s^{-1}}$) in the middle part of the ascent, reducing noise and making large-scale features better visible at the expense of losing small-scale features. Towards the lower and upper limit of the ascent, the moving average window was gradually made smaller, hence, the variability in the curves becomes larger at the lowest and highest altitudes. It should also be kept in mind that, the lower the wind speed, the less precise the wind direction measurement.

3.2.2 Phase II – morning

Between 06 and 0645 UTC, the morning transition from nighttime downvalley to daytime upvalley winds took place. The driving force for this transition is the sun. The HOBO

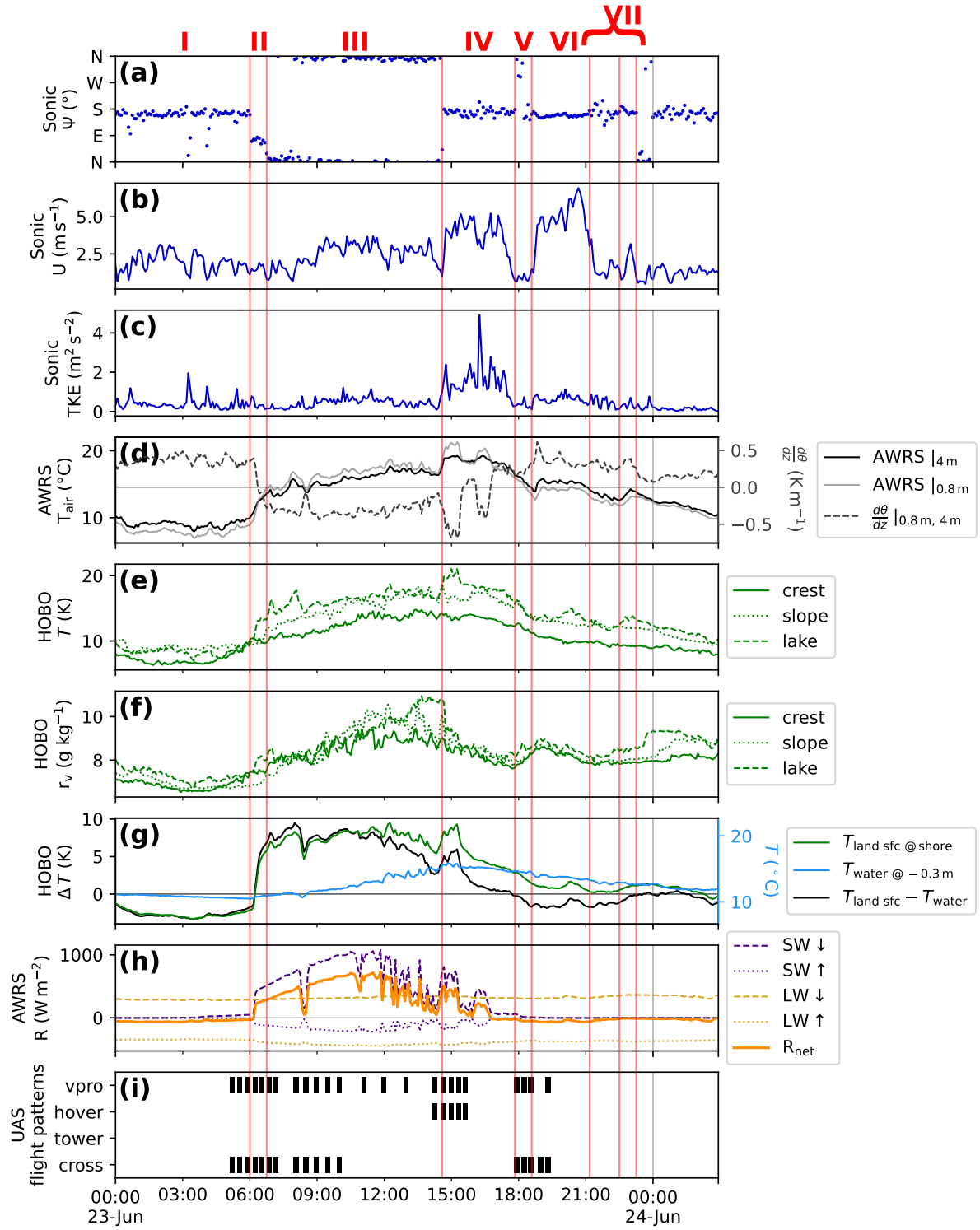

Figure 3.6: Overview of meteorological quantities measured on 23 June 2022. All quantities in panels (a)–(h) are 5-minute averages. Time on x-axis in UTC. The y-label of each panel indicates the displayed quantity and the corresponding measurement instrument. (a) Wind direction and (b) horizontal wind speed as in Fig. 3.2a-b. (c) Turbulent kinetic energy computed with 30-minute rolling averages. (d) Air temperature T and potential temperature gradient $\frac{d\theta}{dz}$ between 0.8 and 4 m at the AWRS. (e) Air temperature T at 2 m AGL at the HOBO stations at the southern lake shore, on the slope and at the crest. (f) Water vapor mixing ratio r_v at the same locations as (e). (g) Absolute temperature T of the land surface at the southern lake shore $T_{\text{land sfc @shore}}$ and of the water at 0.3 m below lake surface $T_{\text{water @}-0.3\,\text{m}}$ measured by HT sensors. Difference of the two temperatures ΔT in black. (h) Radiation and (i) UAS flight patterns as in Fig. 3.2d-e. The red lines and letters indicate the different phases of the day.

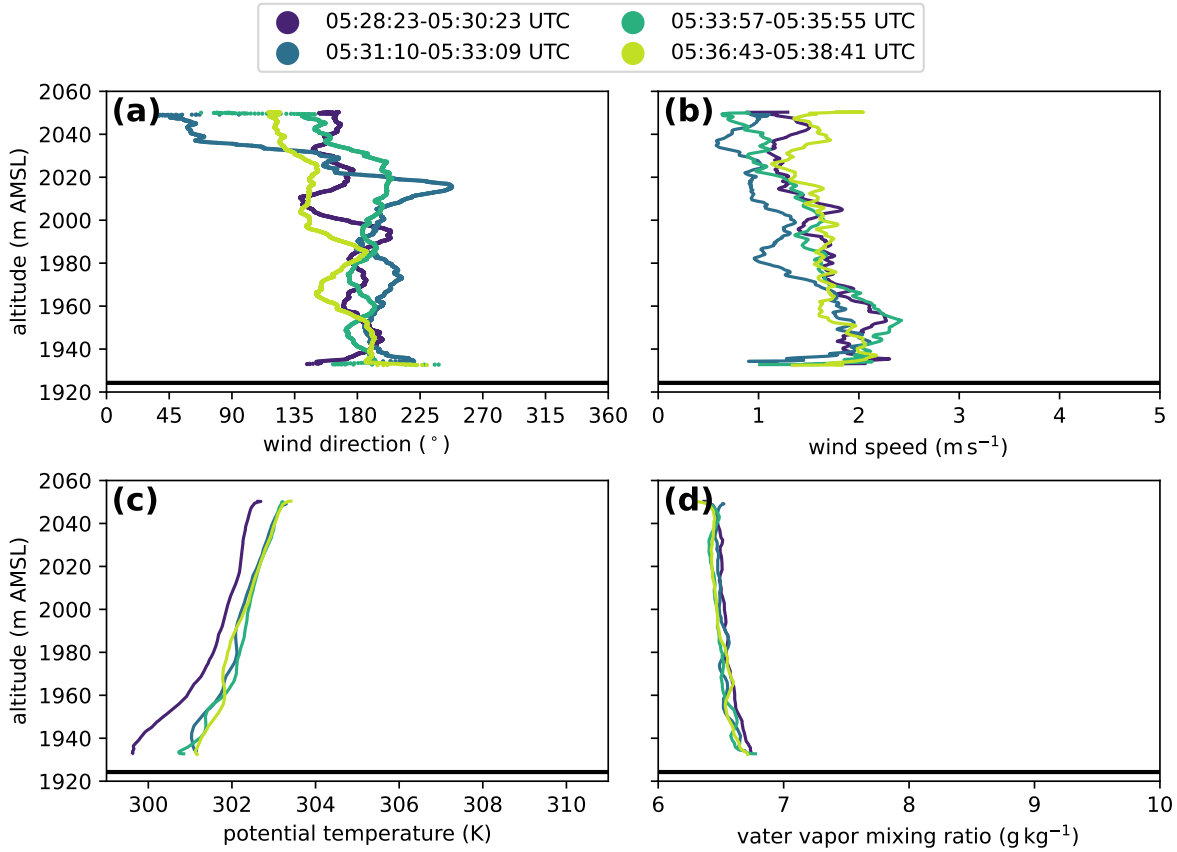

Figure 3.7: Figure belongs to phase I. Vertical profiles of flight no. 302 between 0528 and 0538 UTC on 23 June 2022. The measurement location is at the southern shore of Nafing Lake (cf. orange dot between lake and marshland in Fig. 2.2). The four lines in each panel are the different ascents during one flight (see legend for respective time periods). Four meteorological quantities are displayed: (a) wind direction, (b) wind speed, (c) potential temperature, and (d) water vapor mixing ratio. The black line is the ground elevation as derived from the barometric pressure sensor of the UAS. The data were smoothed with a moving average of 10 s, corresponding to 10 m at an ascent rate of 1 m s^{-1}. The moving average window gets smaller towards the upper and lower border of a vertical profile.

crest station was the first measurement station at Nafingalm to be exposed to the sun. There, air temperature started to increase at 05 UTC in the morning (cf. Fig. 3.6e). The east-facing slope was increasingly illuminated until it was entirely sunlit shortly after 06 UTC when solar radiation reached the AWRS and the HOBO lake station at the valley floor (cf. Fig. 3.8 and purple dashed line in Fig. 3.6h), leading to a steeper temperature increase (cf. black and grey curves in Fig. 3.6d, and green dashed curve in Fig. 3.6e). The temperature at the HOBO slope station located at the west-facing slope started to increase approximately 20 min later due to a longer phase of shading.

Potential temperature and water vapor mixing ratio increased throughout the valley atmosphere up to 120 m AGL (cf. Fig. 3.9c-d). The warming started from the ground.

Figure 3.8: Solar radiation reaches the valley floor at 0607 UTC on 23 June 2022 in phase II. Credits: Norman Wildmann, adapted photograph.

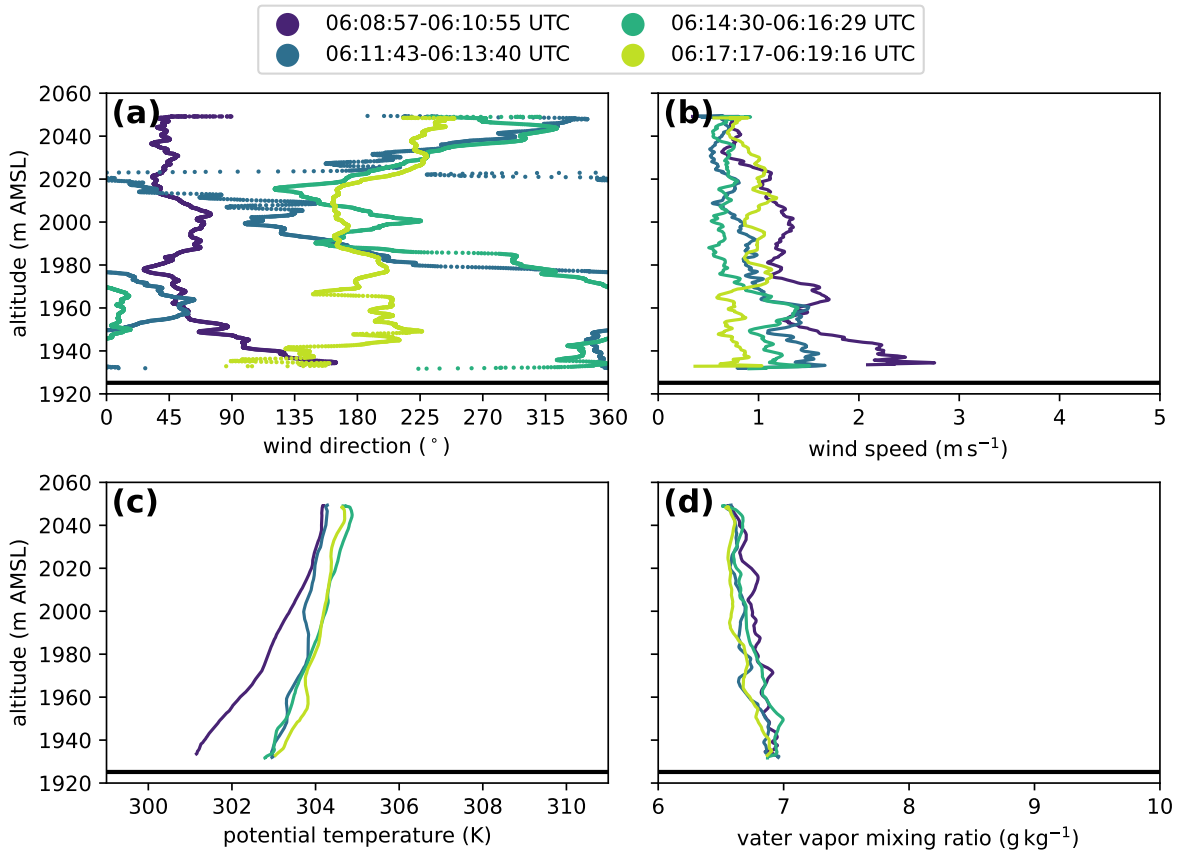

Figure 3.9: Figure belongs to phase II. Representation as in Fig. 3.7, at the same measurement location, on the same day, with the same moving average window, but for flight no. 304 between 0608 and 0619 UTC.

Consequently, stability decreased but the overall stratification was still stable at 0617 UTC (cf. ascent at 0611 UTC in Fig. 3.9c).

After 0610 UTC, wind speeds were lower than in phase I throughout the 120 m-layer, and the low-level jet observed in phase I had disappeared (cf. Fig. 3.9b). The low winds and the corresponding variable wind direction can also be seen in Fig. 3.10b. The vertical

line of arrows in that panel corresponds to the *vpro* flight also displayed in Fig. 3.9. The arrows are not recognizable as arrows as their lengths (wind speed values) are too small for proper representation.

The wind direction rotated counterclockwise from southerly downvalley via easterly to northerly upvalley winds due to the differential heating of the east-facing and the west-facing valley side walls. The change of the north-south-wind component from southerly to northerly happened until 07 UTC, but a tendency of an easterly wind component remained until 08 UTC at the ground (cf. Fig. 3.6a).

The counterclockwise rotation of the wind direction could also be observed at higher levels using UAS. There, the easterly wind component remained until shortly before 10 UTC until the upvalley flow became parallel to the valley axis in the center of the valley, exceeding phase II by three hours. In Fig. 3.10, the succession of multiple *cross+vpro* flights performed between 05 and 10 UTC (thus spanning the phases I-III) is presented. As explained in section 2.3.4, it is important to keep in mind that vertically pointing arrows in Fig. 3.10 display the *horizontal* wind direction, hence, a vertically pointing arrow does not indicate upward motion but southerly winds. At 0506 UTC, the predominant wind direction is south (cf. Fig. 3.10a). Then, the wind direction rotates counterclockwise to southeast at 0608 UTC (cf. Fig. 3.10b), then northeast at 0704 UTC (cf. Fig. 3.10c), then north-northeast at 0823 UTC (cf. Fig. 3.10d). Only at 0952 UTC is the average wind at the valley center (at 10 and 40 m AGL) from north rather than north-northeast (cf. Fig. 3.10e).

An interesting feature of the vertical profile at 0823 UTC is the westerly (instead of easterly) component above 2030 m AMSL (about 110 m AGL). The color-saturated arrows in Fig. 3.10d show a westerly component of approximately 0.1 to 0.5 $\mathrm{m\,s^{-1}}$ only. Some of the faint arrows which represent the measurements of single drone ascents show stronger westerly components of up to 1 $\mathrm{m\,s^{-1}}$ at 2030 m AMSL. This could indicate a cross-valley circulation with a lower branch from east to west and an upper branch from west to east.

3.2.3 Phase III – forenoon and afternoon

Phase III lasted from 0645 in the forenoon to 1435 UTC in the afternoon. In the forenoon, incoming short-wave radiation followed an almost ideal curve with only a few dips probably caused by clouds (cf. Fig. 3.6h). Convective cloud generation was inhibited by the reinforcing synoptic ridge in the first half of the day until approximately 12 UTC. Afterwards, with the approaching low-pressure system and decreasing atmospheric stability, cumulus clouds appeared more frequently, visible in the higher frequency of dips in the curves of incoming short-wave and net radiation. During the longer dip around 0830 UTC, the AWRS potential temperature gradient tended towards zero, indicating neutral stratification which reverted back to superadiabatic stratification when direct solar radiation was present again.

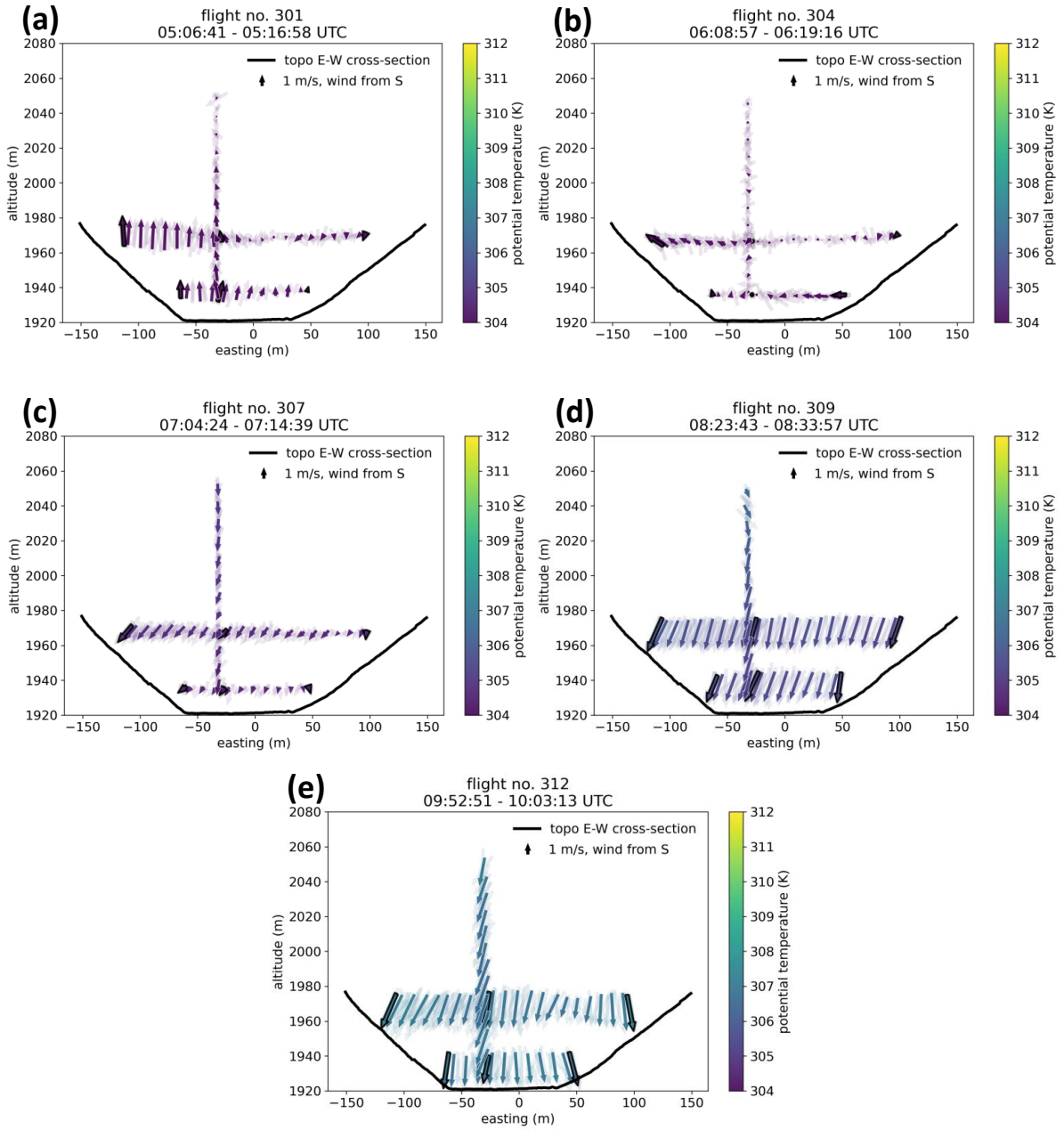

Figure 3.10: Figure belongs to phases I-III. Illustrated are five *cross+vpro* flights from early morning to noon on 23 June 2022: (a) flight no. 301 at 0506-0526 UTC, (b) flight no. 304 at 0608-0619 UTC, (c) flight no. 307 at 0704-0714 UTC, (d) flight no. 309 at 0823-0833 UTC, (e) flight no. 312 at 0952-1003 UTC. Each panel shows the *cross* flight at 10 m AVFL, the *cross* flight at 40 m AVFL, and the *vpro* flight up to 120 m AVFL. The direction of the arrows indicates the horizontal wind direction (upward pointing arrow indicates southerly wind), length indicates wind speed, color indicates potential temperature. Faint arrows correspond to single flight legs. Color-saturated arrows are bin-averaged flight legs. Measurements at locations where the UAS hovered for 30 s are marked with a black edge. The black thick line illustrates the topography along the cross-valley transect at the southern lake shore where the *cross* flights were performed.

The convective conditions are reflected also in the increase in wind speed of the thermally-driven upvalley flow: the upvalley wind component extended from approximately $1\,\mathrm{m\,s^{-1}}$ on average (cf. Fig. 3.10c) to 3 to $4\,\mathrm{m\,s^{-1}}$ (cf. Fig. 3.10d-e). The sonic anemometer at the valley ground determined maximum 5-minute values to also be in the range of 3 to $4\,\mathrm{m\,s^{-1}}$ (cf. Fig. 3.6b).

3.2.4 Phase IV – late afternoon

Between 1435 and 1440 UTC, the wind regime at the AWRS changed, defining the beginning of phase IV. The phase lasted until 1750 UTC. South foehn reached the Nafingalm valley floor in the afternoon, causing a wind direction change from northerly to southerly (cf. Fig. 3.6a). Wind speed maxima of the 5-minute averages displayed in Fig. 3.6b increased from approximately $3\,\mathrm{m\,s^{-1}}$ to $5\,\mathrm{m\,s^{-1}}$ and TKE at the ground reached its highest values of the day (cf. Fig. 3.6c). The foehn intrusion into the Nafingalm valley was associated with a temperature increase (cf. Fig. 3.6d and dashed green line in Fig. 3.6e) and moisture decrease (cf. Fig. 3.6f). At the same time, solar radiation suddenly reached higher values again after hours of fluctuations around lower values as the approach of warmer and dryer air masses might have led to cloud dissolution.

100 m higher than the valley floor, the south foehn was already detected earlier than at the valley ground. Figure 3.11 shows multiple plots of UAS flights during which the pattern *vpro+hover* was performed. It is important to note that the arrow direction represents only the north-south wind component of horizontal wind, and that southerly winds are represented by an arrow pointing from left to right (not upward, as in Fig. 3.10). At 1410 UTC, upvalley flow occurred throughout the depth of the leftmost profile, at the central profile below 1980 m AMSL, and at the rightmost profile below 1960 m AMSL (cf. Fig. 3.11a-b). Above 1960 m AMSL, the rightmost profile shows southerly winds. The southerly airflow was warmer by about 1.5 K (cf. Fig. 3.11a) and dryer by about $1.5\,\mathrm{g\,kg^{-1}}$ (cf. Fig. 3.11b). Within 20 min, the wind changed to southerly winds between 30 and 120 m AGL at all three profiling locations (cf. Fig. 3.11c-d). At 1453 UTC, southerly winds prevailed at all profiling sites (cf. Fig. 3.11e-f).

At Kolsass, located 11 km north of Nafingalm in the Inn Valley, lidar measurements indicated southerly winds of at least $5\,\mathrm{m\,s^{-1}}$ after 1530 UTC above 1600 m AMSL (cf. Fig. 3.12) which is one hour later than the foehn onset at Nafingalm. However, one must keep in mind that the Nafingalm valley floor is at 1920 m AMSL and might thus have been exposed to foehn flow earlier.

An interesting feature can be seen in the lower left panel of Fig. 3.11). The leftmost profile shows higher potential temperatures, lower wind speeds, and slightly higher water vapor mixing ratio during the ascent than the other two profiles. A hypothesis is that the drone was measuring a thermal plume, but other processes such as rotors or foehn intrusions from above should also be considered. To further investigate this temperature

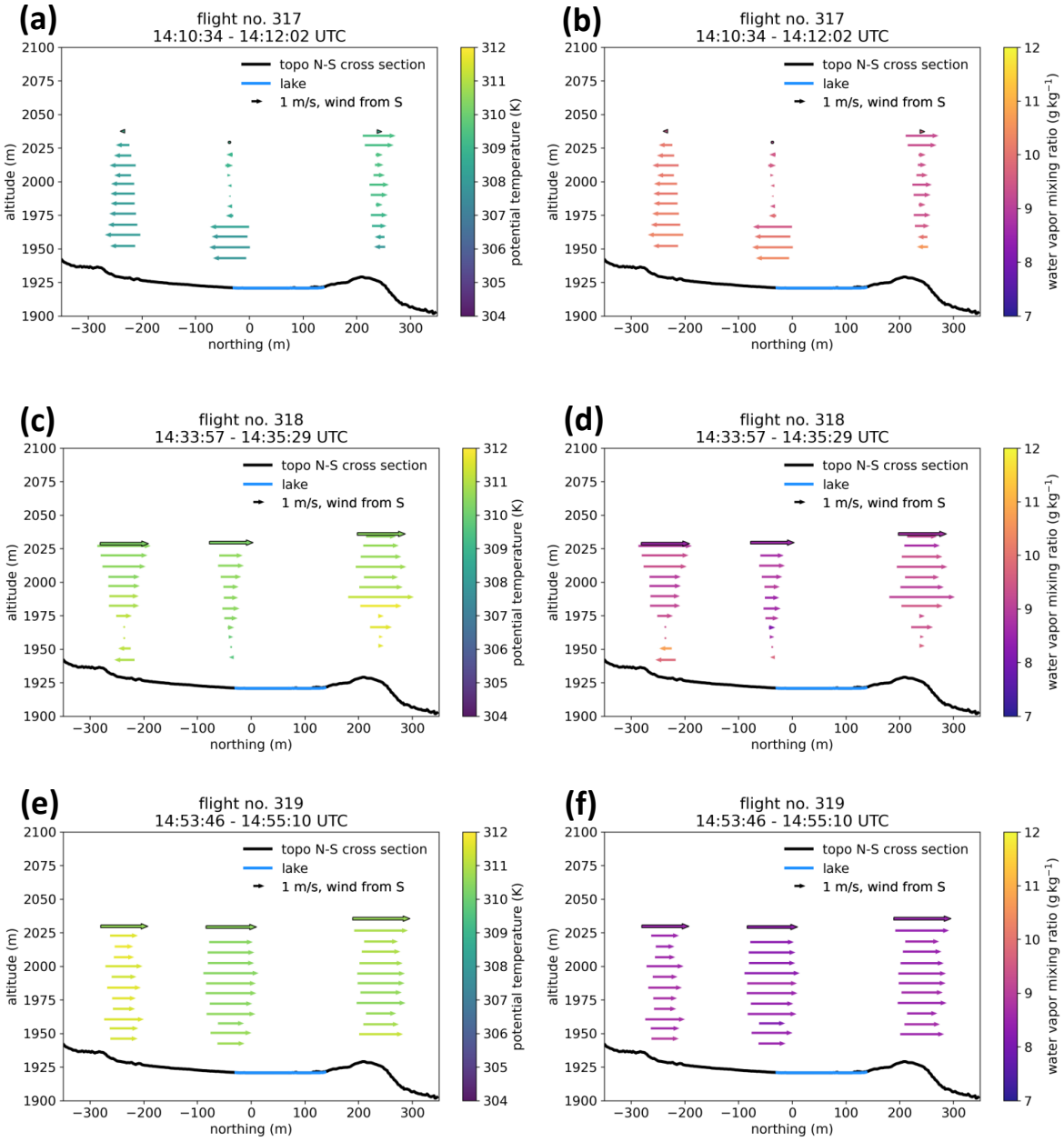

Figure 3.11: Figure belongs to phase IV. Illustrated is the succession of three *vpro+hover* flights on 23 June 2022. Each row is one time step: (a)-(b) flight no. 317 at 1410-1412 UTC, (c)-(d) flight no. 318 at 1433-1435 UTC, (e)-(f) flight no. 319 at 1453-1455 UTC. Each panel shows the *vpro* flights at the creek delta (left in each panel), at the southern lake shore (in the middle of each panel), and north of the lake (right in each panel). The direction of the arrows indicates the north-south wind component only (arrow pointing from left to right indicates southerly wind), the length indicates wind speed. The color indicates potential temperature in (a), (c), and (e), and water vapor mixing ratio in (b), (d), and (f). Measurements at the hover position are averaged and the corresponding arrow is marked with a black edge. The black thick line indicates the topography along the valley axis. The blue tick line indicates the position of the lake.

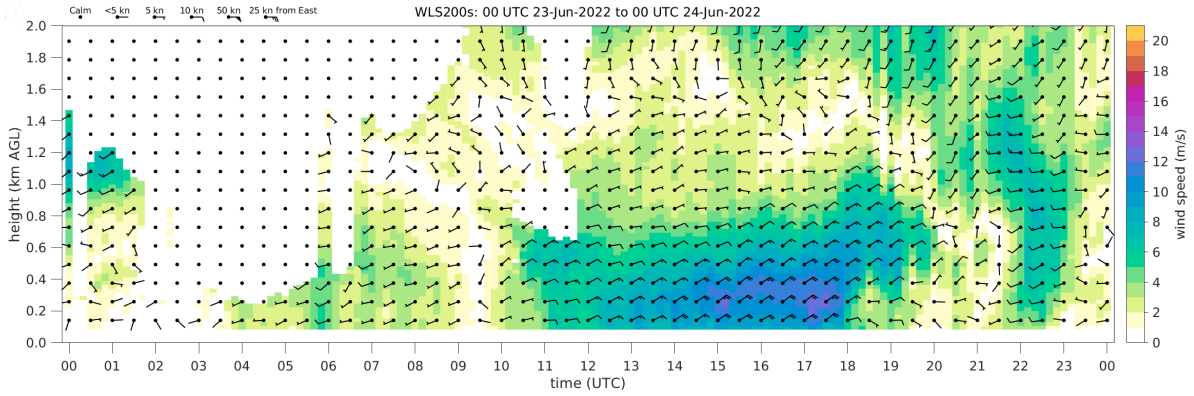

Figure 3.12: Figure belongs to phase IV. Illustrated are horizontal wind speed (color and wind barbs) and horizontal wind direction (wind barbs) measured at Kolsass on 23 June 2022 up to a height of 2 km AGL. Data collected by a WLS200s lidar owned and operated by KIT/IMK-TRO institute.

anomaly, a time series of flight no. 319 is shown (cf. Fig. 3.13). The different phases of the *vpro+hover* flight are displayed in Fig. 3.13a. The grey areas mark the vertical ascent and descent. The white area marks the hover period of the drone at an altitude of approximately 2040 m AMSL. The anomaly of potential temperature and other parameters occurred until 1457 UTC. The beginning of the anomaly cannot be clearly determined as not all parameters displayed in Fig. 3.13 provide reliable values during ascent. Hence, the time between the beginning of the hover period shortly after 1455 UTC and the red vertical line Fig. 3.13 is compared with the hover period after 1457 UTC. Potential temperature is significantly larger during UAS ascent and during the anomaly period as compared to the rest of the flight (cf. Fig. 3.13b). At 1457 UTC, temperature decreases abruptly by 1 K in less than a minute. Water vapor mixing ratio is difficult to evaluate as the noise is large (cf. Fig. 3.13c). However, there is a tendency of elevated values until 1457 UTC as compared to the average mixing ratio between 1457 and 1500 UTC. Furthermore, there is a dip slightly after 1457 UTC but it cannot be stated with certainty if it is physical or caused by measurement errors. Horizontal wind speed is lower at the beginning of the flight (cf. Fig. 3.13d). It increases between 1456 and 1457 UTC which is earlier than the drop in potential temperature. Vertical wind speed is not reliable during vertical ascent or descent of the drone, as explained in section 2.3.4, and may not be interpreted in absolute terms. However, it is possible to interpret the *change* of vertical wind speed during a hover period. After a phase of higher vertical velocity at the beginning of the hover period in flight no. 319, vertical wind speed abruptly decreases by about $2\,\mathrm{m\,s^{-1}}$ at 1457 UTC. The wind direction varies by $\pm 90°$ around south within the anomalous phase (cf. Fig. 3.13f) but wind direction variance is strongly reduced after approximately 1.5 min when potential temperature and water vapor mixing ratio were still elevated. For the interpretation of the anomaly, it might be important that at the

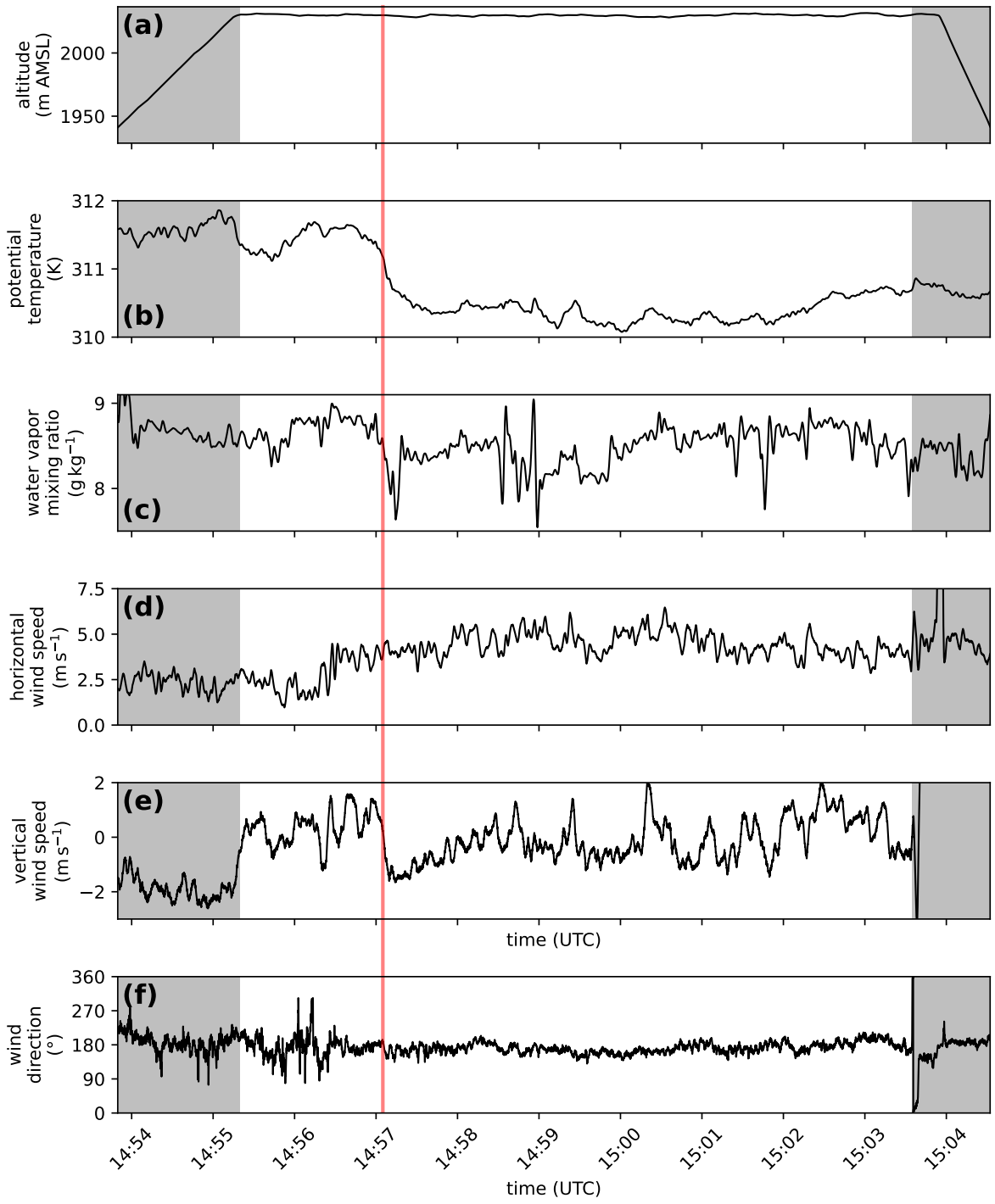

Figure 3.13: Figure belongs to phase IV. Illustrated is the time series of UAS *vpro+hover* flight no. 319 on 23 June 2022 between 1454 and 1504 UTC at the creek delta. This flight is also displayed as the southernmost profile in Fig. 3.11e-f. Parameters displayed are (a) altitude, (b) potential temperature, (c) water vapor mixing ratio, (d) horizontal wind speed, and (e) vertical wind speed. Grey areas: periods of vertical ascent and descent. White area: hover period. Red line: end of the anomaly (details in the text). The UAS flight data were smoothed with a moving average of 2 s.

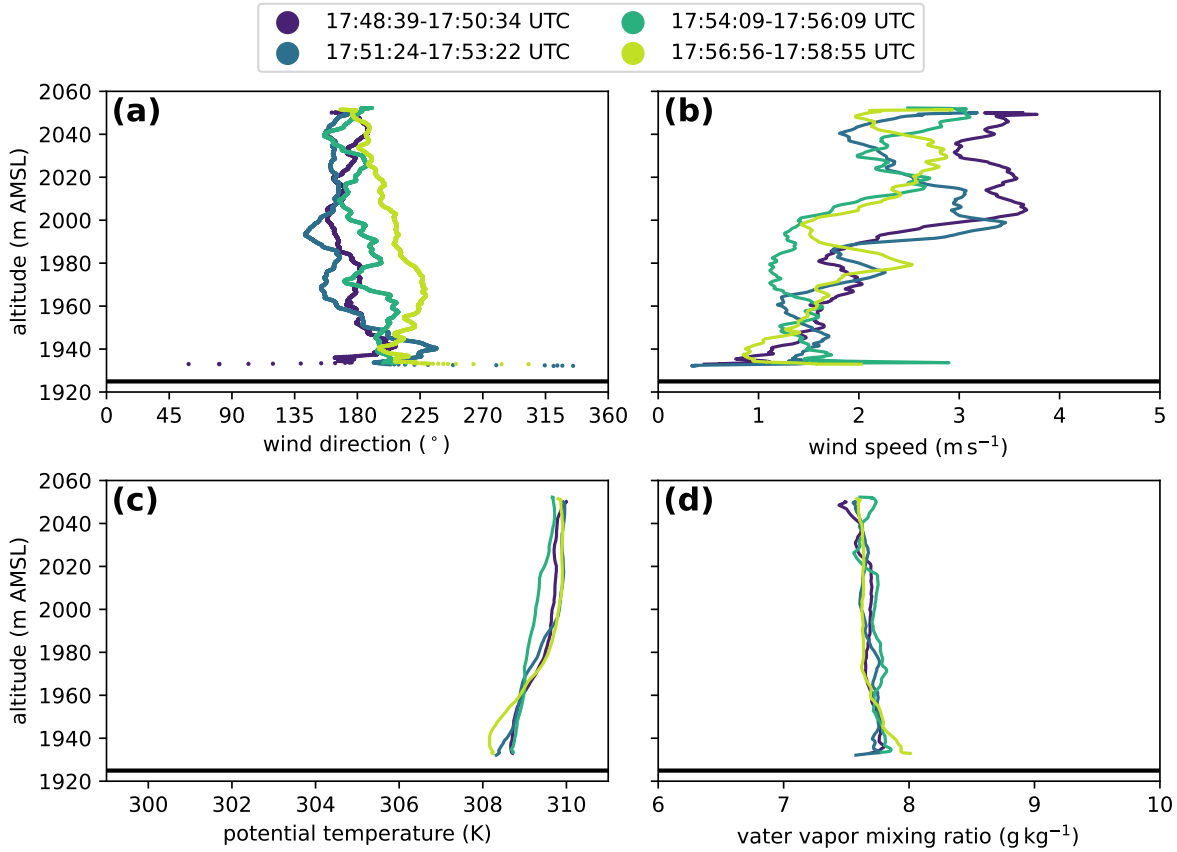

Figure 3.14: Figure belongs to phase V. Figure is as Fig. 3.7, at the same measurement location, on the same day, with the same moving average window, but for flight no. 322 between 1748 and 1758 UTC. The vertical profile of flight no. 322 is also illustrated in Fig. 3.16b.

time when the anomaly was observed, the AWRS north of the lake received full direct sunlight (cf. incoming short-wave radiation in Fig. 3.6f shortly before 15 UTC).

3.2.5 Phase V – evening

Phase V lasted from 1750 UTC to 1835 UTC. The phase was characterized by decoupling of the air layer adjacent to the ground from the higher-level flow due to the formation of a stable layer. A strong temperature decrease north and south of the lake (cf. Fig. 3.6d and green dashed line in Fig. 3.6e) indicated the formation of a cold-air pool (CAP) near the ground. The temperature decrease coincided with a cessation of the southerly winds in the evening. Instead, low winds from the north and from the west of less than $1\,\mathrm{m\,s^{-1}}$ were measured by the sonic anemometer (cf. Fig. 3.6a-b).

The formation of a CAP was also detected at the southern lake shore. Fig. 3.14c shows a decrease of potential temperature up to about 1960 m AMSL between 1754 and 1756 UTC. Between 1990 and 2030 m AMSL (depending on the time period), the border of a lower-wind-speed layer and a higher-wind-speed layer was observed (cf. Fig. 3.14b).

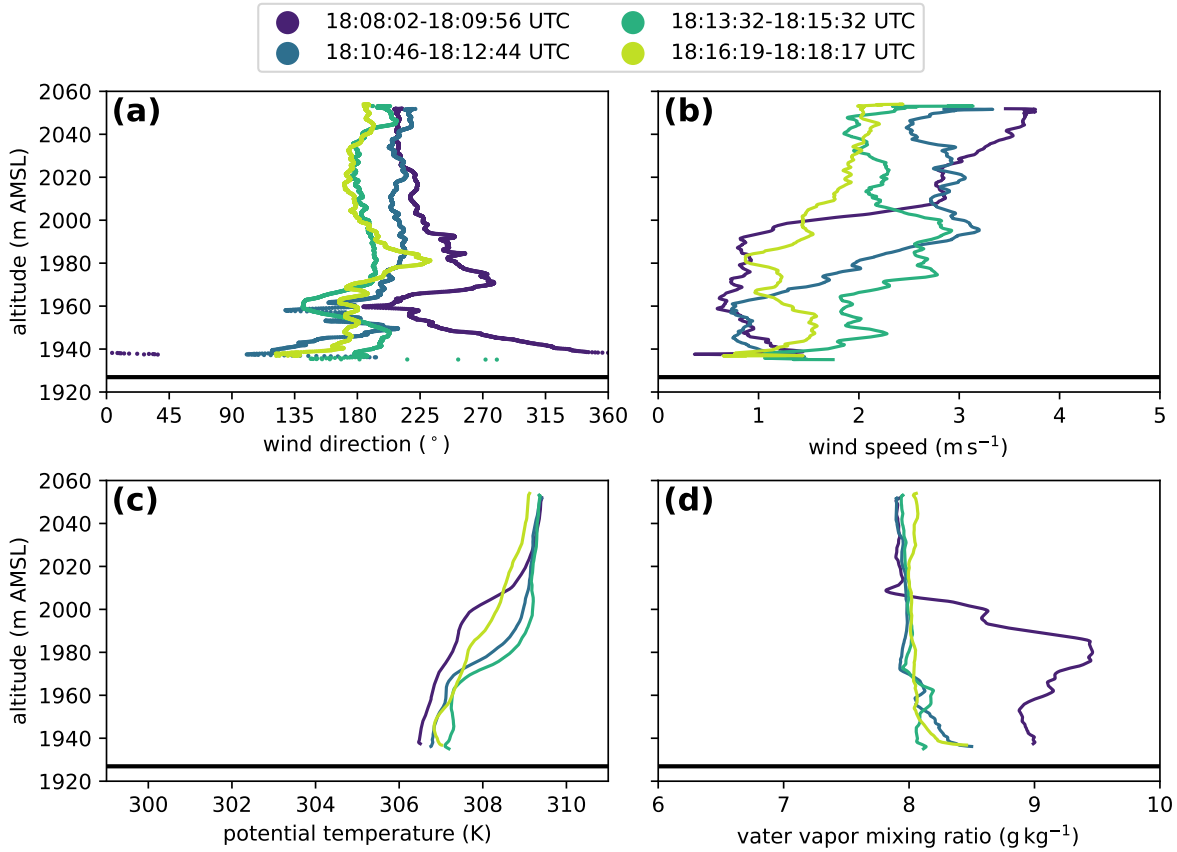

Figure 3.15: Figure belongs to phase V. Figure is as Fig. 3.14, at the same measurement location, on the same day, with the same moving average window, but for flight no. 323 between 1808 and 1818 UTC. The vertical profile of flight no. 323 is also illustrated in Fig. 3.16b.

This could indicate another layering of different wind regimes with remaining foehn flow lifted off the ground, persisting above a stable layer. At lower levels, further cooling between 1758 and 1808 UTC lead to a more pronounced stable layer with an upper limit varying between 1970 and 2000 m AMSL (cf. Fig. 3.15c). At 1808 and 1810 UTC, the height of that enlarged stable layer coincided with the wind speed profile indicating two layers (cf. Fig. 3.15b).

At 1808 and 1826 UTC, there was a westerly wind component in the layer up to 120 m AGL. This becomes evident when looking at the averaged vertical profile of wind direction and speed which is displayed by the color-saturated arrows in Fig. 3.16b-c. Analogous to cross-valley winds in the morning, this could indicate an evening cross-valley wind towards the sunlit west-facing slope, superimposed on the southerly flow above the stable layer. At the valley sidewalls, wind direction was variable. Some time steps show a wind component away from the slope, such as 1t 1748 UTC at the western slope at 10 m AVFL, at 1808 UTC at the western slope at 40 m AVFL, and at 1826 UTC at the eastern slope at 10 m AVFL (cf. Fig. 3.16a-c).

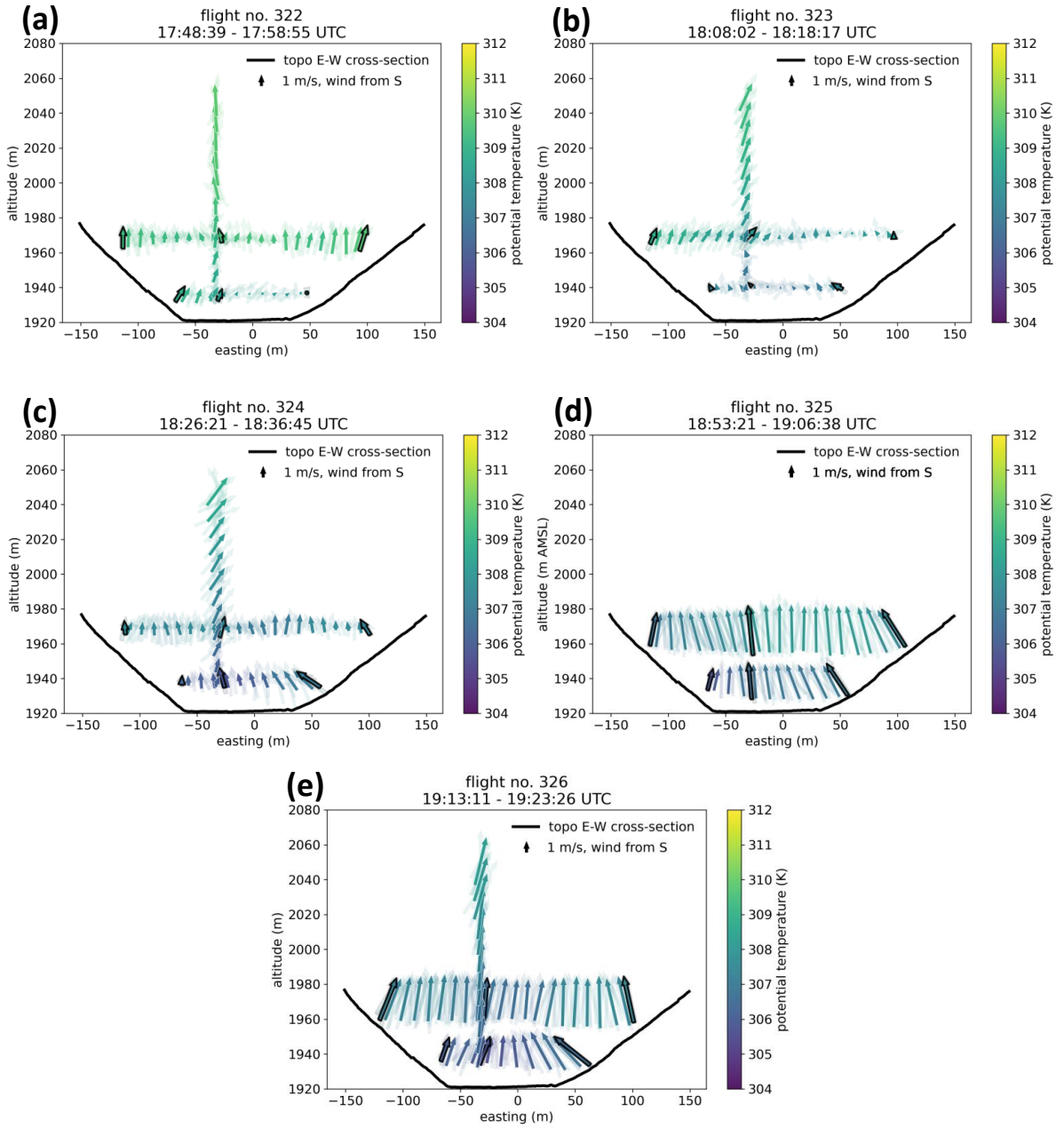

Figure 3.16: Figure belongs to phases V and VI. Illustrated are five successive *cross+vpro* flights on 23 June 2022. (a) Flight no. 322 at 1748-1758 UTC. (b) Flight no. 323 at 1808-1818 UTC. (e) Flight no. 324 at 1826-1836 UTC. (d) Flight no. 325 at 1853-1906 UTC, no *vpro* flight was performed. (e) Flight no. 326 at 1913-1923 UTC. Representation as in Fig. 3.10.

Another wind system might have played a role in phase V. The temperature difference between the land surface at the southern lake shore and the lake water changed its sign between 1740 and 1745 UTC (cf. black line in Fig. 3.6g), evolving to -2 K temperature difference at the end of phase V. The sign change from positive to negative coincided with the beginning of phase V. The question arose if the lake could have induced a lake breeze, contributing to the decoupling of the lower layer of air from the upper-level flow.

With the lake being warmer than the surrounding land at night, a temperature and thus pressure gradient could form, making air move towards the lake. At Nafingalm, this would translate to northerly winds at the sonic anemometer and southerly winds at the UAS at the southern lake shore. However, UAS data show varying wind directions close to the ground (potentially partially caused by the moving average) instead of a clear southerly direction throughout phase V.

A striking short-time feature in phase V is the high water vapor mixing ratio at 1808 UTC. Compared to the other ascents of flight 323, mixing ratio has increased values of up to $1.5\,\mathrm{g\,kg^{-1}}$ (cf. purple line in Fig. 3.15d). The anomaly corresponds to wind directions from north to south to west to north with height (cf. Fig. 3.15a). Advection from northerly and westerly directions (corresponding to the lake and the marshy shore of the lake) could explain the enhanced mixing ratio.

3.2.6 Phase VI – late evening

Phase VI lasted from 1835 until 2100 UTC. After 1835 UTC, a sudden increase in wind speed coincided with a sudden increase in temperature and a wind direction reversal back to southerly winds (cf. Fig. 3.6a, b, d), similar to phase IV. Temperature then remained approximately constant for 1.5 h, indicating enhanced mixing as no typical nighttime cooling occurs. These observations point to another phase of south foehn at Nafingalm. The only parameter that does not match the expectations is water vapor mixing ratio, which kept increasing instead of decreasing at the same time as temperature increased. However, after half an hour, the mixing ratio started to decrease, coinciding with the wind speed reaching $5\,\mathrm{m\,s^{-1}}$. The half hour of increasing mixing ratio might have been a transitional period between the regime of phase III and that of phase IV.

The increasing southerly wind measured north of the lake corresponds to UAS measurements at the southern lake shore. Figure 3.16 shows the three *cross+vpro* flights performed between 1826 and 1923 UTC. No vertical profile was measured during flight no. 325 (cf. Fig. 3.16d). Flight no. 324 has taken place at the end of phase V. It shows a higher variability in wind direction as compared to flights no. 325 and 326 (cf. Fig. 3.16c-e). The succession from flight no. 324 to flight no. 325 illustrates the increase in wind speed, even though part of the reason for lower wind speed in Fig. 3.16a is mathematical as the higher directional variability leads to smaller averaged wind speeds. Potential temperature was lower at lower levels, indicating stable stratification (cf. Fig. 3.16c-e). Within the 20 min between flights no. 325 and 326, cooling happened in the central valley area by approximately 1.5 K for both the UAS at 10 m and the UAS at 40 m AVFL (cf. Fig. 3.16d-e). This could indicate a mixing processes. The arrows close to the valley side walls show a slope-normal wind component. This characteristic is strongest at the eastern slope at the lower *cross* flight level for both 1852 and 1913 UTC (cf. Fig. 3.16d-e). During the UAS measurements, it was visually observed that the gully east of the *cross* flight

Figure 3.17: Photo belongs to phase VI. View from the marshland southwest of Nafing Lake towards east northeast. Photo taken at 1919 UTC on 23 June 2022. Red arrow indicates potential air channeling by the gully. Red circle marks the position of the yellow textile wind vane used for visual observation of the wind. Credits: Norman Wildmann, adapted photograph.

trajectories locally channeled the air. The gully is associated with a creek at the eastern slope, illustrated in the map in Fig. 2.2. The channeling could explain the pronounced slope-normal wind components at 10 m AVFL (cf. Fig. 3.16a-c).

3.2.7 Phase VII – night

Phase VII actually comprises three phases, VII.i, VII.ii, and VII.iii, within the time period from 2110 to 0000 UTC (in Fig. 3.6, only "VII" is annotated"). No UAS flights were done during phase VII, hence, only ground-based data are available for these phases. In short, phases VII.i–VII.iii can be described as "decoupling, mixing, and again decoupling". The decoupling phases VII.i and VII.iii reflect certain characteristics of phase V, and the mixing phase VII.ii reflects certain characteristics of phase VI, explained in the following.

At the end of phase VI, at 2030 UTC, cooling set in at the AWRS and the HOBO lake station (cf. Fig. 3.6d-e). Within half an hour, wind speeds decreased from 7 m s^{-1} to 1.5 m s^{-1}, and the scatter around southerly wind directions became larger (cf. Fig. 3.6a-b). As in phase V, the cooling indicates the formation of an SBL in phase VII.i and might have led to another period of near-ground air decoupling from upper-level flow. At 2230 UTC which is in phase VII.ii, temperatures at the AWRS and the HOBO lake station started increasing and wind speeds picked up, such as happened in phase VI. However, wind speeds were lower than in phase VI, with maximally 3 m s^{-1} as a 5-minute average. Wind direction kept being southerly until 23 UTC. The wind speed was rather low for foehn winds but the increasing temperatures near the valley ground indicate enhanced mixing as typical for a foehn-like flow. At 2315 UTC, in phase VII.iii, cooling set in another time

(cf. Fig. 3.6d and dashed line in Fig. 3.6e), wind speeds decreased (cf. Fig. 3.6b), and wind direction changed from southerly to northerly (cf. Fig. 3.6a). Again, the cooling led to the formation of an SBL, decoupling the near-ground air from higher-level flow. At midnight, another change of regimes took place towards reduced cooling, very low wind speeds, and southerly wind directions (not annotated with an own phase number in Fig. 3.6).

Chapter 4

Discussion

In this section, the results of the UAS measurements on 23 June 2022 are discussed. The discussion is structured by the different phases determined in section 3.2.

4.1 Phase I – early morning

Phase I comprises the second half of the night and the early morning until 06 UTC. The downvalley winds with stable stratification observed in that phase are typical for a nighttime MoBL. The stable layer with the coolest temperatures at the ground can be interpreted as a CAP. Statistical evaluations of three months of ground measurements during the TEAMx-PC22 show evidence for CAPs to be a frequent phenomenon at Nafingalm (Viebahn 2023).

4.2 Phase II – morning

Phase II lasted from 06 to 0645 UTC. Sunrise at Nafingalm on 23 June 2022 was already at 0317 UTC but the relevant point in time for the MoBL at in the Nafingalm valley to change from nighttime to daytime conditions is when the sun reaches the valley floor. The morning transition resembled that of a radiation day with a sudden onset of insolation at the valley floor, an abrupt increase in temperature, and a counterclockwise rotation of the wind within meters from the ground between 06 and 08 UTC (Viebahn 2023).

The cross-valley wind component observed during multiple hours in the morning could either be associated with upslope winds at the western valley side wall, or it could be part of a cross-valley circulation superimposed on the upvalley flow. UAS sampling the wind field in a cross-valley section could help to investigate this hypothesis.

Another possibility is that the flow meanders around the direction of the valley axis. However, all UAS measurements between 0823 and 0952 UTC (intermediate half-hourly steps not shown) only show northeasterly wind components below 2000 m AMSL (corresponding to approximately 80 m AGL), no northwesterly components. This is an argument

against meandering where one would expect to get a changing signal of wind direction also at lower altitudes for some of the measurement time steps.

4.3 Phase III – forenoon and afternoon

Phase III lasted from 0645 UTC to 1435 UTC. The northerly winds can be attributed to thermally-driven upvalley flow which is typical for Nafingalm not only for radiation days but also for average days including days with non-ideal radiation. Maximum upvalley wind speeds are usually higher on radiation days being in the range of 3 to $4\,\mathrm{m\,s^{-1}}$ as opposed to 1.5 to $3\,\mathrm{m\,s^{-1}}$ on average days (the given values are the 25th to 75th percentile; Viebahn 2023). The maximum values observed on 23 June 2022 rather match with the statistical values for radiation days.

The directional wind component at the valley side walls pointing away from the valley center could indicate upslope winds. The wind directions close to the valley side walls were never observed to be exactly slope-normal. This leads to the assumption that, if these winds actually are slope winds, they are usually superimposed by valley winds, as was also the case during other experiments, for example in the Dischma valley in Switzerland (Hennemuth and Schmidt 1985). Another possibility to explain the slope-normal wind component is that the slopes mechanically deflect the valley inflow horizontally (or also vertically) due to non-perfect north-south orientation of the valley side walls. Both effects, upslope winds and mechanical deflection, can superimpose.

To distinguish the two effects, measurements of the vertical wind component along a slope-normal trajectory would help. To achieve this, a UAS could hover at different distances from the slope, for example between 30 and 3 m distance, hovering every 3 m for a certain period of time. Then, the vertical velocities at all hover points within one flight could be compared. This way of discrete profiling could be performed either along a horizontal transect or along a transect perpendicular to the slope. For measuring very shallow flows ($\mathcal{O}(1\mathrm{m\,s^{-1}})$ or less), ground-based sensors for the three-dimensional wind vector, temperature, and humidity could be deployed at the western and eastern ends of the *cross* flight trajectories. The relative vertical wind component combined with the virtual potential temperature as a buoyancy measure could then be exploited to see if flow close to the slopes only moves horizontally along the valley side wall (horizontal deflection), moves upward without being buoyancy-driven (vertical deflection), or moves upward with being buoyancy-driven (upslope wind).

4.4 Phase IV – late afternoon

Phase IV from 1435 UTC until shortly before 18 UTC was characterized by foehn flow at the Nafingalm valley ground. The onset of foehn at Nafingalm between 14 and 15 UTC fits

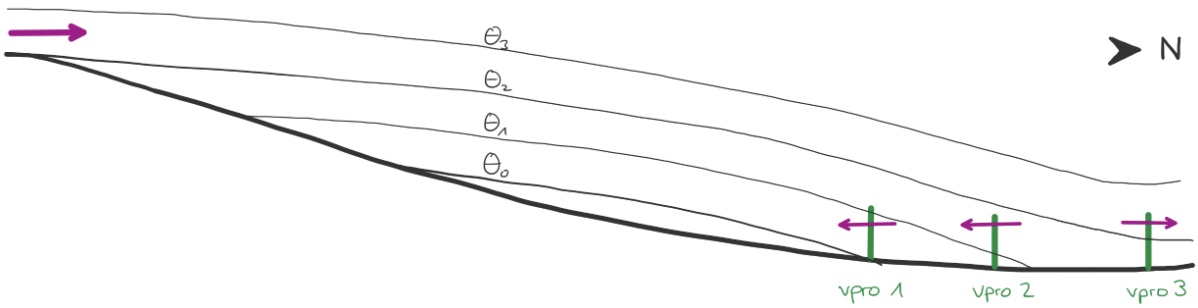

Figure 4.1: Schematic diagram of a vertical cross-section of Nafingalm showing a possible temperature distribution at 1410 UTC on 23 June 2022. Thick black line: topography from Geiseljoch in the south (left in the figure) to the measurement site north of Nafing Lake (right in the figure). Green vertical lines: trajectories of UAS vertical profiles. Thin black lines: isentropes with potential temperature increasing with height. Purple arrows: wind direction.

well with the observations of foehn in the Wipp Valley, the southerly flow above Kolsass, and the COSMO model predictions. Hence, it can be assumed that the large-scale forcing was not strong enough beforehand to establish foehn winds at Nafingalm earlier in the day. The successive wind direction reversal from upper to lower levels at Nafingalm could indicate erosion of relatively cooler valley air by mechanical turbulence (Haid et al. 2020) as the valley air was indeed cooler and also moister than the intruding airflow.

Why did the foehn air skip the southern profiling drones and reach the northernmost profiling drone first? Foehn air masses do not necessarily follow the lee side topography and remain close to the ground. Flow separation at the lee side of an obstacle and reattachment to the ground can occur (Jackson et al. 2013). If a certain air mass meets a relatively cooler air mass, the warmer air mass tends to stay above the cooler one due to buoyancy effects. However, if turbulence is involved, for example, due to wind shear between the two air masses, or waves, or rotors, the cooler air can be eroded by the warmer air above (Haid et al. 2020). The extent of penetration of warmer air into the lower layer can vary spatially. The isentropes (along which air parcels move in the absence of diabatic processes) in Fig. 4.1 show a possible distribution of air masses at Nafingalm at 1410 UTC on 23 June 2022. In the schematic diagram, the warmer southerly flow reaches down to vertical profile no. 3 (”vpro 3”) but not to vertical profiles no. 1 and 2 (”vpro 1” and ”vpro 2”), matching the observations displayed in Fig. 3.11.

What could have been a mechanical drive for the foehn layer to penetrate into the layer with prevailing upvalley winds? A possible explanation for the penetration of the warmer air at vertical profile no. 3 are trapped lee waves with a local minimum of the wave at the location of ”vpro 3”. In combination with these waves, rotor streaming can occur with rotors shearing off the crest of an obstacle such as a mountain or pass, moving downwind (Förchtgott 1957) and causing local turbulence. Such a rotor could also have been the cause for the intrusion into the lower layer of air at ”vpro 3”. However, trapped

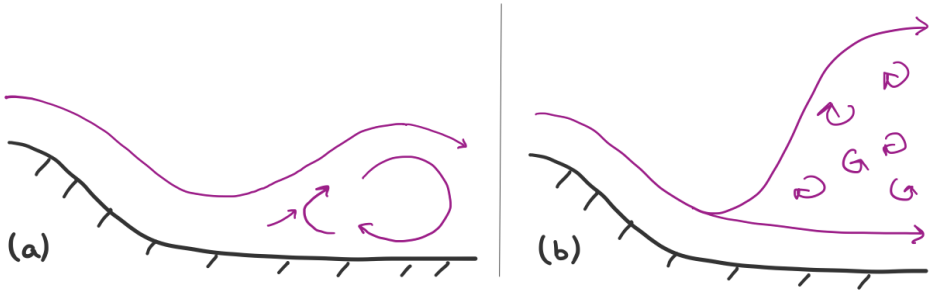

Figure 4.2: (a) Type I rotor below wave crest. The point where the flow detaches from the lee slope is a point of flow separation. (b) Type II rotor, also called hydraulic-jump-like rotor, with dividing streamline. The height of the rotor extends above the upstream height of the flow. Black thick line: topography. Purple: streamlines. Illustration by the author, based on Hertenstein and Kuettner (2005).

lee waves usually occur at wavelengths of 5 to 30 km (Jackson et al. 2013) which is large compared to the size of Nafingalm: the distance from the Geiseljoch pass to the vertical profile north of the lake is approximately 1.5 km and would correspond to a quarter of the wavelength. The whole wavelength of the wave would then be 6 km which is on the small edge of typical trapped lee waves. Hence, the hypothesis is unlikely.

Another possible explanation are foehn-induced rotors as described by Hertenstein and Kuettner (2005). They distinguish two types of rotors: the type I rotor (cf. Fig. 4.2a), and the type II, hydraulic-jump-like rotor (cf. Fig. 4.2b). For the type I rotor, one would expect a northerly flow component, opposed to the southerly foehn flow at "vpro 3", or turbulent flow with variable wind direction. However, the observations show a southerly wind component in "vpro 3", contradicting the hypothesis of a type I rotor. Furthermore, type I rotors are associated with trapped lee waves which were already discussed to be unlikely for Nafingalm. For the type II rotor, isentropes to the north of "vpro 3" would suddenly rise and the downstream flow would become very turbulent. As there were no measurements taken north of "vpro 3", this hypothesis cannot be confirmed or disconfirmed.

To further investigate phenomena that could potentially be larger than the scale that can be captured by UAS (120 m in the vertical), such as foehn flow and its spatial structure, it would be beneficial to add remote sensing at Nafingalm. A Doppler wind lidar could detect the flow towards and away from the lidar to investigate if and where at the slope between Geiseljoch and the valley floor flow separation occurs. Two lidars could yield even more information as two-dimensional wind vectors can be determined in the plane where the lidar scans overlap.

For the occurrence of the temperature anomaly at the creek delta during flight no. 319, multiple hypotheses can be formulated. One hypothesis is flow reversal forming on the lee-side of the barrier (Geiseljoch) opposing the foehn flow (Mursch-Radlgruber

1995). "Vpro 1" would then have been in an area where a wind direction opposing the foehn flow would be expected. The opposing wind direction would correspond to northerly flow. However, the north-south component of "vpro 1" shows southerly flow at all heights, contradicting this theory.

Another hypothesis is that potentially warmer air from higher levels locally penetrated the layer of air below, similar to the schematic in Fig. 4.1 but with the intrusion at "vpro 1" instead of "vpro 3". The air mass must have descended from at least the crest level at Geiseljoch, meaning a descent of 400 m. "Vpro 1" and "vpro 2" were horizontally only 200 m apart. It is surprising that a phenomenon of a vertical scale double as large as the horizontal scale of two separate UAS has not had any influence on "vpro 2". However, it remains possible that such an intrusion caused the temperature anomaly.

A third hypothesis is the occurrence of a thermal plume. For a buoyant plume, rising motion and a lower density than the one of surrounding air (achieved by higher potential temperature and/or higher moisture content) is expected. During the time the positive anomaly of potential temperature was observed, water vapor mixing ratio tended to be elevated. The vertical velocity, being about $2\,\mathrm{m\,s^{-1}}$ higher than that of the surrounding air mass, is reasonable for a thermal plume in the late afternoon with weakening solar forcing, and for a plume of a size restricted to a diameter of tens of meters. The estimation of the diameter results from the space available at the valley ground where the hypothetical plume must have formed. Horizontal wind speed was lower than at the other vertically profiling UAS and increased only after the occurrence of the anomaly. This might be explained by partial decoupling of the plume from the surrounding air. When detached from the ground, the plume is accelerated by the surrounding wind, but shortly after detachment it can still move at low horizontal speed. Furthermore, direct solar radiation had set in again shortly before the anomalous profile was sampled. This could have led to increased heating of the ground and consequently to an increased surface sensible heat flux from ground to air. However, it must be considered, as well, that the temperature anomaly occurred in the late afternoon when solar forcing was not strong anymore and surface sensible heat flux might have already changed sign at the creek delta.

In the future, it would be interesting to perform more *vpro+hover* flights at the creek delta to see if anomalies such as observed in this case occur frequently, and to evaluate their characteristics. Especially earlier during the day, with stronger solar forcing, thermal plumes would be expected to occur more often, hence, further measurements should be done between late forenoon and early afternoon.

4.5 Phase V – evening

In phase V from 1750 to 1835 UTC, a stable boundary layer (SBL) formed, decoupling the layer near the ground from higher level flow. It is possible that the upper-level flow,

which showed significantly higher wind speeds than measurements at ground level, was persisting foehn which had lifted off the ground. It was potentially superimposed by cross-valley winds towards the west-facing slope. The SBL formation was accompanied by weak, variable winds at low levels.

Slope-normal wind components at the valley side walls were weak and variable, too. They could indicate temporary downslope flow, or meandering flow, or could be caused by mechanical deflection by the valley sidewalls leading air to different directions depending on the incident angle of the air with respect to the slope.

Indications of winds matching the lake breeze pattern or contradicting it could not be determined for phase V due to too low wind speeds making the wind direction deteremined from UAS data unreliable. In his statistical analysis, Viebahn (2023) found that differences of water vapor mixing ratio up- and downstream of the lake are on average small. On the other hand, the UAS detected temporarily increased mixing ratios of 1.5 K on 23 June 2022 which might have been caused by the lake. What can be said for sure is that Nafing Lake is small as compared to lakes that are known to generate lake breezes, such as Lake Garda in Italy or Lake Annecy in France (Laiti et al. 2014; Chazette et al. 2021). The temperature difference between land and water was only beginning to develop in phase V and did hence not exceed 2 K. Furthermore, the air above the lake needs enough time for energy exchange with the water surface. As the fetch of Nafing Lake measures about 190 m in north-south direction, an air parcel at a horizontal speed of $1\,\mathrm{m\,s^{-1}}$ (average wind speed during phase V, cf. Fig. 3.6a) would only have about 3 min to warm up (or cool down for daytime lake breeze). An internal boundary layer forming over the lake would only be shallow. Thus, it is unlikely that a lake breeze can evolve at Nafingalm that is strong enough to be detected under disturbed conditions with an upper-level flow, such as on 23 June 2022.

4.6 Phase VI – late evening

The southerly winds in phase VI between 1835 and 2100 UTC could have been caused by foehn, thermally-driven katabatic winds, or a superposition of the two. Multiple arguments are in favor of foehn: During phase VI, there was no significant cooling despite negative radiative forcing (cf. Fig. 3.6h), indicating a mixing process. Furthermore, wind speeds were higher (5 to $7\,\mathrm{m\,s^{-1}}$, cf. Fig. 3.6b) than the typical wind speeds for radiation days at Nafingalm (2 to $4\,\mathrm{m\,s^{-1}}$, as analyzed by Viebahn (2023)), and higher wind speeds generally promote mixing. Moreover, the change in potential temperature in the central valley area detected during the UAS flights might have been due to mixing. A layer of air with higher wind speeds descended from 2010 to 1970 m AMSL between 1808 and 1816 UTC, 20 min before the onset of strong southerly winds at the Nafingalm valley

ground (cf. elevated high-wind-speed layer marked by the purple and the light green curve in Fig. 3.15b).

Other arguments that one could think of are the potential temperature difference between crest and valley-floor level, and the stratification: For assumed adiabatic descent of foehn air, it can be helpful to compare the potential temperature from Geiseljoch to the one at the AWRS. In case of adiabatic descent of foehn air into the valley, the potential temperatures should be the same. However, during descent along the lee slope, the foehn air could lose heat to the ground diabatically, by sensible heat flux towards the ground. For a distance of 1500 m between Geiseljoch and AWRS and a velocity of $5\,\mathrm{m\,s^{-1}}$, as was measured by the sonic anemometer, the foehn flow could cool during a period of 5 min. In that case, comparing potential temperatures from crest and valley ground level would not help in distinguishing foehn and katabatic flow. Another idea could be to consider stratification. For turbulent foehn flows, stratification is neutral. For katabatic downvalley and downslope winds, stratification is stable. However, foehn flows can also be slow and only weakly turbulent, keeping their stable stratification. This argument would hence not help, either, to distinguish the different flow types. All in all, it cannot be clearly answered if the winds in phase VI at Nafingalm were driven by foehn, thermally-driven katabatic winds, or a superposition of both. Yet, the observations mentioned above that are associated with increased mixing make the occurrence of foehn plausible.

In order to obtain more information about the flow type, one would need to know if and where flow originating from Geiseljoch detaches from the slope, i. e. where flow separation occurs. Therefore, a Doppler wind lidar scanning along the valley axis – or even better, two lidars at distributed locations, measuring along the valley axis the get a two-dimensional wind field in the plane in which the lidar scans overlap – could provide the required data. Furthermore, multiple surface stations from Nafing Lake up to Geiseljoch measuring potential temperature would provide information about the origin of air masses approaching Nafingalm from the south.

4.7 Phase VII – night

The phases VII.i from 2110 to 2230 UTC, VII.ii until 2315 UTC, and VII.iii until midnight are a further succession of changes between decoupling from upper-level flow and foehn-like winds. As for phase VI, it is questionable for phase VII.ii if the flow is actually foehn or thermally-driven katabatic flow. However, in the presence of katabatic flow, the temperature at the AWRS and the HOBO lake station would rather decrease instead of increase due to continued surface sensible heat flux towards the ground. Foehn, however, could induce mixing which can overcompensate the negative sensible heat flux to the ground, leading to increasing instead of decreasing temperatures. Hence, the wind regime in phase VII.ii can be attributed to foehn.

Chapter 5

Conclusions

In preparation for the TEAMx Observational Campaign (TOC) in 2024/2025, a pre-campaign was carried out in summer 2022 (TEAMx-PC22). One of the sub-target areas of TEAMx is Nafingalm, the head of a tributary valley of the Inn Valley. Besides ground-based measurements, airborne measurements were performed with a fleet of uncrewed aerial systems (UAS) at Nafingalm within the period from 20 to 28 June 2022. Simultaneous drone measurements were carried out at various points in space up to 120 m above the valley floor and along vertical and horizontal transects. In this study, the measurements between 20 and 28 June 2022 were described and the ground-based and airborne measurements on 23 June 2022 were analyzed in detail.

One question was which meteorological phenomena could be observed by UAS in the MoBL regarding multiscale wind systems and their interaction. The case study on 23 June 2022 revealed multiple processes, such as the thermally-driven down- and upvalley winds. The transition between the two states in the morning was associated with cross-valley winds. In the afternoon, south foehn penetrated Nafing Valley from above. The foehn layer was lifted off the ground by the formation of a cold-air pool, creating a stable boundary layer (SBL). In the late evening, a southerly flow re-established at the valley floor. In the night, alternating phases of decoupled SBL and elevated layer, and re-establishment of higher-speed southerly flow at the ground were observed. However, these last observations at night were only made by ground-based instruments as no UAS flights were performed after sunset.

A second question was which of the applied UAS flight patterns were suitable to capture different meteorological phenomena. All of the applied flight patterns contributed valuable information about the state and temporal evolution of horizontal wind speed and direction, temperature and relative humidity. The vertical profiles and hover flights were suited to detect stably stratified layers, layers with elevated wind speeds, and changes of wind speed and direction with height. Furthermore, atmospheric processes initiating at higher levels, such as foehn winds successively approaching the ground, could be captured before their signal reached the ground-based instruments. During horizontal *cross* flights,

transects were sampled continuously providing information not only about temperature and humidity but also about horizontal wind speed. To get a comparable amount of information by hovering drones only, at least ten UAS would have had to be operated simultaneously at 10 m AGL, and 20 UAS at 40 m. However, a limitation of *cross* flights is that the relative vertical velocity cannot be measured. With the setup used in this study, this is only possible with hovering drones.

For future measurements at Nafingalm, the focus of the measurements could be put on certain atmospheric processes and the instrumentation could be extended. To obtain information on the wind above the Geiseljoch pass in the south, a Doppler wind lidar could be used. RHI (Range Height Indicator) scans along the valley axis would provide spatial information of the flow towards and away from the lidar in that plane. The same technique could be applied along a cross-valley section. The DBS (Doppler Beam Swinging) or VAD (Velocity Azimuth Display) technique could be used to get a vertical profile of horizontal wind above the lidar. With a second lidar positioned south or north of the first one, a refined, two-dimensional picture of the wind in the vertical plane of the two lidars could be generated. Surface stations along the valley axis up to Geiseljoch could complement remote sensing as the lidar cannot measure within meters from the ground. The surface stations should be equipped not only with sensors for temperature and humidity but also for wind speed and direction.

To investigate slope winds, a UAS could measure relative vertical velocity at different distances from the slope, hovering at each distance for a certain period of time, hence, performing a discrete profile. The vertical velocities at all hover points within one flight could be compared. The sampling of the near-slope area by UAS could be performed simultaneously at multiple heights above ground. For the investigation of very shallow layers of air close to the slope, at a distance unsafe for UAS operation, ground-based instruments could be deployed. These instruments could be located where the UAS pattern suggested above is performed.

To analyze cross-valley circulation, UAS fleet measurements should be performed in a cross-valley plane. A possible flight pattern is a combination of discrete horizontal and discrete vertical profiles. One group of UAS could perform the horizontal profiles, and another group of UAS could profile vertically, with the two groups being separated in along-valley direction by a few meters to avoid collisions. The wind field of absolute horizontal velocities could then be combined with information about the relative vertical velocities of each profile. Two Doppler wind lidars could scan the cross-valley plane to obtain the two-dimensional wind field within that plane for heights above the maximum allowed UAS operation height.

In summary, different wind systems including local thermally-driven winds, mesoscale foehn winds, and their interaction were detected at Nafingalm on 23 June 2022 by performing measurements with a small fleet of UAS. All UAS flight patterns proved to be suitable

to contribute valuable information about wind, temperature, and moisture distribution. The measurement location and the UAS fleet measurement technique, complemented by further ground-based and remote-sensing instrumentation, can be considered appropriate for further experiments as envisaged for the TOC.

Appendix A

Wind algorithm

The algorithm to detect the horizontal wind vector was described by Wetz et al. (2021) and extended by Wetz and Wildmann (2022).

To understand the algorithm, it is important to consider the various frames of reference involved: the body-fixed frame (index b), the local North-East-Down (NED) frame (index n), and the meteorological frame (index m), illustrated in Fig. A.1. It is to be noted that the direction "north" in the NED frame and the meteorological frame refers to the magnetic north, not the geographic north. The declination (deviation of magnetic north from geographic north) is neglected in the wind algorithm. The error was on the order of up to $\mathcal{O}(5°)$ for central Europe at the time the measurements in the framework of this study were done.

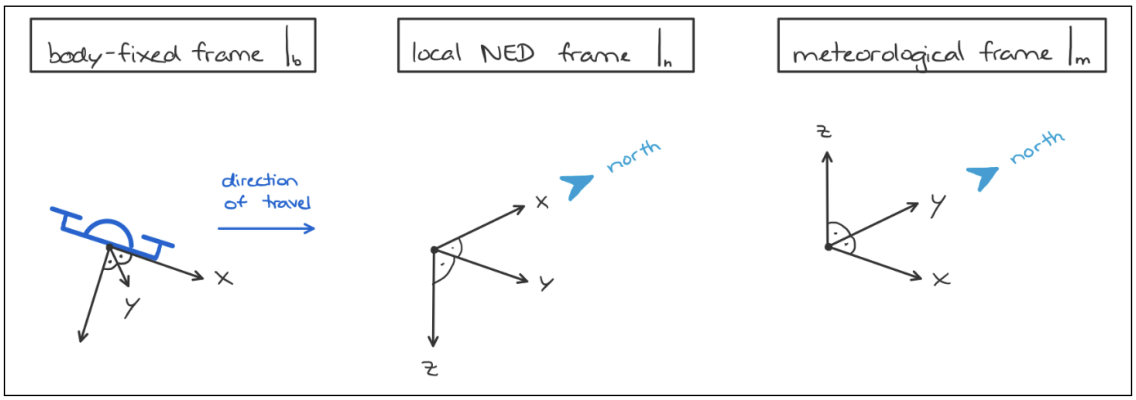

Figure A.1: Frames of reference used in the derivation of the wind algorithm. The local NED frame is the abbreviated local North-East-Down frame.

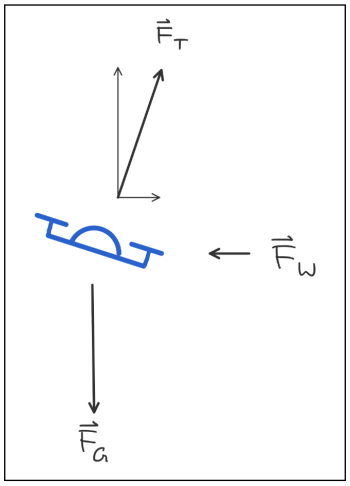

Figure A.2: Force balance in the absence of acceleration.

First of all, it is helpful to define three vectors: the position vector in the body frame $\mathbf{X_b}$, the vector of angular velocities around the x-, y-, and z-axis in the body frame $\omega_\mathbf{b}$, and the vector of attitude angles (also called Euler angles) in the NED frame $\mathbf{\Phi_n}$:

$$\mathbf{X_b} = [x \quad y \quad z]^T, \tag{A.1}$$

$$\omega_\mathbf{b} = [p \quad q \quad r]^T, \tag{A.2}$$

$$\mathbf{\Phi_n} = [\phi \quad \theta \quad \psi]^T. \tag{A.3}$$

If a UAS hovers and we assume no acceleration, then there is a force balance between gravitation $\mathbf{F_G}$, wind drag $\mathbf{F_W}$ and thrust $\mathbf{F_T}$ as illustrated in Fig. A.2:

$$\mathbf{0} = \mathbf{F_G} + \mathbf{F_W} + \mathbf{F_T}. \tag{A.4}$$

If the forces in eq. (A.4) are not balanced, there is a net acceleration $\ddot{\mathbf{X}}_\mathbf{n}$ in the NED frame. In the body frame, this acceleration translates to $\ddot{\mathbf{X}}_\mathbf{b} + \omega_\mathbf{b} \times \dot{\mathbf{X}}_\mathbf{b}$, a dynamic *plus* a gyroscopic term. The gyroscopic term appears because the UAS has three rotational degrees of freedom around its body-frame axes. Eq. (A.4) changes to

$$m\ddot{\mathbf{X}}_\mathbf{b} + m\ \omega_\mathbf{b} \times \dot{\mathbf{X}}_\mathbf{b} = \mathbf{F_{G,b}} + \mathbf{F_{W,b}} + \mathbf{F_{T,b}} \tag{A.5}$$

with m being the mass of the UAS. The cross product in the gyroscopic term $\omega_\mathbf{b} \times \dot{\mathbf{X}}$ yields

$$\begin{pmatrix} p \\ q \\ r \end{pmatrix}_b \times \begin{pmatrix} \dot{x} \\ \dot{y} \\ \dot{z} \end{pmatrix}_b = \begin{pmatrix} q\dot{z} - r\dot{y} \\ r\dot{x} - p\dot{z} \\ p\dot{y} - q\dot{x} \end{pmatrix}_b .$$

The gravitational force $\mathbf{F_G} = m\mathbf{g}$ contains the gravitational acceleration $\mathbf{g}$. In the NED frame, it is $\mathbf{g}_n = [0 \quad 0 \quad -g]^T$. In the body frame, it can be expressed using pitch and roll angle:

$$\mathbf{g_b} = \begin{pmatrix} \sin\theta \\ \cos\theta \sin\phi \\ \cos\theta \cos\phi \end{pmatrix}_b .$$

The wind drag force is expressed with a minus sign as, at least for the x-direction, the wind drag acts in negative x-direction in the body frame:

$$\mathbf{F_{W,b}} = -\begin{pmatrix} F_{W,x} \\ F_{W,y} \\ F_{W,z} \end{pmatrix}_b .$$

The thrust was also chosen to be expressed with a minus sign as it acts in negative z-direction in the body frame:

$$\mathbf{F_{T,b}} = -\begin{pmatrix} 0 \\ 0 \\ F_{T,z} \end{pmatrix}_b .$$

Altogether, eq. (A.5) becomes

$$m\begin{pmatrix} \ddot{x} \\ \ddot{y} \\ \ddot{z} \end{pmatrix}_b + m\begin{pmatrix} q\dot{z} - r\dot{y} \\ r\dot{x} - p\dot{z} \\ p\dot{y} - q\dot{x} \end{pmatrix}_b = mg\begin{pmatrix} \sin\theta \\ \cos\theta\sin\phi \\ \cos\theta\cos\phi \end{pmatrix}_b - \begin{pmatrix} F_{W,x} \\ F_{W,y} \\ F_{W,z} \end{pmatrix}_b - \begin{pmatrix} 0 \\ 0 \\ F_{T,z} \end{pmatrix}_b . \tag{A.6}$$

To determine the horizontal wind vector, we consider only the horizontal components of eq. (A.6). Actually, part of the z_b-component in the body frame would contribute to the x_n- and y_n-component in the NED frame but since pitch and roll angles are assumed to be small, the contribution of z_b to the horizontal wind components is also small and will be neglected. Hence, the horizontal components of eq. (A.6) can be written as

$$m\ddot{x} + m(q\dot{z} - r\dot{y}) = mgsin\theta - F_{W,x}, \tag{A.7}$$

$$m\ddot{y} + m(r\dot{x} - p\dot{z}) = mg\cos\theta\sin\phi - F_{W,y}. \tag{A.8}$$

Wetz et al. (2021) neglect all acceleration terms (dynamic and gyroscopic term), hence the left-hand side of equations (A.7) and (A.8) vanishes. Wetz and Wildmann (2022) neglect the gyroscopic terms as the variances of the gyroscopic terms are two orders of magnitude smaller than the variances of the dynamic term, but they do keep the dynamic term. Rearranging the equations then yields

$$F_{W,x} = mg\sin\theta - \ddot{x}, \tag{A.9}$$

$$F_{W,y} = mg\cos\theta\sin\phi - \ddot{y}. \tag{A.10}$$

Calibration coefficients c_i and d_i have been determined by Wetz and Wildmann (2022) to relate the wind drag force to the horizontal true airspeed (TAS) $\dot{x}_b$, $\dot{y}_b$ of the UAS:

$$\begin{pmatrix} \dot{x} \\ \dot{y} \end{pmatrix}_b = \begin{pmatrix} c_x F_{W,x}^{d_x} \\ c_y F_{W,y}^{d_y} \end{pmatrix}_b . \tag{A.11}$$

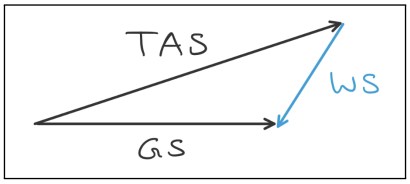

Figure A.3: The wind triangle relates true airspeed (TAS), ground speed (GS), and wind speed (WS). If TAS and GS are known, WS can be determined.

To get the TAS in the NED frame, the TAS in the body frame is multiplied by a rotation matrix $\mathbf{R}(\phi, \theta, \psi)$

$$\begin{pmatrix} \dot{x} \\ \dot{y} \end{pmatrix}_n = \mathbf{R}(\phi, \theta, \psi) \begin{pmatrix} \dot{x} \\ \dot{y} \end{pmatrix}_b \tag{A.12}$$

with the rotation matrix being

$$\begin{pmatrix} \cos\theta\cos\psi & \cos\psi\sin\theta\sin\phi - \cos\phi\sin\psi & \cos\psi\sin\theta\cos\phi + \sin\phi\sin\psi \\ \cos\theta\sin\psi & \cos\phi\cos\psi + \sin\theta\sin\phi\sin\psi & -\sin\phi\cos\psi + \sin\theta\cos\phi\sin\psi \\ -\sin\theta & \cos\theta\sin\phi & \cos\theta\cos\phi \end{pmatrix}.$$

Note that in the NED frame, x points towards the north, y points towards the east, and z points downward, whereas in the meteorological frame, x points towards the east, y points towards the north, and z points upward. To get TAS in the meteorological frame, the following operations are performed:

$$x_m = y_n, \tag{A.13}$$

$$y_m = x_n, \tag{A.14}$$

$$z_m = -z_n. \tag{A.15}$$

To determine the wind speed (WS), the ground speed (GS) of the drone has to be subtracted from the TAS as illustrated by the wind triangle in Fig. A.3 and as described mathematically in eq. (A.17). GS is determined by the GNSS sensor (hence, the quantity is denoted $\dot{x}_{GNSS}$, $\dot{y}_{GNSS}$) and is provided in the meteorological frame of reference.

$$WS = TAS - GS, \tag{A.16}$$

$$\begin{pmatrix} u \\ v \end{pmatrix}_m = \begin{pmatrix} \dot{x} \\ \dot{y} \end{pmatrix}_m - \begin{pmatrix} \dot{x}_{GNSS} \\ \dot{y}_{GNSS} \end{pmatrix}_m. \tag{A.17}$$

This way, the horizontal wind vector $[u \quad v]^T$ in the meteorological frame is found.

Wind direction A first guess of the wind direction Ψ is the yaw angle ψ of a drone as the drone is operated in weather-vane mode (rotating its nose towards the inflow). In the absence of acceleration, ψ corresponds to the actual wind direction (if one adds 180°). The 180° needs to be added in order to obtain a meteorological wind direction (the

direction where the wind *comes from*) instead of a mathematical direction (corresponding to the direction where the wind *goes to*), e. g. $\psi = 90°$ corresponds to a westerly wind, not to an easterly wind.

The only missing feature is that each drone has an individual offset $\Delta\psi$ resulting from possible errors made during the calibration of the magnetometers on-site. $\Delta\psi$ was not considered in the wind algorithm by the time the data analysis of this work was done. The error that is made by neglecting $\Delta\psi$ is on the same order of magnitude ($\mathcal{O}(5°)$) as the neglect of the declination.

In the presence of acceleration and especially in the case of forward flight, the orientation of the drone can deviate from the actual wind direction. The UAS nose will be directed towards the inflow which is a superposition of wind *and* the direction of travel of the UAS. Hence, the wind direction needs to be recomputed from the determined meteorological horizontal wind speeds u_m and v_m:

$$\Psi = \tan \frac{v_m}{u_m} + 180°. \tag{A.18}$$

The addition of 180° is, again, necessary to get the meteorological wind direction instead of a mathematical direction.

Appendix B

Measurement devices and locations

Table B.1 lists all measurement instruments used during TEAMx-PC22 at Nafingalm. Details on the single devices within the AWRS and the HOBO Stations are listed in the Bachelor's thesis of Viebahn (2023).

Table B.1: Measurement instruments used during TEAMx-PC22 at Nafingalm.

Site name	**Coordinates (lat/lon)**	**Site Altitude (m AMSL)**	**Height above ground (m AGL)**	**Instrument**	**Instrument abbreviation**	**Measured variables**	**Resolution**	**Deployment period (all in 2022)**
north of lake, south of lake at shore, south of lake at delta	47.2124 N 11.7132 E	1921 … 1928	0 … 120	SWUF-3D fleet of HolyBro QAV250	UAS	Ψ, u, v, w', T, RH, p	2 Hz, 1 Hz, 75 Hz	20-28 Jun
north of lake	47.21514 N 11.71263 E	1928	5	Metek Ultrasonic Anemometer Class A	sonic anemometer	u, v, w, T_v	10 Hz	20-28 Jun
north of lake	47.21514 N 11.71263 E	1928	0.8, 4.2	Automatic Weather and Radiation Station	AWRS	u, v, T, RH, p, R, S, RR	5 min	15 Jun - 12 Sep
north of lake	47.21514 N 11.71263 E	1928	0, 0.3, 2	HOBO MX2302, HOBO MX2201	HTRH	T, RH	5 min	16 Jun - 12 Sep
south of lake at shore	47.21276 N 11.71303 E	1921	0, 0.3, 2	HOBO MX2302, HOBO MX2201	HTRH	T, RH	5 min	16 Jun - 12 Sep
on the slope	47.20815 N 11.72120 E	2241	0, 0.3, 2	HOBO MX2302, HOBO MX2201	HTRH	T, RH	5 min	16 Jun - 12 Sep
on the crest	47.20294 N 11.73016 E	2531	2	HOBO MX2302	HTRH	T, RH	5 min	16 Jun - 12 Sep
in the lake	47.21360 N 11.71243 E	1921	-0.3, -1.0	HOBO MX2302	HT	T	5 min	16 Jun - 12 Sep

Appendix C

Protocol of UAS flights

Table C.1 lists all UAS flights performed during the measurement campaign at Nafingalm between 20 and 28 June 2022, including the mean quantities of wind speed, wind direction, the potential temperature gradient, and relative humidity. The mean quantities are taken from ground-based measurement stations, not from the UAS measurements. The flight numbers were chosen such that the first digit of the flight number corresponds to the second digit of the day of the month, e. g. flight no. 001 was performed on 20 June 2022, flight no. 101 was performed on 21 June 2023.

Table C.1: Protocol of UAS flights during 20–28 June 2022. The codes in the column "qav no" indicate: o (no problems detected), A (crash), U (incomplete flight, e. g. by earlier landing), Z (time delay, e. g. by later take-off), N (no measurement flight, e. g. manual test flight). Wind speed and direction are taken from the sonic anemometer at 5m AGL if available, otherwise from AWRS at 4 m AGL. The potential temperature gradient between 0.8 and 4 m AGL, measured at the AWRS. Relative humidity is an average of relative humidity at 0.8 and at 4 m AGL, measured at the AWRS.

date	no	time start utc	time end utc	qav no							flight pattern	wind speed (m/s)	wind dir (°)	pot. temp. grad. (K/m)	rel. hum. (%)
				25	28	29	30	31	32	33					
20.06.2022	001	18:20:00	18:25:00		U	o	o				vpro	1.4	246	0.12	81
20.06.2022	002	18:43:00	18:49:00		o	o	U				vpro	2.3	35	0.1	81
20.06.2022	003	18:56:00	19:02:00		Z	o	o				vpro	1.5	123	0.11	83
20.06.2022	004	19:31:00	19:37:00		o	o	o				vpro	2.9	143	0.28	89
21.06.2022	101	03:45:00	03:51:00		o	o	o				vpro	2.2	0	0.21	74
21.06.2022	102	03:56:00	04:02:00		o	o	o				vpro	2.7	175	0.39	76
21.06.2022	103	04:07:00	04:13:00		o	o	o				vpro	2	178	0.32	75
21.06.2022	104	04:17:00	04:23:00		o	o	o				vpro	2.7	175	0.38	72
21.06.2022	105	04:27:00	04:33:00		o	o	o				vpro	1.4	126	0.17	76
21.06.2022	106	04:36:00	04:42:00		o	o	o				vpro	1.5	69	0.31	74
21.06.2022	107	04:56:00	05:02:00		o	o	o				vpro	2	144	0.25	70
21.06.2022	108	05:04:00	05:10:00		o	o	o				vpro	1.8	13	0.21	75
21.06.2022	109	05:13:00	05:19:00		o	o	o				vpro	2.6	151	0.25	78
21.06.2022	110	05:21:00	05:27:00		o	o	o				vpro	1.3	130	0.27	74
21.06.2022	111	05:31:00	05:37:00		o	o	o				vpro	1.2	164	0.21	74
21.06.2022	112	05:39:00	05:45:00		o	o	o				vpro	1.6	149	0.33	72

Table C.1 continued from previous page

21.06.2022	113	05:49:00	05:55:00	o	o	o				vpro	1	145	0.38	72
21.06.2022	114	05:59:00	06:04:00	o	o	o				vpro	0.8	160	0.29	72
21.06.2022	115	06:08:00	06:14:00	o	U	o				vpro	1.6	75	0.31	70
21.06.2022	116	06:17:00	06:22:00	o		o				vpro	1.1	87	0.04	63
21.06.2022	117	06:30:00	06:36:00	o		o	o			vpro	1.3	24	-0.23	65
21.06.2022	118	06:39:00	06:45:00	o		o	o			vpro	1.8	90	-0.26	60
21.06.2022	119	06:48:00	06:54:00	o		o	o			vpro	2	34	-0.17	54
21.06.2022	120	06:58:00	07:04:00	o		o	o			vpro	2.9	21	-0.19	51
21.06.2022	121	07:26:00	07:38:00					o		hover+vpro	2.9	358	-0.17	52
21.06.2022	122	07:44:00	07:56:00	Z		o		U		hover+vpro	2.2	358	-0.22	62
21.06.2022	123	08:04:00	08:17:00	o		o		o		hover+vpro	2	357	-0.25	58
21.06.2022	124	08:21:00	08:34:00	o		o		Z		hover+vpro	2.2	3	-0.27	60
21.06.2022	125	08:41:00	08:54:00	o		o		o		hover+vpro	3.6	12	-0.12	50
21.06.2022	126	08:57:00	09:11:00	o		o		o		hover+vpro	4.7	11	-0.08	48
21.06.2022	127	09:15:00	09:28:00	o		o		o		hover+vpro	4.1	9	-0.16	47
21.06.2022	128	09:33:00	09:47:00	o		Z		o		hover+vpro	5.3	2	-0.14	48
21.06.2022	129	13:38:00	13:52:00	A		o		o		tower	5.2	169	-0.39	62
21.06.2022	130	14:37:00	14:50:00			A		o	o	tower	1.4	172	-0.52	70
21.06.2022	131	14:54:00	15:07:00			o		o	o	tower	1.9	177	-0.82	64
21.06.2022	132	15:10:00	15:24:00			o		o	o	tower	1.3	331	-0.59	64
22.06.2022	201	06:12:00	06:25:00			N				manual	1.7	47	-0.01	70
22.06.2022	202	06:29:00	06:33:00			o				cross	0.9	198	-0.13	67
22.06.2022	203	07:04:00	07:14:00			o				cross	1.3	32	-0.03	75
22.06.2022	204	07:52:00	08:01:00			o				cross	1.9	7	-0.21	63
22.06.2022	205	07:55:00	08:09:00					U		cross	1.9	4	-0.22	65

Table C.1 continued from previous page

22.06.2022	206	08:02:00	08:09:00			o			cross	1.9	359	-0.23	70
22.06.2022	207	08:13:00	08:25:00			o		o	cross	2	353	-0.24	74
22.06.2022	208	09:18:00	09:24:00			U			cross	1.7	1	-0.14	66
22.06.2022	209	09:25:00	09:38:00					U	cross	1.1	360	-0.13	64
22.06.2022	210	13:51:00	13:55:00	N					manual	2.4	349	-0.26	84
22.06.2022	211	14:07:00	14:12:00		o				manual vpro	2.7	354	-0.12	87
22.06.2022	212	14:15:00	14:16:00				N		manual	2.3	342	-0.09	88
23.06.2022	301	05:07:00	05:19:00	o	U	o			cross+vpro	1.9	168	0.37	82
23.06.2022	302	05:26:00	05:39:00	o	o	Z			cross+vpro	1.9	165	0.29	81
23.06.2022	303	05:48:00	06:01:00	o	o	Z			cross+vpro	1.4	164	0.35	80
23.06.2022	304	06:08:00	06:20:00	o	o	o			cross+vpro	1.4	79	0.24	72
23.06.2022	305	06:25:00	06:38:00	o	o	Z			cross+vpro	1.8	72	-0.09	66
23.06.2022	306	06:45:00	06:58:00	o	o	Z			cross+vpro	0.8	17	-0.25	64
23.06.2022	307	07:04:00	07:17:00	Z	o	o			cross+vpro	1.5	6	-0.31	65
23.06.2022	308	07:56:00	08:11:00	o	o	o			cross+vpro	1.8	2	-0.37	58
23.06.2022	309	08:23:00	08:37:00	Z	o	o			cross+vpro	2.2	359	-0.11	68
23.06.2022	310	08:51:00	09:04:00	o	o	o			cross+vpro	2	351	-0.36	63
23.06.2022	311	09:21:00	09:34:00	o	o	o			cross+vpro	3.5	1	-0.37	63
23.06.2022	312	09:52:00	10:05:00	o	o	o			cross+vpro	2.9	3	-0.36	62
23.06.2022	313	10:59:00	11:11:00			o			vpro	2.9	354	-0.31	65
23.06.2022	314	11:53:00	12:05:00			o			vpro	2.2	351	-0.32	65
23.06.2022	315	12:53:00	13:05:00			o			vpro	2.8	348	-0.28	66
23.06.2022	316	13:53:00	13:59:00	o					hover+vpro	2.7	0	-0.14	72
23.06.2022	317	14:10:00	14:22:00	o	o	o			hover+vpro	2	355	-0.12	73
23.06.2022	318	14:33:00	14:46:00	o	o	o			hover+vpro	2.5	169	-0.38	60

Table C.1 continued from previous page

23.06.2022	319	14:53:00	15:06:00	o	o	o			hover+vpro	3.9	172	-0.63	51
23.06.2022	320	15:14:00	15:27:00	o	o	o			hover+vpro	4.5	170	-0.5	50
23.06.2022	321	15:31:00	15:44:00	o	o	o			hover+vpro	4.2	164	0.02	53
23.06.2022	322	17:48:00	18:02:00	o	o	o			cross+vpro	0.8	293	0.17	59
23.06.2022	323	18:07:00	18:22:00	o	o	o			cross+vpro	0.9	147	0.21	70
23.06.2022	324	18:25:00	18:40:00	Z	o	A			cross+vpro	1.1	166	0.31	70
23.06.2022	325	18:52:00	19:07:00	o	o				cross	4.8	150	0.47	67
23.06.2022	326	19:12:00	19:27:00	o	o		o		cross+vpro	4.3	155	0.33	67
26.06.2022	601	17:02:00	17:08:00	o	o				vpro	4	186	0.15	46
26.06.2022	602	17:11:00	17:17:00	o	Z				vpro	4.9	186	0.2	47
26.06.2022	603	17:23:00	17:29:00	o	o				vpro	4.7	186	0.23	47
26.06.2022	604	17:32:00	17:38:00	o	o				vpro	4.9	186	0.21	45
26.06.2022	605	17:42:00	17:48:00	o	o				vpro	3.4	186	0.19	48
26.06.2022	606	17:51:00	17:57:00	o	o				vpro	3.6	186	0.2	46
26.06.2022	607	18:03:00	18:09:00	o	o				vpro	3.6	186	0.29	48
26.06.2022	608	18:11:00	18:17:00	o	o				vpro	5	186	0.32	49
26.06.2022	609	18:21:00	18:27:00	o	o				vpro	4.1	186	0.3	48
27.06.2022	701	05:09:00	05:23:00	o	o				hover+vpro	4.1	165	0.48	58
27.06.2022	702	05:30:00	05:44:00	o	o				hover+vpro	4.8	166	0.51	57
27.06.2022	703	06:00:00	06:14:00	o	A				hover+vpro	4.9	154	0.43	48
27.06.2022	704	06:30:00	06:44:00	o			Z		hover+vpro	5.9	151	-0.08	44
27.06.2022	705	07:00:00	07:14:00	A			o		hover+vpro	5.7	151	-0.17	42
27.06.2022	706	07:30:00	07:43:00				o	o	hover+vpro	5.1	186	-0.28	42
27.06.2022	707	08:00:00	08:13:00				o	o	hover+vpro	5.3	186	-0.34	45
27.06.2022	708	08:30:00	08:44:00				o	o	hover+vpro	5.9	186	-0.26	42

Table C.1 continued from previous page

27.06.2022	709	09:00:00	09:12:00				o	o	hover+vpro	6.2	186	-0.27	42
27.06.2022	710	09:30:00	09:44:00	N					manual	4.1	186	-0.37	40
27.06.2022	711	09:35:00	09:49:00				o		hover+vpro	4.2	186	-0.34	41
27.06.2022	712	10:00:00	10:14:00				o	o	hover+vpro	4.3	186	-0.41	41
27.06.2022	713	10:30:00	10:44:00	o			o		hover+vpro	5.1	138	-0.19	39
27.06.2022	714	11:04:00	11:19:00				N	N	manual	3.9	141	-0.19	37
27.06.2022	715	11:29:00	11:29:00			A			manual				
27.06.2022	716	11:30:19	11:30:46			N			manual	3.3	169	-0.27	37
27.06.2022	717	11:31:00	11:43:00		o				manual hover	4.7	150	-0.29	38
27.06.2022	718	11:50:00	12:05:00	N					manual	5.2	160	-0.35	39
27.06.2022	719	12:09:00	12:23:00				o	o	hover+vpro	5.6	165	-0.43	39
27.06.2022	720	12:30:00	12:43:00	o			Z		hover+vpro	4.6	159	-0.41	39
27.06.2022	721	13:00:00	13:13:00	o			o		hover+vpro	4.1	166	-0.46	38
27.06.2022	722	13:30:00	13:43:00	o			o		hover+vpro	4.8	158	-0.31	39
27.06.2022	723	13:51:00	14:06:00	o					manual hover	4.7	155	-0.28	40

Appendix D

Foehn diagrams

Figures D.1, D.2 and D.3 show measurements of multiple meteorological quantities at Steinach am Brenner, Ellbögen, and Innsbruck. The synopsis of potential temperature, relative humidity, wind speed, and wind direction can help to evaluate whether foehn occurred at the mentioned locations or not. Different combinations of these meteorological quantities can be used to obtain a probability for foehn occurrence (Plavcan et al. 2014).

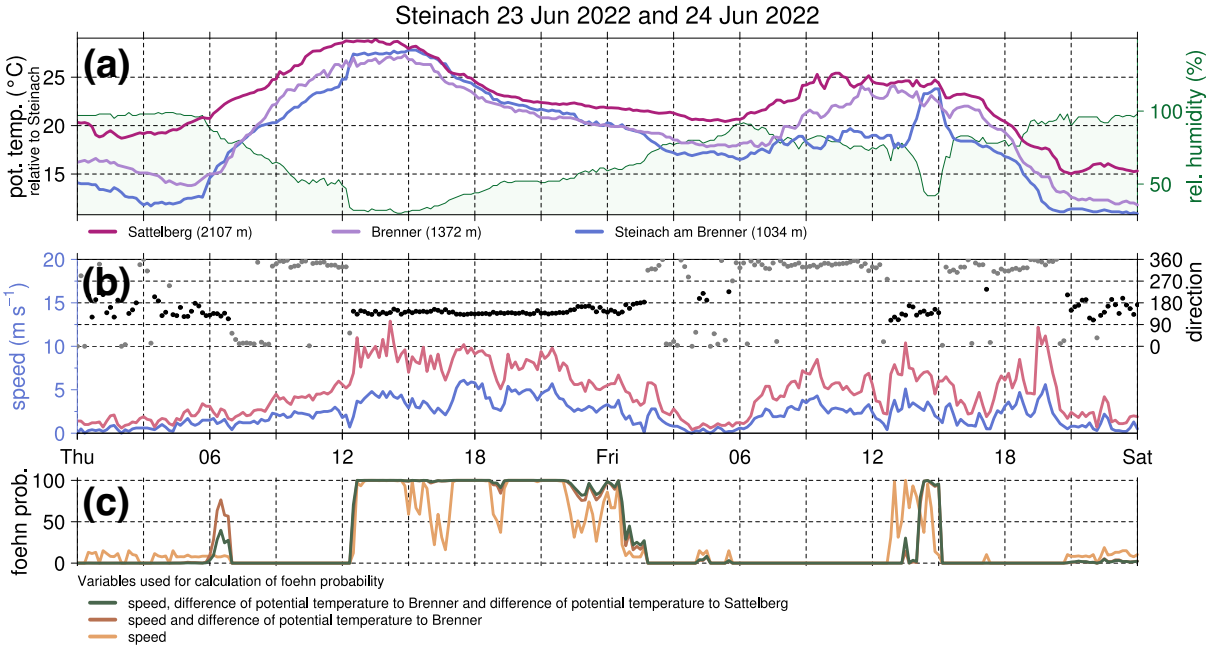

Figure D.1: Foehn diagram for Steinach in the Wipp Valley. (a) Potential temperatures at Sattelberg, Brenner, and Steinach. Relative humidity at Steinach. (b) Wind speed (blue line) and gusts (red line) and direction (dots) at Ellbögen. Dots indicating wind from the approximate south are printed in black. (c) Foehn probability following the classification and method by Plavcan et al. (2014). Figure provided by University of Innsbruck, Institute for Atmospheric and Cryospheric Sciences (2023).

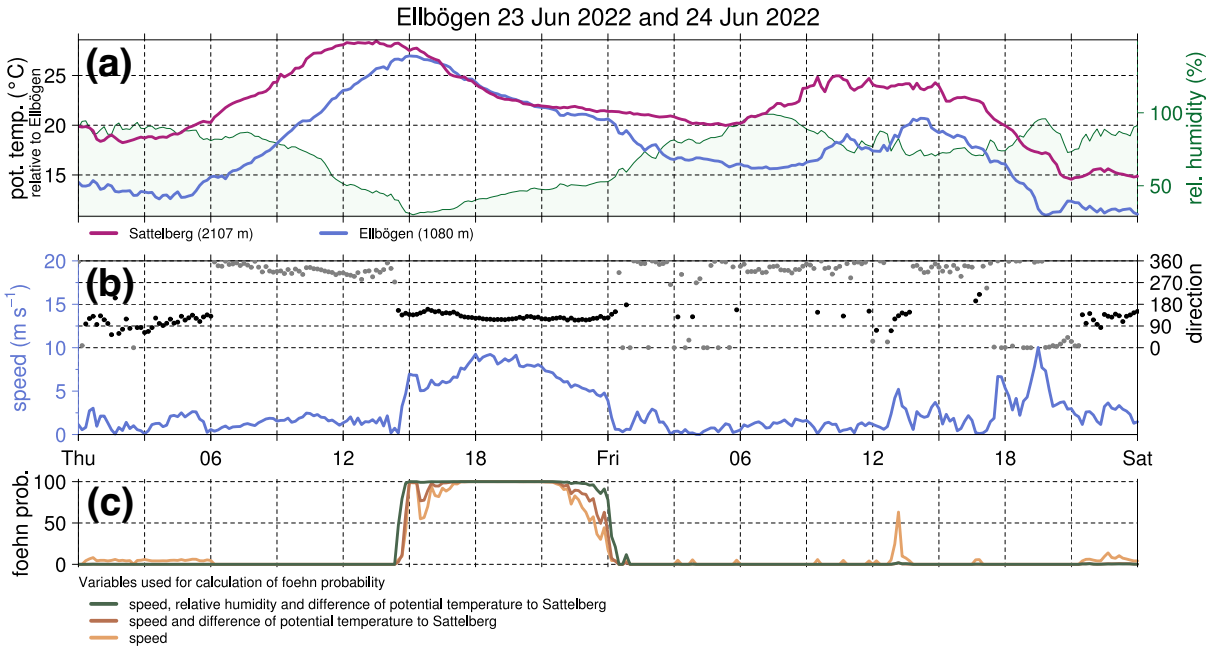

Figure D.2: Foehn diagram for Ellbögen in the Wipp Valley. (a) Potential temperatures at Sattelberg and Ellbögen. Relative humidity at Ellbögen. (b) Wind speed and direction at Ellbögen, no gusts displayed. Colors of (b) and (c) and source of the figure as in Fig. D.1.

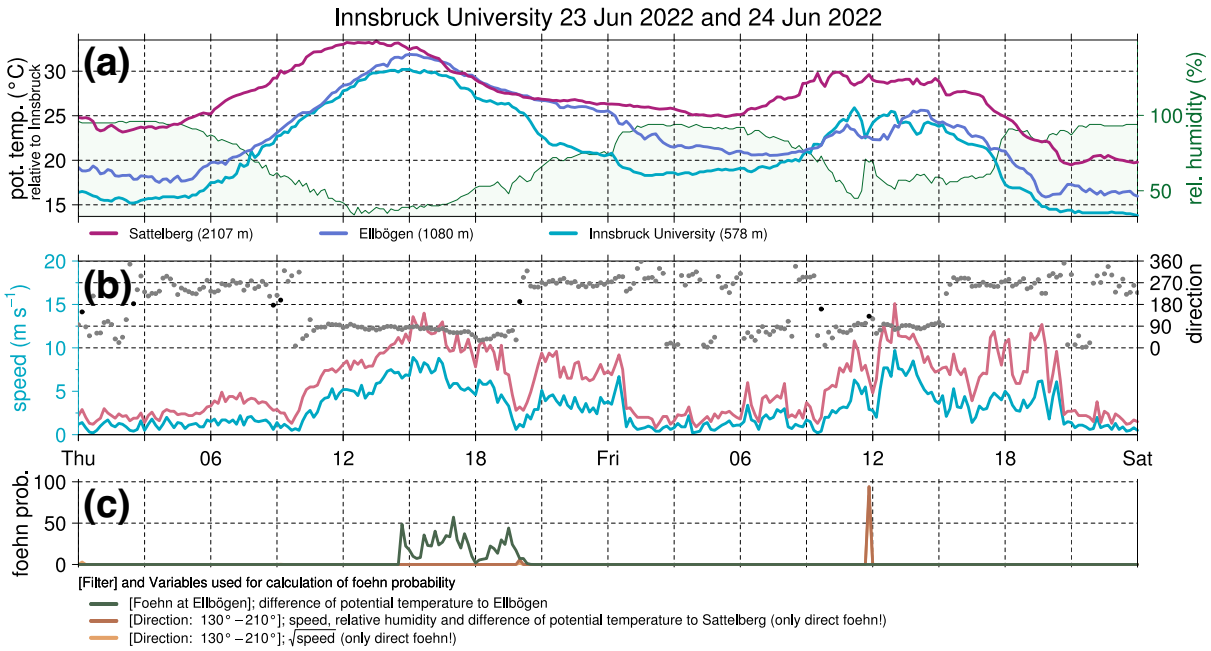

Figure D.3: Foehn diagram for Innsbruck north of the Wipp Valley. (a) Potential temperatures at Sattelberg, Ellbögen, and Innsbruck. Relative humidity at Innsbruck. (b) Wind speed, wind gusts, and direction at Innsbruck. Colors of (b) and (c) and source of the figure as in Fig. D.1.

Bibliography

Adler, B., et al., 2021: CROSSINN: A field experiment to study the three-dimensional flow structure in the Inn Valley, Austria. *Bulletin of the American Meteorological Society*, **102 (1)**, E38 – E60, doi:10.1175/BAMS-D-19-0283.1.

Babić, N., B. Adler, A. Gohm, N. Kalthoff, M. Haid, M. Lehner, P. Ladstätter, and M. W. Rotach, 2021: Cross-valley vortices in the Inn valley, Austria: Structure, evolution and governing force imbalances. *Quarterly Journal of the Royal Meteorological Society*, **147 (740)**, 3835–3861, doi:10.1002/qj.4159.

Bailey, S. C., S. W. Smith, M. P. Sama, L. Al-Ghussain, and G. de Boer, 2023: Shallow katabatic flow in a complex valley: An observational case study leveraging uncrewed aircraft systems. *Boundary-Layer Meteorology*, **186 (2)**, 399–422, doi:10.1007/s10546-022-00783-w.

Ban, N., et al., 2021: The first multi-model ensemble of regional climate simulations at kilometer-scale resolution, part I: evaluation of precipitation. *Climate Dynamics*, **57 (1)**, 275–302, doi:10.1007/s00382-021-05708-w.

Cetti, C., M. Buzzi, and M. Sprenger, 2015: Climatology of alpine north foehn. *Scientific Report MeteoSwiss*, **100**, 76.

Chazette, P., et al., 2021: Experimental investigation of the stable water isotope distribution in an Alpine lake environment (L-WAIVE). *Atmospheric Chemistry and Physics*, **21 (14)**, 10 911–10 937, doi:10.5194/acp-21-10911-2021.

Consortium for Small-scale Modeling, 2023: MeteoSwiss operational applications within COSMO. last access: 2023-11-13, URL `http://www.cosmo-model.org/content/tasks/operational/cosmo/meteoSwiss/`.

Defant, F., 1949: Zur Theorie der Hangwinde, nebst Bemerkungen zur Theorie der Berg- und Talwinde. *Archiv für Meteorologie, Geophysik und Bioklimatologie, Serie A*, **1 (3)**, 421–450, doi:10.1007/BF02247634.

Deidda, P., 2023: On the effect of tributary valleys on thermally driven winds in the main valley: a case study in the Inn Valley. M.S. thesis, University of Innsbruck, URL https://resolver.obvsg.at/urn:nbn:at:at-ubi:1-134436.

Durran, D. R., 1986: Another look at downslope windstorms. Part I: The development of analogs to supercritical flow in an infinitely deep, continuously stratified fluid. *Journal of Atmospheric Sciences*, **43 (21)**, 2527–2543, doi:10.1175/1520-0469(1986)043⟨2527:ALADWP⟩2.0.CO;2.

Egger, J., et al., 2002: Diurnal winds in the Himalayan Kali Gandaki valley. Part III: Remotely piloted aircraft soundings. *Monthly weather review*, **130 (8)**, 2042–2058, doi:10.1175/1520-0493(2002)130⟨2042:DWITHK⟩2.0.CO;2.

Ekhart, E., 1948: De la structure thermique de l'atmosphere dans la montagne [On the thermal structure of the mountain atmosphere]. *La Météorologie*, **4 (9)**, 3–26.

Elvidge, A. D. and I. A. Renfrew, 2016: The causes of foehn warming in the lee of mountains. *Bulletin of the American Meteorological Society*, **97 (3)**, 455–466, doi:10.1175/BAMS-D-14-00194.1.

Förchtgott, J., 1957: Active turbulent layer downwind of mountain ridges. *Studia Geophysica et Geodaetica*, **1 (1)**, 173–181.

Freitas, S., F. Harms, and B. Leitl, 2022: The influence of slopes of isolated three-dimensional valleys on near-surface turbulence. *Boundary-Layer Meteorology*, **182**, 55–74, doi:10.1007/s10546-021-00648-8.

Freytag, C. and B. Hennemuth, 1981: DISKUS — Gebirgswindexperiment im Dischmatal. Teil 1: Sondierungen. *Wiss. Mitt. Met. In st. München.*

Freytag, C. and B. Hennemuth, 1982: DISKUS — Gebirgswindexperiment im Dischmatal. Teil 2: Bodennahe Messungen und Flugzeugmessungen. *Wiss. Mitt. Met. Inst. München.*

Gagne, D., et al., 2023: mavlink/qgroundcontrol: v4.2.8. Zenodo, doi:10.5281/zenodo.8145392.

Gerken, T., T. Biermann, W. Babel, M. Herzog, Y. Ma, T. Foken, and H.-F. Graf, 2014: A modelling investigation into lake-breeze development and convection triggering in the Nam Co Lake basin, Tibetan Plateau. *Theoretical and applied climatology*, **117**, 149–167, doi:10.1007/s00704-013-0987-9.

Göbel, M., S. Serafin, and M. W. Rotach, 2023: Adverse impact of terrain steepness on thermally driven initiation of orographic convection. *Weather and Climate Dynamics*, **4 (3)**, 725–745, doi:10.5194/wcd-4-725-2023.

Gohm, A., 2023: TEAMx-PC22 (TEAMx pre-campaign 2022) - ACINN temperature and humidity logger data set from Nafingalm. Zenodo, doi:10.5281/zenodo.8232767.

Gohm, A. and G. Mayr, 2004: Hydraulic aspects of föhn winds in an Alpine valley. *Quarterly Journal of the Royal Meteorological Society*, **130 (597)**, 449–480, doi:10.1256/qj.03.28.

Gohm, A. and F. Obleitner, 2023: TEAMx-PC22 (TEAMx pre-campaign 2022) - ACINN automatic weather station data set from Nafingalm. Zenodo, doi:10.5281/zenodo.8172308.

Gohm, A., et al., 2009: Air pollution transport in an Alpine valley: Results from airborne and ground-based observations. *Boundary-layer meteorology*, **131**, 441–463, doi:10.1007/s10546-009-9371-9.

Graf, M., M. Kossmann, K. Trusilova, and G. Mühlbacher, 2016: Identification and climatology of Alpine pumping from a regional climate simulation. *Frontiers in Earth Science*, **4**, doi:10.3389/feart.2016.00005.

Haid, M., A. Gohm, L. Umek, H. Ward, T. Muschinski, L. Lehner, and M. Rotach, 2020: Foehn–cold pool interactions in the Inn Valley during PIANO IOP2. *Quarterly Journal of the Royal Meteorological Society*, **146 (728)**, 1232–1263, doi:10.1002/qj.3735.

Haid, M., A. Gohm, L. Umek, H. C. Ward, and M. W. Rotach, 2022: Cold-air pool processes in the Inn Valley during föhn: A comparison of four cases during the PIANO campaign. *Boundary-Layer Meteorology*, **182 (3)**, 335–362, doi:10.1007/s10546-021-00663-9.

Heimann, D., 1992: Numerical simulation of mesoscale structures in the northern Alpine foreland during front passages: A dry cold front with pre-frontal foehn. *Meteorologische Zeitschrift*, **1 (6)**, 290–306, doi:10.1127/metz/1/1992/290.

Hennemuth, B., 1986: Thermal asymmetry and cross-valley circulation in a small Alpine valley. *Boundary-layer meteorology*, **36**, 371–394, doi:10.1007/BF00118338.

Hennemuth, B. and H. Schmidt, 1985: Wind phenomena in the Dischma valley during DISKUS. *Archives for Meteorology Geophysics and Bioclimatology Series B Theoretical and Applied Climatology*, **35 (4)**, 361–387, doi:10.1007/BF02334490.

Hersbach, H., et al., 2023: ERA5 hourly data on pressure levels from 1940 to present. Copernicus Climate Change Service (C3S) Climate Data Store (CDS), last access: 2023-09-14, doi:10.24381/cds.bd0915c6, last access: 2023-09-14.

Hertenstein, R. F. and J. P. Kuettner, 2005: Rotor types associated with steep lee topography: Influence of the wind profile. *Tellus A: Dynamic Meteorology and Oceanography*, **57 (2)**, 117–135, doi:10.3402/tellusa.v57i2.14625.

Horst, R. and J. Doran, 1986: Nocturnal drainage flow on simple slopes. *Boundary-Layer Meteorology*, **34 (3)**, 263–286, doi:10.1007/BF00122382.

Jackson, P. L., G. Mayr, and S. Vosper, 2013: *Mountain weather research and forecasting*, chap. Dynamically-driven winds, 121–218. Springer, doi:10.1007/978-94-007-4098-3_3.

Jansing, L., L. Papritz, B. Dürr, D. Gerstgrasser, and M. Sprenger, 2022: Classification of Alpine south foehn based on 5 years of kilometre-scale analysis data. *Weather and Climate Dynamics*, **3 (3)**, 1113–1138, doi:10.5194/wcd-3-1113-2022.

Kirshbaum, D. J., B. Adler, N. Kalthoff, C. Barthlott, and S. Serafin, 2018: Moist orographic convection: Physical mechanisms and links to surface-exchange processes. *Atmosphere*, **9 (3)**, doi:10.3390/atmos9030080.

Klemp, J. and D. Lilly, 1975: The dynamics of wave-induced downslope winds. *Journal of Atmospheric Sciences*, **32 (2)**, 320–339, doi:10.1175/1520-0469(1975)032⟨0320:TDOWID⟩2.0.CO;2.

Laiti, L., D. Zardi, M. D. Franceschi, G. Rampanelli, and L. Giovannini, 2014: Analysis of the diurnal development of a lake-valley circulation in the Alps based on airborne and surface measurements. *Atmospheric Chemistry and Physics*, **14 (18)**, 9771–9786, doi:10.5194/acp-14-9771-2014.

Lehner, M. and A. Gohm, 2010: Idealised simulations of daytime pollution transport in a steep valley and its sensitivity to thermal stratification and surface albedo. *Boundary-layer meteorology*, **134**, 327–351, doi:10.1007/s10546-009-9442-y.

Lehner, M. and M. W. Rotach, 2018: Current challenges in understanding and predicting transport and exchange in the atmosphere over mountainous terrain. *Atmosphere*, **9 (7)**, doi:10.3390/atmos9070276.

Lehner, M., C. D. Whiteman, S. W. Hoch, D. Jensen, E. R. Pardyjak, L. S. Leo, S. D. Sabatino, and H. J. Fernando, 2015: A case study of the nocturnal boundary layer evolution on a slope at the foot of a desert mountain. *Journal of Applied Meteorology and Climatology*, **54 (4)**, 732–751, doi:10.1175/JAMC-D-14-0223.1.

Long, R. R., 1954: Some aspects of the flow of stratified fluids: II. Experiments with a two-fluid system. *Tellus*, **6 (2)**, 97–115, doi:10.1111/j.2153-3490.1954.tb01100.x.

Lugauer, M. and P. Winkler, 2005: Thermal circulation in South Bavaria - climatology and synoptic aspects. *Meteorologische Zeitschrift*, **14 (1)**, 15–30, doi:10.1127/0941-2948/2005/0014-0015.

Mann, J., et al., 2017: Complex terrain experiments in the New European Wind Atlas. *Philosophical Transactions of the Royal Society A: Mathematical, Physical and Engineering Sciences*, **375 (2091)**, doi:10.1098/rsta.2016.0101.

MeteoSwiss, 2023: COSMO-Prognosesysteme. last access: 2023-11-13, URL `https://www.meteoschweiz.admin.ch/wetter/warn-und-prognosesysteme/cosmo-prognosesysteme.html`.

Mikkola, J., V. A. Sinclair, M. Bister, and F. Bianchi, 2023: Daytime along-valley winds in the himalayas as simulated by the weather research and forecasting (wrf) model. *Atmospheric Chemistry and Physics*, **23 (2)**, 821–842, doi:10.5194/acp-23-821-2023.

Mursch-Radlgruber, E., 1995: Observations of flow structure in a small forested valley system. *Theoretical and applied climatology*, **52**, 3–17, doi:10.1007/BF00865503.

NCEI Geomagnetic Modeling Team and British Geological Survey, 2019: World Magnetic Model 2020. NOAA National Centers for Environmental Information, last access: 2023-11-08, doi:10.25921/11v3-da71.

Palomaki, R. T., N. T. Rose, M. van den Bossche, T. J. Sherman, and S. F. D. Wekker, 2017: Wind estimation in the lower atmosphere using multirotor aircraft. *Journal of Atmospheric and Oceanic Technology*, **34 (5)**, 1183–1191, doi:10.1175/JTECH-D-16-0177.1.

Peltier, W. and T. Clark, 1979: The evolution and stability of finite-amplitude mountain waves. Part II: Surface wave drag and severe downslope windstorms. *Journal of Atmospheric sciences*, **36 (8)**, 1498–1529, doi:10.1175/1520-0469(1979)036%3C1498:TEASOF%3E2.0.CO;2.

Pfister, L., et al., 2023: The TEAMx-PC22 Alpine field campaign – Objectives, instrumentation, and observed phenomena. *Meteorologische Zeitschrift*, submitted.

Plavcan, D., G. J. Mayr, and A. Zeileis, 2014: Automatic and probabilistic foehn diagnosis with a statistical mixture model. *Journal of Applied Meteorology and Climatology*, **53 (3)**, 652–659, doi:10.1175/JAMC-D-13-0267.1.

Prandtl, L., 1944: *Führer durch die Strömungslehre*. 2d ed., F. Vieweg & Sohn.

Reuder, J., P. Brisset, M. M. J. Stephanie, and Mayer, 2009: The small unmanned meteorological observer SUMO: A new tool for atmospheric boundary layer research. *Meteorologische Zeitschrift*, **18 (2)**, 141–147, doi:10.1127/0941-2948/2009/0363.

Rotach, M. W., G. Wohlfahrt, A. Hansel, M. Reif, J. Wagner, and A. Gohm, 2014: The world is not flat: Implications for the global carbon balance. *Bulletin of the American Meteorological Society*, **95 (7)**, doi:10.1175/BAMS-D-13-00109.1.

Rotach, M. W., et al., 2022: A collaborative effort to better understand, measure, and model atmospheric exchange processes over mountains. *Bulletin of the American Meteorological Society*, **103 (5)**, E1282–E1295, doi:10.1175/BAMS-D-21-0232.1.

Saigger, M. and A. Gohm, 2022: Is it north or west foehn? A Lagrangian analysis of penetration and interruption of Alpine foehn intensive observation period 1 (PIANO IOP 1). *Weather and Climate Dynamics*, **3 (1)**, 279–303, doi:10.5194/wcd-3-279-2022.

Schmidli, J., 2013a: Daytime heat transfer processes over mountainous terrain. *Journal of the atmospheric sciences*, **70 (12)**, 4041–4066, doi:10.1175/JAS-D-13-083.1.

Schmidli, J., 2013b: Daytime heat transfer processes over mountainous terrain. *Journal of the Atmospheric Sciences*, **70 (12)**, 4041 – 4066, doi:10.1175/JAS-D-13-083.1.

Schmidli, J. and R. Rotunno, 2010: Mechanisms of along-valley winds and heat exchange over mountainous terrain. *Journal of the atmospheric sciences*, **67 (9)**, 3033–3047, doi:10.1175/2010JAS3473.1.

Schumann, U., 1990: Large-eddy simulation of the up-slope boundary layer. *Quarterly Journal of the Royal Meteorological Society*, **116 (493)**, 637–670, doi:10.1002/qj.49711649307.

Schumann, U., 2012: *Atmospheric Physics: Background–Methods–Trends*. Springer Science & Business Media, doi:10.1007/978-3-642-30183-4.

Serafin, S., et al., 2018: Exchange processes in the atmospheric boundary layer over mountainous terrain. *Atmosphere*, **9 (3)**, 102, doi:10.3390/atmos9030102.

Serafin, S., et al., 2020: Multi-scale transport and exchange processes in the atmosphere over mountains: Programme and experiment. Tech. rep., innsbruck university press. doi:10.15203/99106-003-1.

Shimura, T., M. Inoue, H. Tsujimoto, K. Sasaki, and M. Iguchi, 2018: Estimation of wind vector profile using a hexarotor unmanned aerial vehicle and its application to meteorological observation up to 1000 m above surface. *Journal of Atmospheric and Oceanic Technology*, **35 (8)**, 1621–1631, doi:10.1175/JTECH-D-17-0186.1.

Sprenger, L. J. M., 2022: Thermodynamics and airstreams of a south foehn event in different Alpine valleys. *Quarterly Journal of the Royal Meteorological Society*, **148**, 2063–2085, doi:10.1002/qj.4285.

Strauss, L., S. Serafin, and V. Grubišić, 2016: Atmospheric rotors and severe turbulence in a long deep valley. *Journal of the Atmospheric Sciences*, **73 (4)**, 1481–1506, doi:10.1175/JAS-D-15-0192.1.

Stull, R. B., 1988: *An introduction to boundary layer meteorology*. Springer Science & Business Media, doi:10.1007/978-94-009-3027-8.

Stull, R. B., 2017: *Practical meteorology: an algebra-based survey of atmospheric science*. University of British Columbia, 940 pp., URL `www.eos.ubc.ca/books/Practical_Meteorology/`.

Sturman, A., et al., 2003: The Lake Tekapo Experiment (LTEX): An investigation of atmospheric boundary layer processes in complex terrain. *Bulletin of the American Meteorological Society*, **84 (3)**, 371–380, doi:10.F1175/BAMS-84-3-371.

TEAMx Community, 2022: TEAMx pre-campaign 2022. last access: 2023-11-13, URL `https://zenodo.org/communities/teamx-pc22`.

Umek, L., A. Gohm, M. Haid, H. Ward, and M. Rotach, 2021: Large-eddy simulation of foehn–cold pool interactions in the Inn Valley during PIANO IOP 2. *Quarterly Journal of the Royal Meteorological Society*, **147 (735)**, 944–982, doi:10.1002/qj.3954.

Umek, L., A. Gohm, M. Haid, H. Ward, and M. Rotach, 2022: Influence of grid resolution of large-eddy simulations on foehn-cold pool interaction. *Quarterly Journal of the Royal Meteorological Society*, **148 (745)**, 1840–1863, doi:10.1002/qj.4281.

University of Innsbruck, Institute for Atmospheric and Cryospheric Sciences, 2023: Ertel2. last access: 2023-11-09, URL `http://acinn-ertel.uibk.ac.at/`.

Vergeiner, I. and E. Dreiseitl, 1987: Valley winds and slope winds — Observations and elementary thoughts. *Meteorology and atmospheric physics (Print)*, **36 (1-4)**, 264–286, doi:10.1007/BF01045154.

Viebahn, T., 2023: Windregime und Stabilität in einem alpinen Seitental im Sommer. Eine Standortcharakterisierung im Rahmen der TEAMx Vorkampagne 2022. Bachelor's thesis, University of Innsbruck.

Wagner, A., 1932: Neue Theorie des Berg- und Talwindes. *Meteorologische Zeitschrift*, **49**, 329–341.

Wagner, J., A. Gohm, and M. Rotach, 2015a: The impact of valley geometry on daytime thermally driven flows and vertical transport processes. *Quarterly Journal of the Royal Meteorological Society*, **141 (690)**, 1780–1794, doi:10.1002/qj.2481.

Wagner, J. S., A. Gohm, and M. W. Rotach, 2014: The impact of horizontal model grid resolution on the boundary layer structure over an idealized valley. *Monthly Weather Review*, **142 (9)**, 3446–3465, doi:10.1175/MWR-D-14-00002.1.

Wagner, J. S., A. Gohm, and M. W. Rotach, 2015b: Influence of along-valley terrain heterogeneity on exchange processes over idealized valleys. *Atmospheric Chemistry and Physics*, **15 (12)**, 6589–6603, doi:10.5194/acp-15-6589-2015.

Weigel, A. P. and M. W. Rotach, 2004: Flow structure and turbulence characteristics of the daytime atmosphere in a steep and narrow Alpine valley. *Quarterly Journal of the Royal Meteorological Society*, **130 (602)**, 2605–2627, doi:10.1256/qj.03.214.

Wetz, T. and N. Wildmann, 2022: Spatially distributed and simultaneous wind measurements with a fleet of small quadrotor UAS. *Journal of Physics: Conference Series*, **2265 (2)**, 022 086, doi:10.1088/1742-6596/2265/2/022086.

Wetz, T. and N. Wildmann, 2023: Multi-point in situ measurements of turbulent flow in a wind turbine wake and inflow with a fleet of uncrewed aerial systems. *Wind Energy Science*, **8 (4)**, 515–534, doi:10.5194/wes-8-515-2023.

Wetz, T., N. Wildmann, and F. Beyrich, 2021: Distributed wind measurements with multiple quadrotor unmanned aerial vehicles in the atmospheric boundary layer. *Atmospheric Measurement Techniques*, **14 (5)**, 3795–3814, doi:10.5194/amt-14-3795-2021.

Wetz, T., J. Zink, J. Bange, and N. Wildmann, 2023: Analyses of spatial correlation and coherence in ABL flow with a fleet of UAS. *Boundary-Layer Meteorology*, 1–29, doi:10.1007/s10546-023-00791-4.

Whiteman, C. D., 2000: *Mountain meteorology: fundamentals and applications*. Oxford University Press, doi:10.1093/oso/9780195132717.001.0001.

Wildmann, N., A. Alexa, T. Wetz, and J. Zink, 2023: TEAMx-PC22 (TEAMx pre-campaign 2022) – Vertical profiles and multi-point in-situ measurements at Nafingalm collected with the SWUF-3D UAS fleet. Zenodo, doi:10.5281/zenodo.7903331.

Wildmann, N., M. Hofsäß, F. Weimer, A. Joos, and J. Bange, 2014: MASC – a small Remotely Piloted Aircraft (RPA) for wind energy research. *Advances in Science and Research*, **11 (1)**, 55–61, doi:10.5194/asr-11-55-2014.

Wildmann, N. and T. Wetz, 2022: Towards vertical wind and turbulent flux estimation with multicopter UAS. *EGUsphere*, **2022**, 1–20, doi:10.5194/egusphere-2022-110.

Wildmann, N., T. Wetz, and J. Zink, 2022: Towards spatio-temporal measurements in the mountain boundary layer with a fleet of UAS. *EGU General Assembly Conference Abstracts*, Vienna, Austria, EGU22–6490, doi:10.5194/egusphere-egu22-6490.

Zadra, A., et al., 2018: Systematic errors in weather and climate models: Nature, origins, and ways forward. *Bulletin of the American Meteorological Society*, **99 (4)**, ES67 – ES70, doi:10.1175/BAMS-D-17-0287.1.

Zangl, G., 2006: North foehn in the Austrian Inn Valley: A case study and idealized numerical simulations. *Meteorology and Atmospheric Physics*, **91 (1-4)**, 85–105, doi: 10.1007/s00703-004-0106-7.

Zardi, D. and C. D. Whiteman, 2013: *Mountain weather research and forecasting*, chap. Diurnal mountain wind systems, 35–119. Springer, doi:10.1007/978-94-007-4098-3_2.

AI statement

I hereby declare that I have composed this work independently and without the use of any artificial intelligence (AI).

Acknowledgments

First of all, I would like to thank my supervisors Norman Wildmann and Alexander Gohm for offering me the opportunity to work on this topic which nicely combines my interests in mountain meteorology and flying, for their long-term support and for fruitful discussions. I owe a special debt of gratitude to Land Tirol for providing land surface laser-scan data, Meteo Swiss for producing and the University of Innsbruck for providing COSMO-1E forecast data, as well as the European Center for Medium-Range Weather Forecasts (ECMWF) for producing and Copernicus Climate Change Service (C3S) Climate Data Store (CDS) for providing ERA5 Reanalysis data. Thanks to both Josef Zink and Tamino Wetz for their support during measurement campaigns, to Josef for giving me the idea to work on drones in my Master's thesis and to Tamino for patiently answering my questions about his papers. I offer thanks, too, to Jonathan Schumann, Marie Stöckhardt, and Lukas Lohner for accompanying me on hikes, bike tours, and swims to download measurement data from the loggers on Nafingalm, and Ayhan Khosan, Salome Hayler, and Charlotte Poppa for their advice on how to use QGIS. Last but not least I want to warmly thank my parents, my mother for always cheering me up and my father for sharing the enthusiasm for science.

universität
innsbruck

Eidesstattliche Erklärung

Ich erkläre hiermit an Eides statt durch meine eigenhändige Unterschrift, dass ich die vorliegende Arbeit selbständig verfasst und keine anderen als die angegebenen Quellen und Hilfsmittel verwendet habe. Alle Stellen, die wörtlich oder inhaltlich den angegebenen Quellen entnommen wurden, sind als solche kenntlich gemacht.
Die vorliegende Arbeit wurde bisher in gleicher oder ähnlicher Form noch nicht als Magister-/Master-/Diplomarbeit/Dissertation eingereicht.

Innsbruck, den 16.11.2023

(Datum, Unterschrift)